LBNL-41116
UC-404

ERNEST ORLANDO LAWRENCE
BERKELEY NATIONAL LABORATORY

The Structure and Morphology of Semiconductor Nanocrystals

Andreas V. Kadavanich
Materials Sciences Division

November 1997
Ph.D. Thesis

LBNL-41116
UC-404

The Structure and Morphology of Semiconductor Nanocrystals

Andreas Virin Kadavanich
Ph.D. Thesis

Department of Chemistry
University of California, Berkeley

and

Materials Sciences Division
Ernest Orlando Lawrence Berkeley National Laboratory
University of California
Berkeley, CA 94720

November 1997

This work was supported by the Director, Office of Energy Research, Office of Basic Energy Sciences, Materials Sciences Division, of the U.S. Department of Energy under Contract No. DE-AC03-76SF00098.

The Structure and Morphology of Semiconductor Nanocrystals

by

Andreas Virin Kadavanich

B.S. (University of California, Davis) 1992

a dissertation submitted in partial satisfaction of the requirements for the degree

of

Doctor of Philosophy in Chemistry

in the

GRADUATE DIVISION

of the

UNIVERSITY OF CALIFORNIA, BERKELEY

Committee in charge:

Professor A. Paul Alivisatos, Chair

Professor Gabor Somorjai

Professor Ronald Gronsky

Fall 1997

The Structure and Morphology of Semiconductor Nanocrystals

by

Andreas Virin Kadavanich

Abstract

The Structure and Morphology of Semiconductor Nanocrystals

by

Andreas Virin Kadavanich

Doctor of Philosophy in Chemistry
University of California, Berkeley
Professor A. Paul Alivisatos, Chair

Colloidal semiconductor nanocrystals were studied using High Resolution Transmission Electron Microscopy (HRTEM). Organically capped nanocrystals were found to have faceted shapes consistent with Wulff polyhedra after the effects of capping ligands on surface energies were taken into account. The basic shape thus derived for wurtzite (WZ) structure CdSe nanocrystals capped by tri-octyl phosphine oxide (TOPO) was a truncated hexagonal prism, elongated along the <001> axis with {100} and {002} facets. This structure has C_{3v} point group symmetry. The main defect in this structure is a stacking fault (a single layer of zincblende type stacking), which does not significantly affect the shape (does not alter the point group).

Zincblende (ZB) structures tend towards tetrahedral shapes with {111} facets when the capping ligand is ionic. This was shown for CdS passivated by polyphosphate ligands. For covalent ligands, ZB structures will form truncated octahedra with predominantly {111} and {100} facets as was seen in InP and InAs nanocrystals. In both cases, the resultant point-group of the crystallites is T_d. The main structural defect is a rotation twin fault (a single layer of wurtzite type stacking). Unlike the case for WZ structures, rotation twin faults significantly affect the particle morphology, leading to

misshapen crystallites with a point group symmetry different from the unfaulted crystallite.

Oxide passivated Si nanocrystals in the diamond lattice show evidence of faceting along {111}, {100} and {110} planes. However, large particles are quasispherical with vicinal surfaces and steps. Reflection twins are very frequently found in the center of the crystallite which suggests that they occur as part of the critical nucleus.

Core-shell nanocrystals of CdS/HgS/CdS (ZB) and CdSe/CdS (WZ) were investigated. The HRTEM data shows that growth of the shell proceeds in an epitaxial fashion in both systems. Image contrast also indicates the presence of a shell. As with ordinary nanocrystals, single-layer stacking faults are the major defects and have a large effect on the ZB morphology while only mildly perturbing WZ morphology in most cases. The similarity between the core-shell structures and plain nanocrystals grown by a similar method, suggests a common layer-by-layer growth mode.

Under various conditions, nanocrystals were found to self-assemble into arrays on TEM substrates. For large, faceted crystallites, this was found to result in oriented nanocrystals.

This page intentionally left blank.

Dedication

This dissertation is dedicated to my father who regrettably did not live to see it completed.

Table of Contents

Introduction **1**

Chapter 1: Experimental Details **3**

1.1 Introduction 3

1.2 TEM 3

1.2.1 Basics 3

1.2.2 Sample Preparation 6

1.2.2.a Carbon Films 7

1.2.2.b Other films 12

1.2.2.c Specimen preparation: Attaching samples to substrates 13

1.2.2.d Specimen processing 14

1.2.3 TEM data collection 14

1.2.4 TEM Image Processing 17

1.2.5 Computer Modeling and HRTEM Image Simulation 19

Appendix 1-A: The Preparation Of TEM Specimen Support Grids With 0.1-1.5 Micron Holes 27

Appendix 1-B: SAD Calibration Data 31

Chapter 2: Organically Capped Nanocrystals **34**

2.1 Background 34

2.2 CdSe nanocrystals 34

2.2.1 Sizing 35

2.2.1.a Low-resolution TEM sizing 36

2.2.1.b Size data from CDF sizing 39

2.2.1.c HRTEM Sizing........42
2.2.2 Nanocrystal morphology........48
2.2.2.a Implications of Nanocrystal Morphology........54
2.2.2.b Concluding remarks........56
2.3 Aqueous CdS........56
2.3.1 Morphology........57
2.3.2 Remarks........59
2.4 InP........60
2.4.1 Morphology........61
2.4.2 Remarks:........64
2.5 InAs........64
2.5.1 Morphology........65
2.6 Si Nanocrystals........65
2.6.1 Morphology........66
2.6.1.a 111-Twins Fault in Si Nanocrystals........67
2.6.2 Remarks........69
2.7 Conclusions........69
Appendix 2-A: Identifying Common Semiconductor Crystal Structures And Orientations In HRTEM Images........100

Chapter 3: Epitaxial Nanocrystals........104

3.1 Introduction........104
3.2 CdS/HgS/CdS Quantum Onions........106
3.2.1 Morphology........106
3.2.1.a Multiply-Twinned Tetrahedral Crystallites: Onions with Ears........108
3.2.2 Remarks........110
3.3 CdSe/CdS Core-Shell nanocrystals........111
3.4 Conclusions........115

Chapter 4: Ordered nanocrystal layers **127**

Conclusions **134**

Concluding Remarks 136

References **138**

List of Figures

Figure 1.1: Schematic of a TEM 20

Figure 1.2: Optical Path of a TEM.. 21

Figure 1.3: Carbon Evaporation: Use of thickness indicator.. 22

Figure 1.4: Removing Carbon Films from evaporation substrates.. 23

Figure 1.5: Attaching Carbon Films to TEM Grids.. 24

Figure 1.6: Magnification Calibration for 002B 25

Figure 1.7: Symmetric Ruler For Measuring Ring Radii in SAD's.. 26

Figure 2.1: CdSe Nanocrystals.. 70

Figure 2.2: Centered-Dark Field Operation of the TEM 71

Figure 2.3: CDF micrograph of CdSe nanocrystals.. 72

Figure 2.4: CDF Trace of CdSe nanocrystals 73

Figure 2.5: Arrangement for Tracing CDF images.. 74

Figure 2.6: CDF Size Data, 0.25 nm bins 75

Figure 2.7: CDF Size Data, Automatic Binning 76

Figure 2.8: CDF Size Data, Natural Binning.. 77

Figure 2.9: CDF Size Data, "Unnatural" Binning 78

Figure 2.10: CDF Size Data, 0.1 nm Binning.. 79

Figure 2.11: Aspect ratios from CDF measurements.. 80

Figure 2.12: Nanocrystal Aspect Ratio vs. Mean Diameter 81

Figure 2.13: Nanocrystal Aspect Ratio vs. Major Axis Diameter 82

Figure 2.14: Nanocrystal Aspect Ratio vs. Minor Axis Diameter.. 83

Figure 2.15: HRTEM Sizing of Wurtzite CdSe.. 84

Figure 2.16: Projections of Hexagonal Crystallites 85
Figure 2.17: Sizing Data from HRTEM 86
Figure 2.18: Model of CdSe Nanocrystal 87
Figure 2.19: Faceted CdSe Nanocrystals 88
Figure 2.20 : Faceted CdSe Nanocrystals 89
Figure 2.21: Faceted CdSe Nanocrystals 90
Figure 2.22: High Temperature Reconstruction of a CdSe Nanocrystal 91
Figure 2.23: CdS Nanocrystals 92
Figure 2.24: Large Tetrahedral CdS Nanocrystals 93
Figure 2.25: InP Nanocrystals, Octahedral Shape 94
Figure 2.26: InP Nanocrystals, Tetrahedral Shape 95
Figure 2.27: InP Nanocrystals, Defect Shapes 96
Figure 2.28: Models for InP Morphology 97
Figure 2.29: InAs Nanocrystals 98
Figure 2.30: Si Nanocrystals 99

Figure 3.1: Tetrahedral CdS Cores 117
Figure 3.2: CdS/HgS Core-Shells 118
Figure 3.3: CdS/HgS/CdS Nanocrystals 119
Figure 3.4: Size Evolution from CdS to QDQW 120
Figure 3.5: Onions with Ears 121
Figure 3.6: TEM Simulations of Multiply Twinned QDQW's 122
Figure 3.7: QDQW Model 123
Figure 3.8: CdSe/CdS Core-shell Nanocrystals 124
Figure 3.9: Size Evolution of Core-shell nanocrystals 125
Figure 3.10: Intensity Profiles Across Core-shell Samples 126

Figure 4.1: Ordered InAs Nanocrystals 131
Figure 4.2: Oriented CdSe Nanocrystals............ 132
Figure 4.3: Oriented CdSe Nanocrystals, High Resolution 133

List of Tables

Table 1.1: 200 kV Camera Length Calibration for 002B, July 1994 32

Table 1.2: 200 kV Camera Length Calibration from December 1995 33

Table 1.3: Camera Length Calibration for 002B at 120 kV 33

Notes on Nomenclature

Many people from various disciplines study nanocrystals, and the nomenclatures are not necessarily consistent across disciplines. I have tried to adhere to common conventions as much as possible. As far as I have not found any firm guidelines I have striven to be internally consistent. Below I address some of the conventions used in this manuscript.

I have chosen to give dimensions in units of nanometer rather than Ångstrom. The latter is the unit of choice for most chemists but in a bow to standardization I have chosen the SI units. It is assumed that the reader will have no problems in making the conversion.

Crystallographic indices occur throughout the documents. I have adopted the recommended conventions of the International Crystallographic Union[1], shown below.

hkl	label for a diffraction spot/ring
[hkl]	designates a lattice vector direction
<hkl>	designates a set of symmetry-related lattice vector directions

e.g. in zincblende, <100> designates the set [100], [$\bar{1}$00], [010], [0$\bar{1}$0], [001], [00$\bar{1}$]

(hkl)	designates a family of lattice planes/a surface
{hkl}	designates a family of symmetry-related lattice planes/surfaces

Additionally, for hexagonal systems, there exists an alternate four-coordinate notation of the form hkil, which the reader may encounter in the literature (but not in this manuscript). The relevant indices for comparison to some of the cited literature are <0001>, equivalent to <001>, and <10$\bar{1}$0>, equivalent to <100>.

Finally, the concept of a rotation twin fault occurs at various points in the

---

[1] 1. Hahn, T., ed. *International Tables for Crystallography, Volume A, Space-Group Symmetry.* Fourth revised Edition ed. International Tables for Crystallography. Vol. A. 1995, Kluwer Academic Publishers Group: Boston.

manuscript. Crystallographers may take exception to this term as a crystallographic twin is incompatible with the definition of a fault. Nevertheless, this term is frequently encountered in the literature, especially in solid-state physics. It refers to the growth fault formed along the <111> direction in zincblende structures (ABC stacking) by the introduction of a single layer of wurtzite type <001> (ABA) stacking. This comprises only half of an intrinsic or extrinsic fault with the result that the orientation of the lattice changes in traversing the fault, in a twin-like manner.[2] The lattice is reflected across the fault, however, if the basis is included the actual symmetry relation between the two domains on either side of a [111] fault is a 141° rotation about the $[1\bar{1}0]$ axis. Hence the designation as a rotation twin. The full term rotation twin fault nicely captures the effect this type of growth fault has on the crystal structure, so I have chosen to retain it.

---

[2] See Northrup, J.E. and Cohen, M.L., *Electronic structure of the rotation twin stacking fault in b-ZnS*. Physical Review B, 1981. **23** (6): p. 2563-2566. for a nice explanation of the various growth faults.

List of acronyms

ASU	Arizona State University
BF	Bright Field
CA	Condenser Aperture
CBED	Convergent Beam Electron Diffraction
CDF	Centered Dark Field
CHREM	Center for High Resolution Electron Microscopy
CL	Condenser Lens
ECS	Equilibrium Crystal Shape
EDX	Energy Dispersive X-ray (spectroscopy) = x-ray fluorescence
EELS	Electron Energy-Loss Spectroscopy
FFT	Fast Fourier Transform
FT	Fourier Transform
HOMO	Highest Occupied Molecular Orbital
HRTEM	High Resolution Transmission Electron Microscope/Microscopy
KX	1000 times (magnification)
LBNL	Lawrence Berkeley National Laboratory
LED	Light Emitting Diode
LUMO	Lowest Unoccupied Molecular Orbital
MBE	Molecular Beam Epitaxy
MC	Minimum Contrast
NCEM	National Center for Electron Microscopy
OA	Objective Aperture
OL	Objective Lens
QD	Quantum Dot

QDQW	Quantum Dot inside Quantum Well
SA	Selective Area Aperture
SAD	Selected Area (Electron) Diffraction
SAXS	Small Angle X-ray Scattering
TEM	Transmission Electron Microscope/Microscopy
TFS	Through-Focal Series
TOP	trioctyl phosphine
TOPO	trioctyl phosphine oxide
UC	University of California
X	times (magnification)

Acknowledgements

I would like to thank all present and past members and affiliates of the Alivisatos group for their support, advice, and generally for being a cool bunch of people. Special thanks go to Dr. Joe Shiang for opening my eyes to the beautiful applications of group theory to nanocrystals. I am especially indebted to all the people who have provided samples for my studies: Dr. Vicki Colvin, Dr. Janet Katari, Dr. Sarah Tolbert, Dr. Andrew Guzelian, Dr. C.J. Chen, Dr. Xiaogang Peng and Jennifer Lee. I have also benefited in disproportionate measure from scientific discussions with Dr. Sandra Rosenthal.

The staff at NCEM deserves a special acknowledgement for performing a marvelous job. Special thanks go to Chris Nelson for keeping the microscopes operating at peak conditions in spite of users like myself. I have also benefited from many fruitful discussions with Dr. Uli Dahmen, Dr. Mike O'Keefe, John Turner and Dr. Frances Ross.

Similarly Prof. David Smith at ASU has been very helpful in the advancement of my knowledge and TEM proficiency. My thanks extend to the rest of the ASU Faculty and Staff who have assisted me with my studies.

I would like to thank Nisus Software for making the world's best word processor for technical writing. Producing this dissertation has actually been fun.

I would like to express my gratitude to the members of my committee, Prof. Ronald Gronsky and Prof. Gabor Somorjai for their support and guidance, and for keeping me on my toes. My greatest and most heartfelt gratitude is reserved for my advisor Prof. A. Paul Alivisatos for showing me the way while allowing me the freedom to find it in my own fashion.

Finally, I would like to thank all my friends who have kept me sane over the past five years. No need to name names. You know who you are.

Introduction

> *What would happen if we could arrange the atoms one by one the way we want them?*
>
> *–Richard P. Feynman, 1959*

Over the course of the past decade, the field of semiconductor nanocrystals has experienced tremendous growth and is beginning to settle into a stage of maturity. The physical properties, especially the electronic properties, of an increasing variety of nanocrystals are being studied in ever greater detail. The interest in the electronic properties is largely due to the possible applications of these nanocrystals in optoelectronic devices. Unlike the equivalent quantum dots produced by the conventional "top-down" semiconductor processing techniques, nanocrystals embody the "bottom-up" approach of molecular assembly. This makes nanocrystals particularly interesting for nanotechnology as it is a very scalable process.

It also means that nanocrystals are not merely a physical system, but an intensely chemical one. Advances in synthesis drive most of the progress towards better electronic properties. In particular, surface modification has come to be quite important, due to the large proportion of atoms at the surface and their large contribution to the electronic properties. The surfaces also are vitally important in determining how nanocrystals behave chemically. The passivating ligands on the surface determine what solvents nanocrystals are soluble in and how they interact with other molecules or substrates. Clearly if one wants to use nanocrystals as building blocks for complex structures and devices, an understanding of the surface chemistry will be vital.

The need for high-order structural characterization (beyond the spherical approximation) is also impelled by the drive towards the study of individual nanocrystals. Spectroscopic measurements on single nanocrystals are becoming common tools of investigation and show complex and unique behavior. No two nanocrystals behave the same! Theoretical treatment of such results will increasingly require a more sophisticated knowledge of the structure of individual nanocrystals, not just the common features of the ensemble average.

Determining the physical properties of a system is in principle a straightforward task. If the positions of all objects (atoms, electrons) and all their interaction potentials are known, the problem is solved. This trivial statement of course masks the incredible complexity of determining those parameters. This work presented here takes on the challenge of defining atom positions in colloidal semiconductor nanocrystals. It is hoped that the results presented may provide a basis for an improved theoretical understanding of nanocrystal properties as well as serve to stimulate further progress in the synthesis and characterization of nanocrystals.

To the human mind, the natural method for defining an object is to look at it. Hence, the obvious way to study a nanocrystal is to examine it under a high-powered microscope. The transmission electron microscope (TEM) makes it possible to do so with near atomic resolution and obtain images such as the one shown. Even without an understanding of how to interpret the image in terms of structure, there is an immediate aesthetic appeal to such pictures. However, obtaining such images is clearly no trivial task. The necessary effort is detailed in Chapter 1, which is intended to serve as a guide to the experimentalist wishing to obtain such images. The casual reader, interested mainly in the results and interpretation, may skip it and proceed directly to Chapter 2. The necessary theory for understanding the TEM images is presented therein together with results on nanocrystals such as the one shown here, which incidentally is a wurtzite CdSe nanocrystal, faceted along {100} (matching the hexagonal shape of the unit cell).

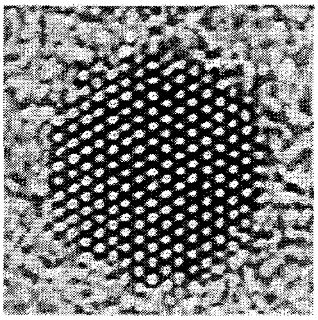

Chapter 1: Experimental Details

> *We have friends in other fields---in biology, for instance. We physicists often look at them and say, ``You know the reason you fellows are making so little progress? You should use more mathematics, like we do." They could answer us---but they're polite, so I'll answer for them: ``What* ***you*** *should do in order for* ***us*** *to make more rapid progress is to make the electron microscope 100 times better.*
>
> *—Richard P. Feynman, 1959*

1.1 Introduction

Structural studies of nanocrystals present many challenges. While characterizable as small molecules, real samples rarely have the uniformity required to apply molecular tools of structural characterization such as single-crystal x-ray diffraction or nuclear magnetic resonance. Yet, the small size (and small amount of material produced in most syntheses) makes it difficult to apply structural probes commonly used with inorganic crystalline materials. Powder x-ray diffraction tends to yield very wide peaks for the smallest sizes due to Debye-Scherrer broadening. Additionally nanocrystals are strained and frequently suffer from defects, such as stacking faults, which can add further complication to the interpretation of diffraction patterns. Above all, any bulk probe will only provide information about the average features shared by all nanocrystals. Thus, smaller details, including the surface structure are generally not available from such measurements. Scanning probe instruments suffer other limitations, the main one being that they cannot probe the interior of a particle. This is a serious drawback since the actual nanocrystal is usually protected by an organic ligand shell.

1.2 TEM

1.2.1 Basics

The transmission electron microscope (TEM) has the capability to overcome many of these deficiencies. Electrons interact much more strongly with matter than light or x-rays do and hence are well-suited to small sample sizes. Furthermore, the TEM can be used to look at individual nanocrystals and to discern their structural features down to atomic detail. This is the most powerful feature of the TEM as a structural probe for inhomogeneous systems.[1] Great effort is expended to obtain optical data from individual nanocrystals, while structural data on individual nanocrystals can be obtained from this commercially available instrument. There are drawbacks however, and to fully understand these it is necessary to briefly discuss the operation of a TEM. For a fuller discussion of how TEM's work and a general introduction to electron microscopy I recommend the excellent book by Williams and Carter. [1] For a deeper understanding of TEM and materials science the books by Hirsch [2] and Edington [3] are excellent reference sources, if somewhat dated. To appreciate the fine points of High Resolution TEM, the book by Spence [4] is an excellent treatise on the practice, while Reimer's monograph [5] covers the physics in excruciating detail.

Figure 1.1 shows a schematic cross section of the basic parts of a TEM. The main components are the electron source, a set of electromagnetic lenses, functional apertures, a sample holder, and a detection system. The whole setup is enclosed inside a high vacuum column. This limits the use of TEM to non-volatile samples (though progress is being made in the design of "environmental cell" sample holders).

In more abstract terms, the TEM may be treated as the electron analog of an ordinary optical microscope. As such it can be represented by the optical diagram in Figure 1.2 (a). Unlike an ordinary microscope however, the "light" source is highly monochromatic, akin to using a laser light source. Thus, in addition to ordinary imaging,

---

[1] The TEM is a truly remarkable and powerful instrument. Not only is it a superb structural probe with atomic detail, but it can also be used for spectroscopic analysis on a microscopic scale, thanks to EDX, EELS and Cathodoluminescence. While nanocrystals are presently at the detection limit for most of these techniques, it is only a matter of time before such techniques will become routine tools of chemical analysis in the nanocrystal size regime.

it is also possible to obtain the far-field diffraction pattern. In practice this is accomplished by adjusting the projector lenses to focus on the back focal plane of the objective lens instead of the first image plane, as depicted in Figure 1.2 (b). (The necessary adjustments are highly automated and apart from some minor corrections are accomplished at the push of a button.) The important point to keep in mind is that both modes use transmission geometry. A TEM images is a 2-dimensional projection of a 3-dimensional structure and overlapping structures can result in image artifacts which may not be obvious to the untrained observer. Similarly diffraction patterns can be overlapping patterns of several parts of the sample.

A variety of electron sources are available, see [1]. All the data presented in this document were obtained using a LaB_6 source, which consists of an oriented single crystal of LaB_6 shaped into a very fine tip. Electron emission occurs at the sharp point of the source and is thus spatially very restricted. This results in spatial coherence of the electron waves inside the beam, a feature that is exploited in HRTEM imaging. After emission, electrons are accelerated in a potential of typically 100-200 kV. This gives them a de Broglie wavelength between 0.00370 nm and 0.00251 nm. It is this short wavelength that allows for much better resolution in an electron microscope compared to a light microscope. In the final analysis, lens imperfections limit the obtainable point-to-point resolution to ~2 Å (0.2 nm, about ten times better than at the time of Feynman's talk). The improved resolution comes at the price of much more damaging radiation than light. While most electrons scatter elastically, a focussed beam bombards each nm^2 with some 10,000,000 ballistic electrons each second. These electrons can exact damage by heating, exciting electronic transitions (radiolysis), or by sputtering away atoms ("knock-on damage").

High Resolution lattice imaging adds another complication in that the HRTEM image is not merely a projection of the object being studied, but actually an interferogram formed by the diffracted electron beams from the sample. Hence HRTEM lattice imaging is restricted to samples that diffract (i.e. periodic crystals). Amorphous specimens do not give High Resolution lattice contrast. Furthermore, contrast depends on a variety of conditions, including the defocus setting of the microscope. Fortunately, nanocrystals are sufficiently thin that the weak-phase object approximation is reasonably satisfied. Under the proper operating conditions, HRTEM images can then be treated as projections of the crystal structure. To simplify image interpretation, images are normally collected at Scherzer defocus (and actually a through-focus series is collected). For the studies presented herein it was deemed sufficient to record images under conditions such that lattice contrast was maximized while staying within the first Fourier period from minimum contrast (MC) focus.

1.2.2 Sample Preparation

The ultimate limiting factor in microscopy is sample preparation. No amount of operator expertise or instrument capability can make up for a poorly prepared sample. The main consideration in this regard is usually sample thickness. Nanocrystals have an advantage over bulk materials in this aspect as they can be viewed in their native form. Thus one need not worry about artifacts induced by the thinning process, as one would with bulk samples. On the downside, nanocrystals cannot be prepared as free-standing samples. Rather they require a support substrate, and it is this substrate that is the most critical part of sample preparation for nanocrystal TEM.

The main criterion for a good substrate is that it should not interfere with the imaging of the nanocrystal. The easiest way to accomplish this is to choose a substrate that only weakly interacts with the beam. Ideally this means the substrate should be invisible relative to the sample. This presents a challenge as the samples, due to their thinness are only weakly interacting themselves. Hence to make the substrate less visible one chooses a weakly scattering material and makes a very thin film. The thinner the film, the more electron transparent it becomes. However, this comes at the expense of mechanical strength. A very thin film will sag when supported on even the highest mesh commercial TEM support grid. Thin films are also more susceptible to charging and heating induced by the beam due to their lower conductivities.

The remainder of this section will deal with the choice and preparation of sample substrates.

A note on nomenclature. For the purposes of this dissertation, the term "sample" refers to a particular set of nanocrystals that are derived from the same synthesis batch and any post-processing (such as size-selective precipitation). Generally, this means a sample corresponds to a vial containing a solution of nanocrystals in some solvent. A "grid" denotes a TEM specimen grid, either with or without a thin film coating. The term "specimen" is reserved for the actual piece of material that is inserted into the TEM. In practice a specimen thus consists of the support substrate (usually a TEM grid with a thin film coating) and a sample that has been deposited onto it. These conventions are not universal but will be adhered to in this document.

1.2.2.a Carbon Films

One of the best substrates available is amorphous carbon. The low atomic number of carbon ensures weak scattering of the electron beam. Carbon also has high thermal and electrical conductivities. Furthermore, having an amorphous substrate is helpful for the beam tilt and astigmatism corrections in HRTEM. Amorphous carbon films are relatively easy to prepare, making them suitable for routine investigations of large numbers of samples. Finally, carbon films can be prepared down to thickness of approximately 2 nm with sufficient mechanical strength to be self-supporting. [6]

Carbon films are easily prepared by sputter coating onto a suitable substrate. For most of the work presented in this document, this was done using a Denton 502A bell jar evaporator, located in the Electron Microscope Laboratory[1] (EML) at UC Berkeley. This evaporator uses electroresistive heating to evaporate the source material. The source material were 1/8 inch diameter amorphous carbon rods. Approximately 1 cm of the tip of a rod was sharpened to 1/16 inch for use as a filament in the resistive heater. The bell jar was evacuated to a pressure of roughly 5 x 10^{-6} torr using a turbopump. The filament was degassed by passing a 10 Ampere current through it for ten seconds. This gives an orange glow to the filament, but no measurable carbon evaporation. After the pressure has restabilized, the evaporation may proceed. The control of thickness is an art as much as a science. Most of it is guided by the use of a folded-over piece of filter paper near the substrate acting as a thickness indicator, Figure 1.3. The shadow cast by the fold gives an indication of the thickness of the evaporated film. A bright, focused light source (such as a flashlight) is useful for illuminating the indicator through the bell jar. To evaporate, the current through the filament is brought to 28 to 35 Amperes until there is a bright yellow glow similar to an incandescent light bulb, and maintained for a few seconds (up to 20 seconds at a time). To avoid eye-damage from the intense light, one should not look at the filament during this time.

For a given substrate at room temperature, the film thickness is governed by the evaporation rate (controlled by the current) and time and the source-to-target distance. The largest possible distance is generally desirable as it will give the slowest (most controllable) deposition rate. For the Denton the distance was about 15 cm. Experience will be the best guide as to the choice of current and evaporation time. Lower currents yield lower evaporation rates. It should be noted that the dependence on current is strongly non-linear and it is easier to fine tune the deposition by regulating the evaporation time than the current. If no evaporation is taking place, the current can be

---

[1] 26 Giannini Hall, UC Berkeley

increased in 0.5 Ampere increments until an acceptable evaporation rate is established. Multiple passes can be used until the desired thickness is reached, if the chamber is kept at vacuum. Single-pass films are likely of higher quality, as there is less chance for residual contaminants to become incorporated into the film, but I am not aware of any data to support this claim. To better control the evaporation, it is useful to try out each freshly sharpened filament in a blank run (with only the indicator). A carefully sharpened filament (that does not have many nicks and protrusions) will give fairly reproducible results, although the amount of current required to achieve evaporation will increase with use. Again, experience is the best guide for choosing suitable conditions.

Very thin films (2-5 nm thick) are barely visible. In fact, it may not be possible to tell by looking through the bell jar that anything has deposited. Thin films (5-20 nm) appear brownish/grey and will be barely visible through the bell jar and will be translucent. Medium thickness films (20-30 nm) will be clearly visible through the bell jar and look grey but still somewhat translucent. As the films get thicker, they become completely opaque and may look somewhat metallic/shiny. Generally, useful film thicknesses are in the 2-20 nm range.

A flat, smooth substrate for the evaporation ensures a flat, smooth carbon film. Two types of substrates were used in my studies: freshly cleaved mica sheets and single crystals of NaCl. Mica is cheap, and easy to handle. It comes in large sheets, which means that many specimens can be obtained from a single evaporation. However, the carbon adheres relatively strongly to the mica. Very thin films generally break during removal from the film because of this. Also, some shreds of mica stick to the carbon film after removal and can show up in EDX spectra of the specimens. [6] Nevertheless, for routine preparation of thin films, this is the substrate of choice. Mica sheets were obtained from Ted Pella Co. Films are removed from the mica by floating them off on a surface of distilled water. To do so, the mica sheet is slowly dipped at a shallow angle into a bowl of distilled water, Figure 1.4 (a). The carbon film will separate from the substrate and float on the water surface. If it does not, the sheet can be retracted and the procedure tried again. Scoring the film near the leading edge of the sheet can also help. Thin films are transparent and will not be visible except by reflection of light below the critical angle. A bright light source above the water surface is helpful in this regard.[1] Frequently, the film will break into many pieces which is of no concern as long as some pieces are large enough to coat a TEM grid. To coat a TEM grid, one grabs it with tweezers[2], dips it below the film, then lifts straight up while holding the grid at a shallow angle, see Figure 1.5. This generally traps a significant amount of water between the tweezer tips (unless anti-capillary tweezers are used). This water exerts enough surface tension to make removal of the grid difficult, so it should be removed by touching a Kimwipe or other absorbent tissue to the liquid between the tips. Similarly, some water is normally trapped under the carbon film (a good sign actually that there is a film on it) and should be extracted by touching the edge of the grid to the edge of a tissue[3]. Thereafter the grid can be removed and allowed to dry in air. Which side of the grid to coat is a matter of preference. While some people claim that adhesion is better on the dull side of the grid, others claim good results from coating the shiny side. Whatever one chooses, it is important to be consistent as some films will not be visibly to the eye, and the only way to tell the coated side is by knowing this information.

When mica contamination is a problem, (i.e. for EDX applications) NaCl single crystals are a cleaner substrate. They are also less adherent (they dissolve away in the water bath) and thus more suitable for very thin films. However, they are expensive and

---

[1] This is all set up in the EML

[2] reverse action tweezers are very useful for this.

[3] Placing the edge of the grid against the edge of the tissue minimizes the chance that the flat side of the grid will get stuck to the tissue by surface tension

generally not available with large areas. {100} cleaved single crystals were obtained from Ted Pella Co. These come as cubes of 1 cm edge length[1] and were further cleaved into 0.5 cm thick 1 cm squares. With care, these can be further cleaved into 0.25 cm thick sheets when necessary. As purchased, and when freshly cleaved, the surfaces are flat, however, the surfaces degrade rapidly with use. The crystals are best handled with plastic tweezers to prevent damage and contamination from skin oils. The procedure for film removal is the same as for mica, except that the NaCl crystals should be held by the sides, Figure 1.4 b. Since the crystals dissolve in the water bath, one should strive to minimize the time it takes to remove the film from the crystal, and immediately dry the crystal after removal. Also, the water bath will need to be replaced after several uses.

Carbon films can also be prepared as holey carbon. Rather than continuous films, these have holes of less than 10 μm diameter in them. The preparation of these films is described in Appendix 1-A. An alternative preparation using Formvar is available in the EML. The main use of holey carbon film is as a mechanical support for very thin continuous carbon films. For this, a regular TEM grid is first coated with a thick holey carbon film, which is then itself coated with a thin continuous film. The thick holey carbon film provides a strong support with a very high effective mesh size (much larger than the grids themselves). The sample is imaged through the thin film spanning the holes in the thick holey carbon film. The holey carbon film is also sufficiently transparent to allow for limited imaging. Moreover, the features in the holey carbon film can be used as landmarks at lower magnifications. They are particularly useful for the initial alignment, focussing, and stigmation of the objective lens.

Another use of holey carbon film is as a substrate for background free imaging.

---

[1] Larger crystals can be obtained. One unconventional source is your neighborhood IR spectroscopist. NaCl plates several cm's in diameter are used as windows for IR gas cells. Old, cracked windows, unsuitable for spectroscopy still make fine substrates for carbon films. While cheap, this is clearly not a reliable source, yet a good example of the value of recycling.

For this application, the holey carbon film is used as the main substrate on a grid, without an additional thin film on top. Occasionally nanocrystals will be found adhering to the edge of a hole, with the main part of the nanocrystal hanging over the hole and hence with no background from the substrate. This makes it possible to image the surface in better detail, in particular, it is possible to see amorphous material at the surface.

For very small particles, this technique does not work very well, as only a small portion of the particle will be free of the film, the remainder adhering to the film surface. This can be overcome by the use of larger particles as additional supports. The large particles provide a large surface area in cross section orientation for the smaller particles to adhere to. Only a small portion of the larger particle needs to be lying across a hole in the carbon film for the smaller particle to be imaged in its entirety without any background contribution. [7] This method holds promise, but was not attempted with our samples.

An alternative approach to background free imaging is the use of thin films of graphite in [001] orientation.[8] The procedure for making such films is somewhat laborious and the final film is contaminated with tungsten particles, but such films contribute virtually no background noise to the image. As with the above method, this has not been tried in our laboratory, but holds sufficient promise to warrant future investigation.

1.2.2.b Other films

An alternative substrate frequently used for biological samples is Formvar film, a polymer. This is easy to prepare and highly transparent. However, I have found its stability to be lacking. In particular, at the beam intensities required for HRTEM, the films frequently start vibrating irregularly. This may be due to thermal stresses or charging effects, but either way it is undesirable.

Aluminum films can be prepared by sputter coating in analogous fashion to carbon films. At low thicknesses (<10 nm) they are sufficiently transparent for HRTEM imaging. However, they films tend to be polycrystalline, with domain sizes on the order of 10-30 nm. Thus they have a lot of structure which interferes with the imaging of nanocrystals. Their appeal is mostly in their hydrophilic surface, which is suitable for samples that do not adhere well to carbon.

1.2.2.c Specimen preparation: Attaching samples to substrates

After a suitable substrate has been prepared, attaching the sample to it becomes the biggest challenge. The problem is mainly one of adhesion, and hence intricately related to the chemical properties of the nanocrystal surfaces and the substrate.

For the most common sample of TOPO coated nanocrystals on a carbon substrate this is rather trivial as the nanocrystals stick quite well to the carbon. One need only expose a filmed grid to a drop of solution and let the solvent evaporate. The nanocrystals will be left behind, stuck to the carbon film. As a general guideline, a weakly colored solution (optical density ≈ 0.1 at the exciton peak) will give a good density of crystallites on the film. [6]

For nanocrystals that are soluble in polar solvents (such as methanol) this procedure will not work as the surface of the carbon film is non-polar. Adhesion of such samples is improved by exposing the film to an argon ion plasma discharge (50 mtorr total pressure at a base vacuum of 10-20 mtorr for 30 seconds in the Denton 502A). The grid should be exposed to the sample solution immediately after this process. The plasma slightly charges the surface of the carbon film, increasing its interaction with polar samples. This process works better in a setup where the electrodes generating the plasma are inside the sample chamber than with an rf generator. Presumably this is due to field inhomogeneities near the electrodes, one of which supports the grids in the setup used in this study. Good results were obtained when the grids were supported on a piece of parafilm lying on the bottom electrode. This may not be necessary, but it helps to isolate the grids from the electrode itself and simplifies the handling inside the vacuum chamber.

Formvar films are polar and hence can be used as a substrate for polar materials. However, the limitations for TEM operations must be kept in mind.

1.2.2.d Specimen processing

Occasionally sample solutions contain large amounts of organic contaminants or the solvent itself may adhere to the carbon film. This becomes a source of contamination inside the microscope, where the influence of the electron beam will polymerize the organics, forming an opaque film. To avoid this, the dried specimen grid can be soaked in a suitable solvent for several minutes to remove any such materials. The main requirement on the solvent is that it must not dissolve the nanocrystals, but should dissolve organics well. Methanol works quite well with most samples.

Another potential problem is oxidation of air-sensitive samples, both in air, and from residual gases in the TEM. This can be overcome by evaporating a protective carbon layer onto a freshly prepared specimen grid. The trade-off is an increase in the background intensity. Hence, this should be done very carefully to evaporate only the minimum thickness to cover the nanocrystals. Unfortunately it is not known a priori what that required thickness is. The thickness of a nanocrystal itself is a good starting guess, and generally a 10 nm overcoat has good protective capability. Ideally, one would want to try several different thicknesses with each sample to optimize both image contrast and protection. In practice, the tediousness of this technique limits the number of samples that one may reasonably prepare in this way, and therefore the 10 nm thickness is a good target thickness for unknown samples.

1.2.3 TEM data collection

Most TEM data was collected on two of the microscopes at the National Center for Electron Microscopy (NCEM). They are the JEOL 200CX High Resolution TEM ("200CX") and the TopCon EM002B High Resolution TEM ("002B"). Both microscopes were operated at an accelerating voltage of 200 kV except for III-V samples which were studied at 120 kV. The 002B was also equipped with an energy dispersive x-ray (EDX) spectrometer to qualitatively measure x-ray fluorescence from a specimen being studied. Both instruments were equipped with Gatan image intensifiers and TV viewing systems. The nominal point-to-point resolutions at 200 kV for the 200CX and 002B are 0.23 nm and 0.18 nm respectively. While either microscope can be fitted with a slow scan CCD detector, all the data presented in this dissertation were recorded on TEM film (Kodak SO-163).

Quantitative EDX spectroscopy was performed on the JEOL 200CX Analytical Electron Microscope ("AEM") at NCEM. This microscope can also be equipped with a hot stage, which was used for high temperature diffraction studies. High Temperature HRTEM Imaging was performed on a modified Phillips 430 located at the Center for High Resolution Electron Microscopy (CHREM) in the Physics Department of Arizona State University (ASU). This microscope operates at 10^{-10} torr with a nominal point-to-point resolution of 0.2 nm at 300 kV. It is also equipped with an image intensifier and TV view system, as well as a video cassette recorder for data collection.

To simplify image interpretation, HRTEM images are normally recorded at Scherzer defocus, which is defined by the microscope parameters. In practice, since we were more interested in the lattice structure and gross morphology rather than exact atomic positions, the focus was chosen to give the most contrast in the lattice image while staying within the first Fourier period. Actual HRTEM imaging followed the following sequence of steps: (1) The substrate (carbon) image was brought into focus and adjusted for beam tilt (using voltage centering) and astigmatism. Frequently nanocrystals will show fringe contrast at this point. (2) The focus is adjusted to bring the nanocrystal to minimum contrast. (3) The nanocrystal is underfocused to the first maximum in the fringe contrast. This generally occurs 10-30 nm below minimum contrast, and thus is close to Scherzer defocus for the 002B. (4) The image is recorded at this setting.

Low resolution (amplitude contrast) images were recorded at minimum contrast focus in most cases. Occasionally, when it was more important to get good contrast than to image individual particle features, the image was underfocused. This improves contrast due to the bright, sharp Fresnel ring appearing around each particle.

Dark field images were recorded in centered dark-field (CDF) mode. In most cases the smallest objective aperture (2 nm^{-1} radius) was used as the limiting aperture. Sometimes the second smallest aperture (5 nm^{-1} radius) was used which under certain conditions may allow more than one diffracted beam from a single crystallite to contribute to the CDF image. Thus it is possible to get fringe contrast in some CDF images. Specifically, {001} fringes have been observed in CDF images of CdSe nanocrystals recorded on the 002B.

The magnification of the 002B at 200 kV was calibrated using gold foil. This calibration was performed once only and thus may no longer be accurate. However, spot checks using Si nanocrystals indicate that any variation should be less than 5%. To calibrate magnifications of 390KX through 590KX at the standard objective lens (OL) current, lattice images of gold {111} spacings were recorded on film and measured on the negatives using a loupe[1] with an integrated ruler with 0.1 mm markings. The size of a 0.1 μm sized feature at 390KX was also measured and compared to the same feature at lower magnifications to calibrate these magnifications. The results of this calibration are displayed in Figure 1.6.

The camera length at various OL currents was calibrated using >10 nm diameter

---

[1] Basically a magnifying glass.

Si nanocrystal electron diffraction patterns. Selected Area Diffraction (SAD) patterns were recorded on film. SAD patterns were recorded in a double exposure. The first exposure was performed with the beam stop blocking the direct beam to avoid saturating the film. The second exposure was a short (0.1 s) exposure with the beam stop removed to record the position of the direct beam on the negative. The resultant ring patterns were analyzed using a loupe with integrated ruler or a symmetric ruler (see Figure 1.7)for ring radii greater than 1 cm. The loupe allowed measurements to the nearest 0.1 mm, distances were estimated to the nearest 0.04 mm. The regular ruler had 1 mm markings and distances were estimated to the nearest 0.2 mm. Ring radii were measured by aligning the ruler across the central beam spot, measuring the diameter of highest intensity (judged visually) on a given ring and dividing by two. The symmetric ruler allows for direct measurement of radius by placing the zero mark on the central spot, then fine-tuning its position until the reading on either side of the zero for a given ring was the same. Readings for each ring were taken along two orthogonal axes and averaged to compensate for astigmatism and non-flatness of the negative in the camera chamber, both of which distort circular rings into ellipses. The results of this calibration are summarized in Table 1.1 in Appendix 1-B.

1.2.4 TEM Image Processing

Negatives were enlarged and processed on an Agfa Rapidoprint print processor. HRTEM images were generally exposed with the highest contrast setting as they only occupy a limited portion of the full dynamic range of the negative film. The full range of an SAD pattern cannot be represented on print film and hence several prints with different exposure times are necessary if one wants to compare intensities. Depending on the features to be shown in a given print, different contrast settings can be used.

For presentation and image analysis purposes, images were scanned and digitized.

Prints were scanned using flatbed scanners with resolutions ranging from 300dpi to 400dpi and 8-bit (256 level) dynamic range. Negatives were scanned using the NCEM's high resolution scanner. This instrument scans with 16-bit (65,536 level) dynamic range, which makes it particularly suitable for scanning SAD patterns.

For visual presentation, images were processed in Adobe® Photoshop software (versions 3.0 - 4.0) running on Power Macintosh® compatible computer systems. Processing operations commonly used were **Brightness/Contrast**, **Levels** and **Equalize**. These are all one-to-one operations, though not necessarily linear ones. This means that no pixel relationships will be reversed, i.e. any two pixels, one of which is darker than the other, will still have the same pixel be darker after such an operation is complete. However, the exact levels of darkness may vary. Alternatively, the Curves adjustment was used for finer control. Care was taken to maintain one-to-one correspondence, which translates into using a curve which has no inflection points. If one wants to compare intensities, it is necessary to also maintain linearity, which corresponds to using a straight-line curve in Curves adjustment. Brightness/Contrast also maintains linearity.

Diffractogram analysis of digitized TEM images was performed using Gatan® Digital Micrograph 2.5 or NIH Image 1.60 - 1.61 on Power Macintosh® compatible computer systems. Both programs use a fast Fourier Transform (FFT) algorithm, which requires selection of a square area with a binary edge length (2^x pixel squares). The main difference between the two programs is the use of a mask filter in Digital Micrograph which removes artifacts arising from the square shape of the source image area. However, for exploratory analysis, NIH Image is sufficient.

Digital Micrograph also has provisions for digitally enhancing scanned images using a variety of algorithms, such as the removal of aperiodic noise. One has to be wary of introducing artifacts in this process however and hence this should be a last resort only. None of the images presented in this dissertation have been thus enhanced.

NCEM has also developed a plug-in for Digital Micrograph which makes it possible to convert a scanned SAD pattern into a plot of intensity vs. radius (and hence scattering vector). The main difficulty with this process is the determination of the exact center for determining the radius. The NCEM plug-in makes the user select the center by visually fitting a circle displayed on-screen to one of the diffraction rings. This actually yields more reproducible results than the automated fitting process built into newer versions of Digital Micrograph. This is likely due to the subconscious image processing done by the user compensating for image defects and irregularities. The latter can lull a computer algorithm into a local minimum during the fitting process.[1]

1.2.5 Computer Modeling and HRTEM Image Simulation

Initially, structural computer models were created using Latuse and Plot3D software for MS-DOS compatible computers, available from LBNL. Thereafter, most models were created using the Catalysis package available with BIOSYM/MSI's Insight II (versions 3.0 and 4.0) software running on IBM RS6000 series and Silicon Graphics Inc. Indigo2 and Octane workstations. Some visualization of the models was done using Advanced Visualization System (AVS) software on Stardent 2000 workstations.

HRTEM image simulation was accomplished using Insight II, which uses the multislice algorithm of Cowley & Moodie [9].

---

[1] A note about the conversion routine: After selecting an area, the program asks for the maximum radius to be measured. The program performs no input checking and will allow the user to select a radius that exceeds the selected area. This can yield two possible results. The less troublesome is a crash. A more pernicious outcome results if the program does not crash. Rather it will produce artifacts in the intensity versus radius plot. This latter condition may not be obvious. Therefore it is important to carefully prepare the digitized image and select appropriate input values. A quick check for the artifact is to redo the measurement with a sufficiently small radius to be safely away from the edges of the image, yet includes some features from the SAD. Corresponding regions should be identical.

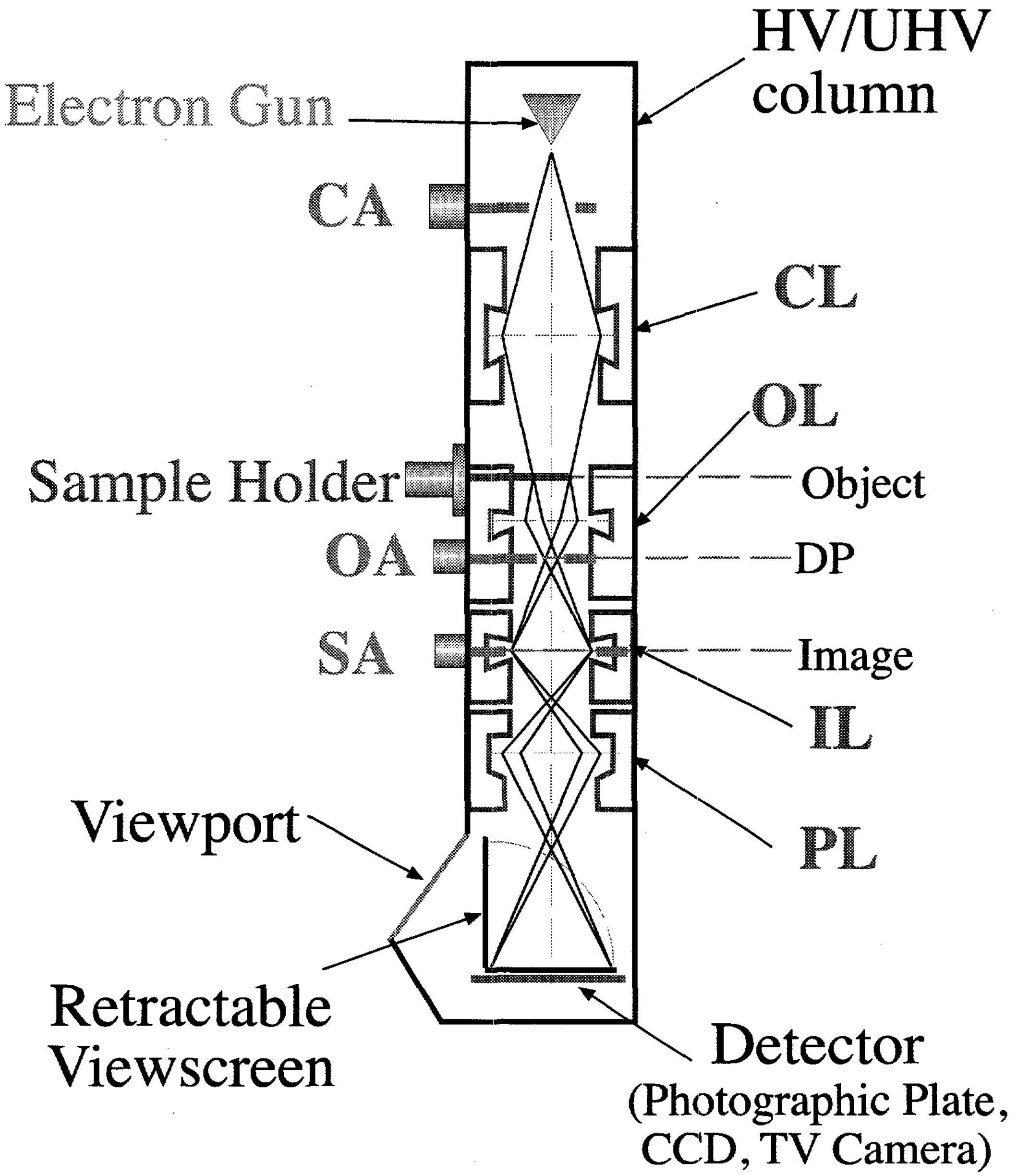

Figure 1.1: Schematic of a TEM

The essential components of a TEM. Not too scale.

CL = Condenser Lens	CA = Condenser Aperture
OL = Objective Lens	OA = Objective Aperture
IL = Intermediate Lens	SA = Selective Area Aperture
PL = Projector Lens	
DP = Diffraction Pattern	

In reality most lenses are actually compound lenses (e.g. there are 2 Condenser lenses…)

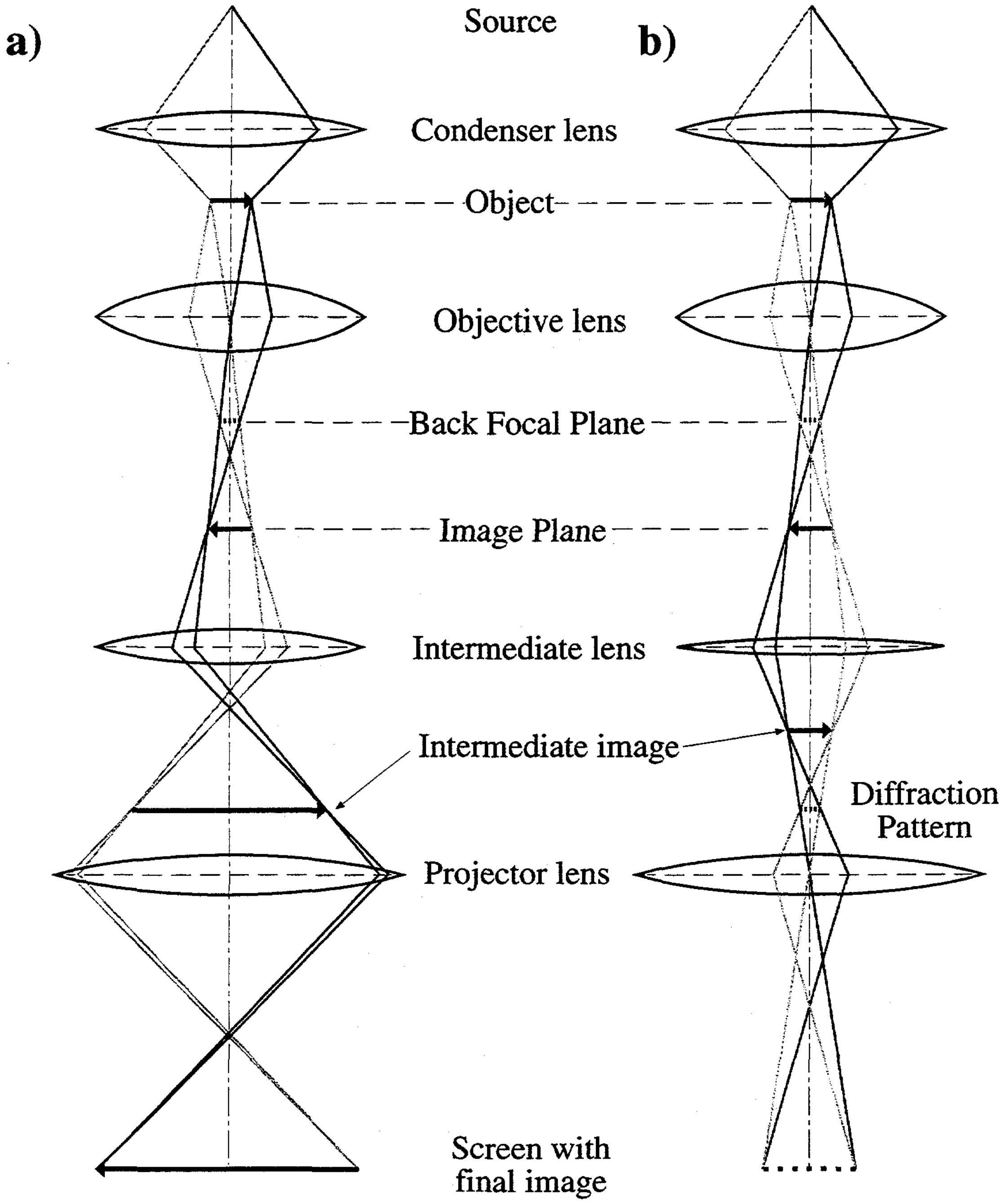

Figure 1.2: Optical Path of a TEM
(a) Ray diagram for TEM operation in imaging mode (left). The OA (not shown) is placed in the Back Focal Plane (BFP). The Intermediate lenses are focused on the image plane and the image is projected onto the screen.
(b) Ray diagram for TEM operation in diffraction mode (right). The SA (not shown) is placed in the Image Plane to select an area. The Intermediate lenses are focused on the BFP and the diffraction pattern is projected onto the screen.

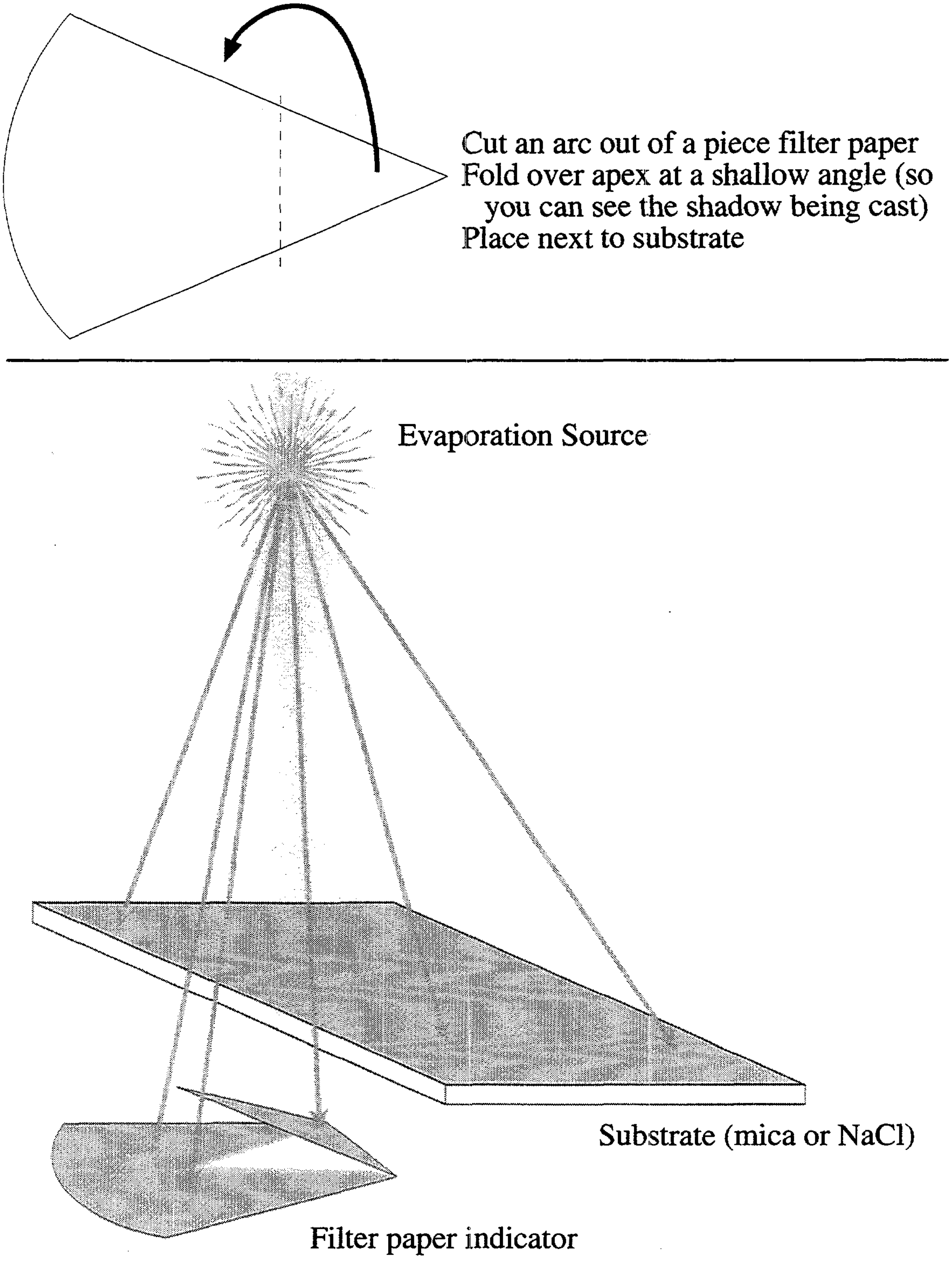
Cut an arc out of a piece filter paper
Fold over apex at a shallow angle (so
you can see the shadow being cast)
Place next to substrate

Figure 1.3: Carbon Evaporation: Use of thickness indicator

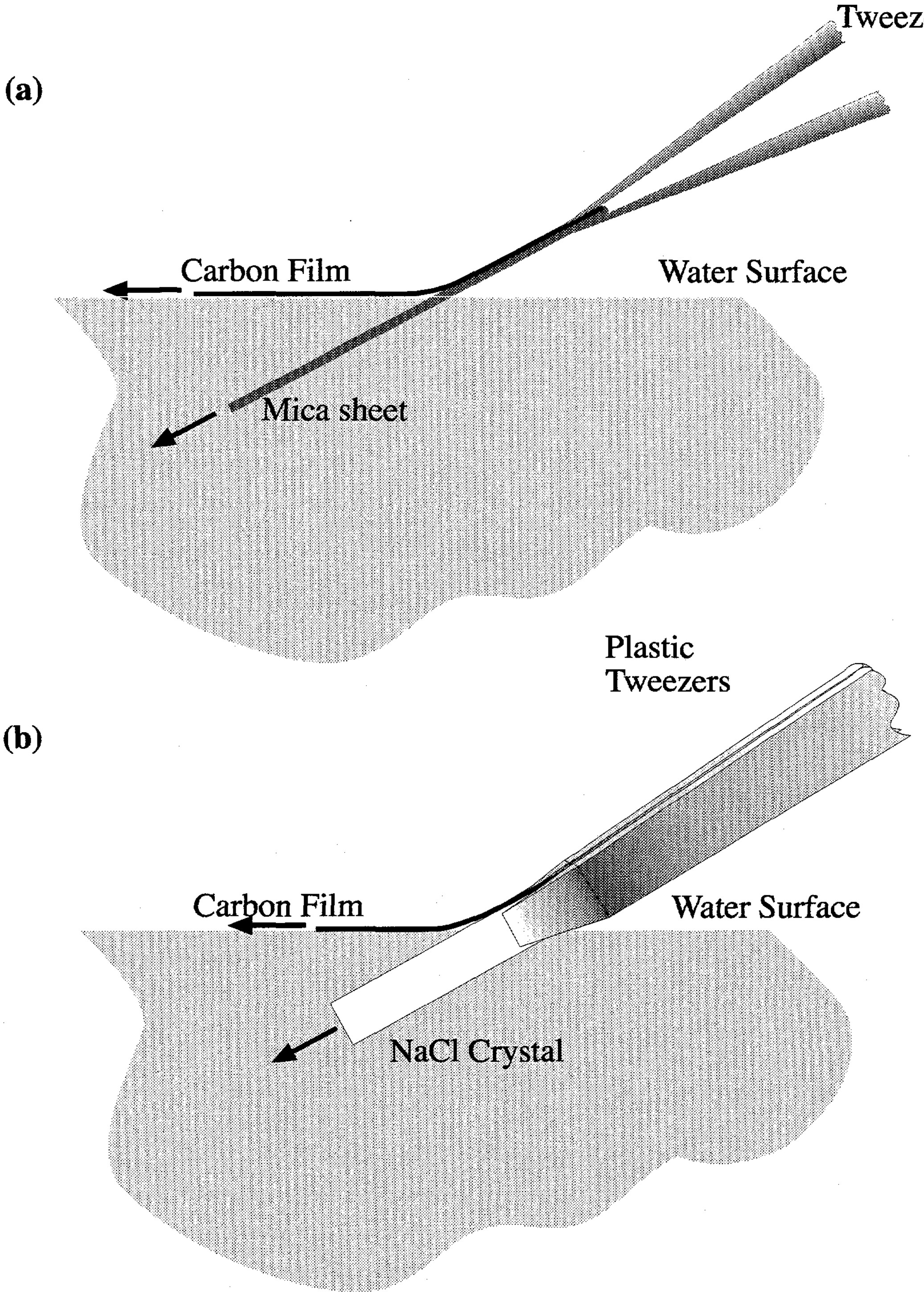

Figure 1.4: Removing Carbon Films from evaporation substrates

The substrate is immersed into a water bath in a straight motion at a shallow angle. The carbon film floats on the surface of the water. When retracting the substrate care should be taken not to disturb the floating carbon film

(a) Holding a mica sheet with tweezers.

(b) NaCl crystal held from the sides with plastic tweezers.

Figure 1.5: Attaching Carbon Films to TEM Grids

A TEM grid is dipped into the water and placed at a shallow angle below the carbon film. The grid is then lifted up in a straight motion. The presence of the film can be detected by the water underneath it. Water will not adhere to a blank grid. The excess water underneath the film can be removed by (carefully) touching the edge of the grid to a kimwipe. The water trapped between the tweezer tips should be removed similarly or its surface tension will draw the grid in when the tips are released.

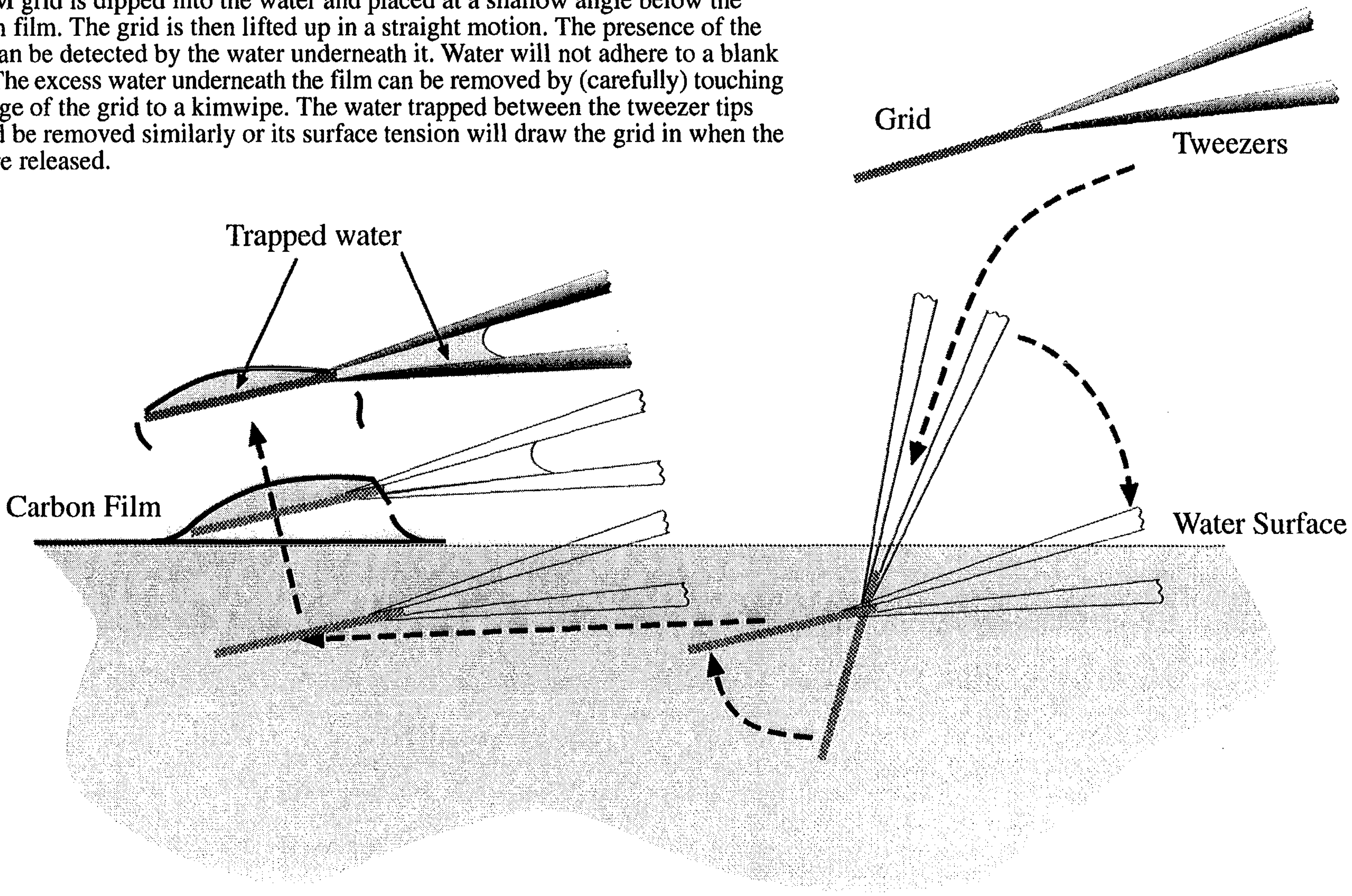

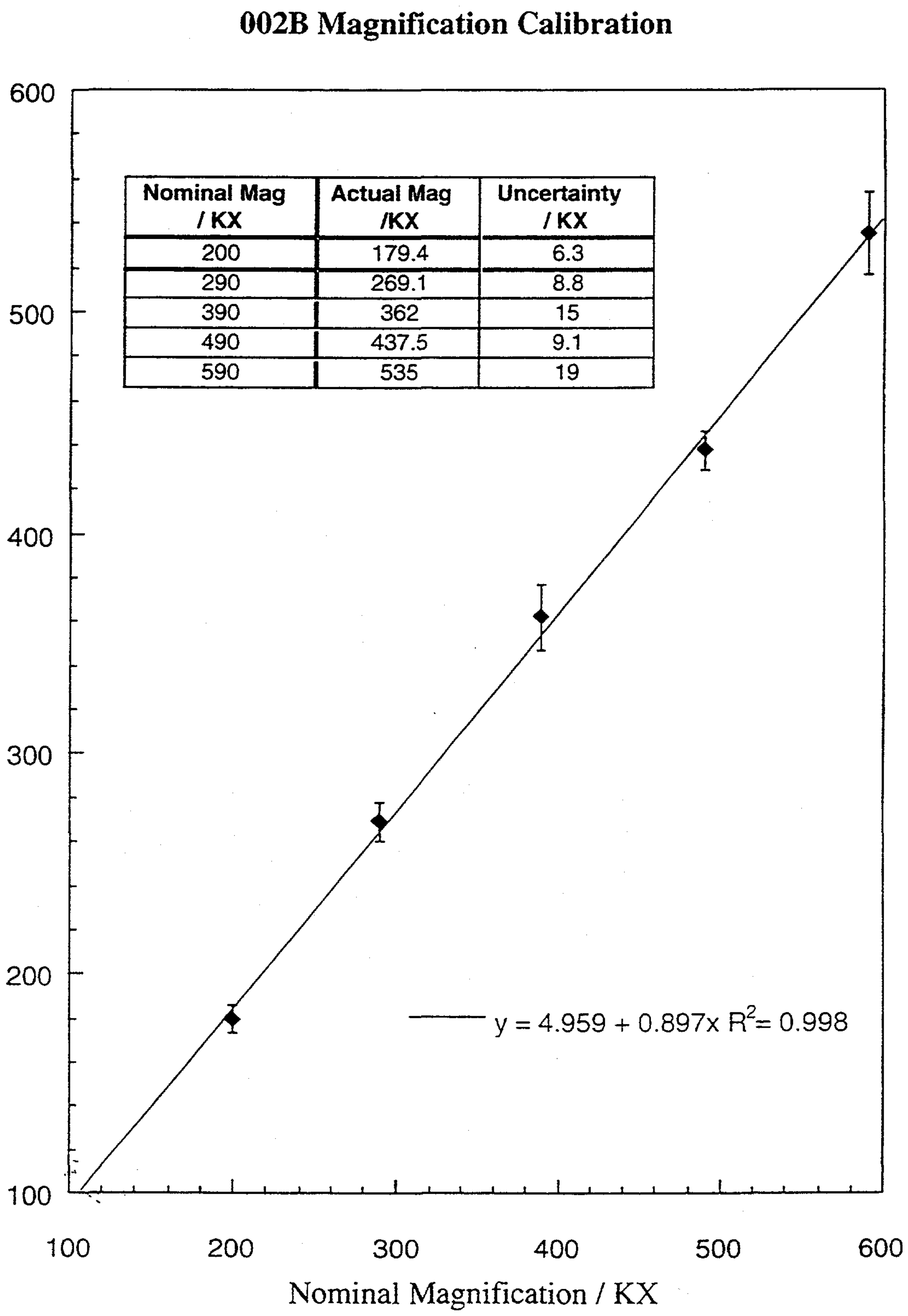

Nominal Mag / KX	Actual Mag /KX	Uncertainty / KX
200	179.4	6.3
290	269.1	8.8
390	362	15
490	437.5	9.1
590	535	19

Figure 1.6: Magnification Calibration for 002B

Measured at 200 kV operating voltage with objective lens current readings between 1130 and 1140.

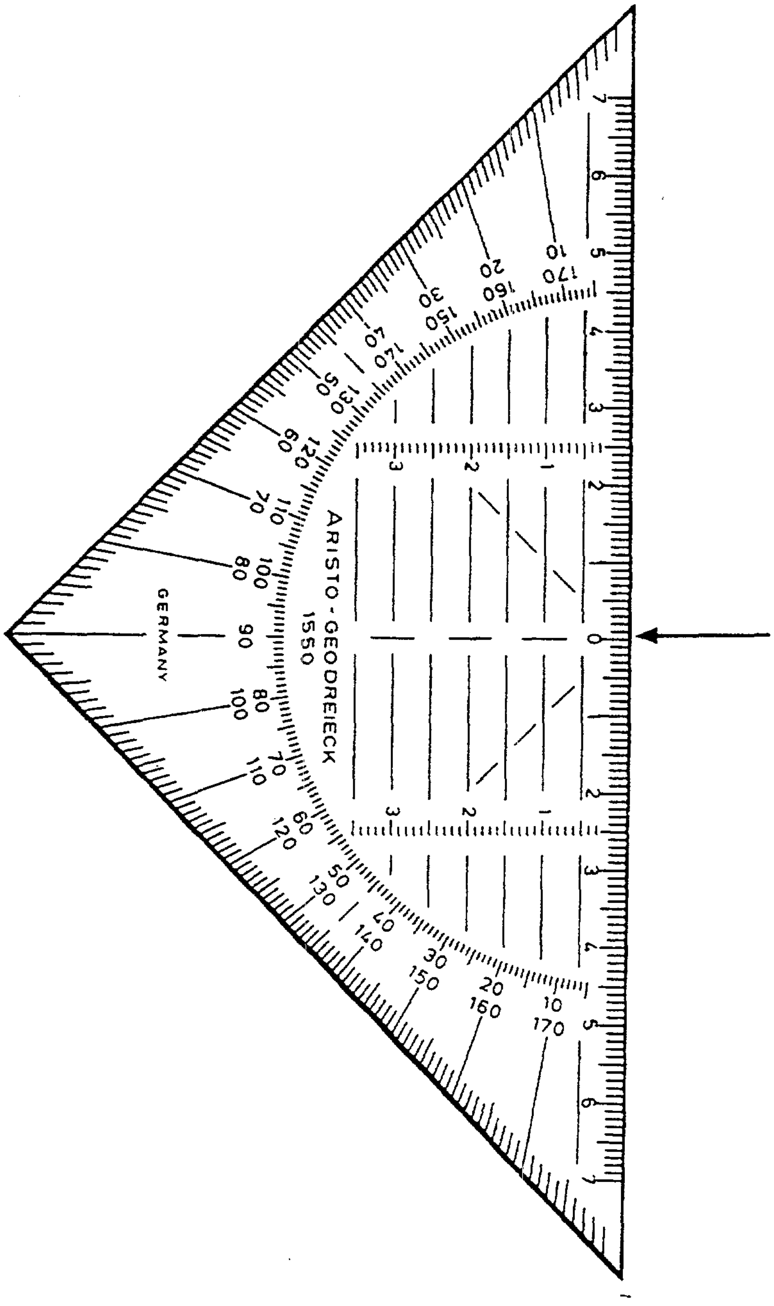

Figure 1.7: Symmetric Ruler For Measuring Ring Radii in SAD's

The ruler used for measuring ring radii in SAD's. The zero mark (arrow) is aligned with the central diffraction beam (if present) and then the position of the ruler is fine tuned for any given ring until the reading is the same on either side of center. The reading is the actual radius. Readings are taken along two orthogonal axes and averaged to correct for astigmatism in the lenses and tilt of the photographic plate.

This kind of ruler may be difficult to procure. Mine are imported from Germany, but graphics arts/drafting shops may carry something akin.

Appendix 1-A: The Preparation Of TEM Specimen Support Grids With 0.1-1.5 Micron Holes

after Eric L. Matheson

modified by L.F. Allard and D.F, Blake

(with additional comments by Andreas V. Kadavanich)

MATERIALS NEEDED:

Microscope glass slides

Tweezers

Specimen grids

Pasteur pipette

Metal block (top surface larger than glass slide)

Freezer (-15 to -20° centigrade)

Kimwipes

Paper towels

Distilled water

Acetone

Ethyl acetate

Vacuum evaporator

Dicoco Dimethyl Ammonium Chloride (DDAC)

Cellulose Acetate Butyrate (CAB)

Hydrofluoric acid

Safety Precautions:

HF is a very perfidious substance and should be handled with extreme care. While a 2% solution is rather benign one should still include all common precautions, including protective clothing and having neutralizing agent ready. Special precautions should be taken when preparing a 2% solution from more concentrated stock.

METHOD OF PREPARATION

Day 1:

1. Clean the glass slides with acetone and Kimwipes. Even new slides will have to be cleaned.
2. Mix solutions of:

DDAC (0.03%-0.05%) in water.
CAB (0.2%) in ethyl acetate.

3. Place metal block in freezer and allow to reach equilibrium temperature (overnight).
4. Soak the cleaned glass slides in DDAC solution 10-30 minutes. Remove glass slides from DDAC solution and rinse with distilled water for a few seconds. (Use a plastic squirt bottle.) Allow to dry overnight. This will leave a very thin water repellent layer an the glass. Blowing the rinsewater off with compressed air or Freon seems to give good results and produces a uniform water repellent layer.

Day 2:

5. Place glass slide in freezer on metal block for 5-30 seconds. (In Berkeley, in the summer, 30 seconds works well) Quickly remove slide from freezer and pour CAB solution onto it using Pasteur pipette. The slide should be held at an angle so the excess CAB will run off and the pipette nozzle should move across the length of the slide and

be touching or almost touching the glass. This is a subtle step but produces very fine results. The CAB solution should be applied very quickly after the slide is removed from the metal block (approx. 3 sec. or less). Condensation of water droplets on the glass will be immediate upon removal from the freezer. The CAB needs to be applied quickly to prevent larger water droplets from forming. Allow the CAB solution to volatilize after it has been applied to the glass. This step is the most critical and requires some practice. After the slide is dry, the presence of a holey plastic film will give it a light bluish-gray "smokey" appearance. The smallest holes are found in those areas with the very lightest coloration. The slide should be inspected under an optical microscope to determine whether or not suitable holes have been formed. Use a razor blade to carefully scrape away bad portions of the film.

6. Gently lower the glass slide into a plastic dish of 2% HF at an angle of 10° to 20° from the horizontal. The film should float off the slide and stay on the surface of the water. Using a new clean glass slide, transfer the film from the HF solution to a new container of distilled water. (Use the reverse motion from floating it off to pick it up, then float it off as before) This step should be done twice in order to completely rid the film of residual HF which could attack the specimen grids.
7. With the plastic film floating on the water, gently drop the metal grids onto the film with their dull side down (shiny side up), using a pair of tweezers. Avoid placing grids on the peripheral portions of the film as the distribution of holes on these areas is less uniform than in the center. Gently press each grid onto the film with the tip of the tweezers to ensure a good adherence to the film.
8. With an "island" of grids floating on the surface, place a piece of a paper towel so it covers the grids. (Don't use Kimwipes or other soft tissues), but hold on to it. Put the paper towel down in a rolling motion so that you gently cover the island. Gently lift the towel straight up. The grids and film should still be adhering to the paper towel.

9. Line a petri dish (or other suitable container) with Kimwipes so that the ends of the Kimwipes extend over the edges of the dish. Contour the wipes so they won't get stretched when the lid is put on the dish. Place the towel with the grids stuck to it into the petri dish and put the lid on. The Kimwipes will absorb the moisture from the towel and wick it to the outside (provided the ends of the wipes are sticking out of the dish) and the lid prevents excessive contamination with dust. Allow to dry (usually overnight is fine).

Day 3:

10. Place grids on a piece of filter paper into the vacuum evaporator and evaporate a layer of carbon onto them (200-500 Å is good).

11. Place your grids in a soxhlet extractor. Extract for 1 hour with Ethyl Acetate. Inspect grids under an optical microscope. Discard any with excessively torn films.

Alternatively if you are using Mo, Ti, Ni or other high-melting material grids you can use the following method (which is somewhat cleaner, but more destructive to the carbon).

Place the grids in a tungsten boat (a shaped foil will do nicely) and connect to an electrode in the evaporator. Pump down to high vacuum (10^{-5} torr or better). Pass an electric current through the foil so it just turns dull red. This will vaporize off the plastic and leave only the carbon film. Leave the current on for about 5 minutes so the plastic is completely vaporized. A holey carbon film with small holes (0.1-1.5 mm) should now remain on the metal grids. Inspect them under an optical microscope.

Appendix 1-B: SAD Calibration Data

Camera lengths were calibrated using the SAD patterns from large (> 10 nm diameter) Si nanocrystals. These nanocrystals gave ring patterns akin to powder x-ray diffraction patterns. Ring radii were measured directly off the negatives. Ring radii represent the radius of maximum intensity judged by eye as either (a) the highest intensity in the ring or (b) midway between the largest contrast changes on the inner and outer edges of the ring radius. Uncertainties in the measurement were estimated from the readings as well. Camera lengths were calculated from the measured radii, the known diffractions spacings of bulk Si powder (from the JCPDS data files) and the wavelength of 200 kV electrons. All camera lengths for a given setting were averaged, weighted by their inverse uncertainties squared. 95% Confidence limits were calculated from the standard deviation in the average using Student-t distributions. (See Bevington [10] for statistical procedures) The table below summarizes the results for various settings of the objective lens on the 002B.

Camera Length Calibration				
		OL Setting		
		1138	1140	1142
CL	76 cm	72.39 ± 0.23 (32)	73.27 ± 0.26 (32)	72.84 ± 0.20 (28)
	100 cm	93.81 ± 0.34 (22)	94.96 ± 0.25 (32)	94.42 ± 0.28 (20)
	120 cm	114.37 ± 0.74 (14)	115.84 ± 0.28 (24)	115.48 ± 0.28 (18)
	150 cm	139.09 ± 0.40 (12)	139.79 ± 0.41 (18)	139.64 ± 0.24 (16)

Table 1.1: 200 kV Camera Length Calibration for 002B, July 1994

Camera length calibration using Si nanocrystals for the NCEM TopCon EM002B microscope with UHR polepiece, from July 1994.

CL = Nominal Camera Length reading from the microscope.

OL Setting = Reading of the objective lens current obtained from CRT display.

Calibrated camera lengths are in cm. The Format is *Calibrated Camera Length* ± *95% Confidence Limits* (Number of measurements used for calculating average and Student-t factors).

For comparison, a spot check of the calibration was performed in December 1995. The data is shown below.

Camera Length Calibration 12/95			
	OL Setting		
	1138	1140	1142
CL 120 cm	114.87 ± 0.14 (38)	114.99 ± 0.17 (36)	115.23 ± 0.18 (36)

Table 1.2: 200 kV Camera Length Calibration from December 1995

Camera length calibration using Si nanocrystals for the NCEM TopCon EM002B microscope with UHR polepiece, from December 1995. Same format as Table 1.1.

Within the confidence limits, this is unchanged. Since better statistics were available for the latter calibration, it was used for all subsequent measurements at 120 cm, which was the standard camera length for most work at 200 kV.

A similar calibration for 120 kV acceleration voltage is shown below.

Camera Length Calibration at 120 kV			
		OL Setting	
		743	764
CL	73	68.069 ± 0.057 (64)	
	110	101.14 ± 0.27 (35)	101.84 ± 0.28 (14)

Table 1.3: Camera Length Calibration for 002B at 120 kV

Camera Length Calibration for 002B at 120 kV. Format same as Table 1.1.

Most 120 kV work was performed at OL = 764. The standard camera length at 120 kV was 110 cm.

Chapter 2: Organically Capped Nanocrystals

> *The surfaces of bodies are the field of very powerful forces of whose action we know but little.*
>
> *—Lord Rayleigh*

2.1 Background

Nanocrystals are generally treated as spherical particles for theoretical calculations of electronic structure. Hence they are defined by parameters of the bulk solid plus the addition of a single radius. Other considerations, such as slight deviations from sphericity [11] or crystal-field effects [12] are added perturbatively. While this description may be adequate to first order for the inhomogeneous samples currently prepared and studied, a more detailed treatment will be necessary if one wants to consider the molecular nature of nanocrystals. Clearly, a discrete, crystalline lattice cannot be shaped into a truly spherical object. In cases where the unit cell has lower than cubic symmetry, even a quasi-spherical shape may not be possible. Detailed considerations of the nanocrystal morphology are becoming more important as more work is shifting towards the optical properties of individual nanocrystals as opposed to ensemble properties. In particular, the large surface-to-volume ratio means that many important properties are controlled by the surface chemistry. Yet very little is known about the structure and composition of nanocrystal surfaces.

2.2 CdSe nanocrystals

CdSe nanocrystals are the prototypical nanocrystal system for study. This is due largely to the fact that a very well-developed synthetic route exists for making high-quality samples with good size distributions. CdSe nanocrystals are also somewhat unique in that they occur in the wurtzite crystal structure unlike the zincblende structure found in most semiconductor nanocrystals addressed in this study. The nanocrystals investigated for this manuscript were prepared by the methods described in the papers by Bowen Katari [13] and Peng [14]. The salient features for the following discussion are:

1. The nanocrystals are grown from atomic precursors: Dimethyl cadmium and TOP:Se (Selenium atoms coordinated to tri-octyl phosphine molecules).
2. Growth takes place in a coordinating solvent (tri-octyl phosphine oxide, TOPO) at high temperature (350°C). The TOPO passivates the nanocrystal surface.
3. Size control is achieved by rapid nucleation followed by growth under conditions that prohibit further homogeneous nucleation. This is achieved by rapidly lowering the temperature after the nucleation step.

2.2.1 Sizing

Determination of a sample's average size remains the initial step in any nanocrystal study intent on understanding size dependent properties. While calibrations now exist that correlate the absorption onset with average size for CdSe nanocrystals, TEM continues to be the best direct measurement for size. Furthermore, at this stage, only direct structural probes are suited to account for non-sphericity of the nanocrystals. While x-ray diffraction can provide some of this information as well [15], it relies heavily on fitting of the diffraction patterns. As the number of fitting parameters increases, the reliability of each parameter may be compromised by dependencies on other parameters. Furthermore, any fit will make some assumptions about shape, that may not be justified. Murray et. al. [15] overcome this problem by actually using the shape parameters determined from TEM for the x-ray fitting. Finally, the fit will only provide the average size, but not the size distribution. TEM sizing does not suffer from these limitations. In the ideal case, the only limitation is the number of nanocrystals included in a measurement. While measuring individual nanocrystals is tedious, sampling on the order of 200 nanocrystals can be accomplished in a reasonable amount of time and this provides a good statistical sampling.

However there are some experimental limitations as well. They all reduce to the difficulty of defining the edge of a nanocrystal on a continuous-tone image. The details are different for low-resolution imaging and HRTEM and hence should be addressed separately. For the purposes of this document, Low-resolution TEM designates imaging by amplitude contrast. Similarly, HRTEM will be used to indicate phase contrast lattice imaging. Amplitude and phase contrast are the terms properly applied to these techniques, but high and low resolution are suitable phenomenological descriptions as far as the data presented here is concerned. The latter are also more intuitively understandable to the average chemist. It needs to be kept in mind though that there are methods for obtaining contrast, both high and low resolution, which differ from the ones discussed below.

2.2.1.a Low-resolution TEM sizing

This method of imaging is appealing as the instrumentation is more readily available than its high-resolution kin, the image formation process is more intuitively understandable, and the level of operator experience required is far less than for HRTEM. The latter is important since TEM is not a common tool in most chemistry laboratories. Hence it is likely that (initially) this simpler method will be the main characterization tool. In bright field (BF) imaging a particle creates contrast by scattering electrons away from the direct beam. These scattered electrons are intercepted by an aperture and do not contribute to the final image. Hence the particle appears as a dark feature (fewer electrons) on a bright background on the final micrograph such as in Figure 2.1. Since most of the electrons do not get scattered, most of the signal in the recorded image is the direct beam, with the particle and substrate as small perturbations. Because the dynamic range of the recording film is finite and mostly used by the direct beam, the particle image will only cover a limited portion of the recording film's dynamic range. Furthermore, for a spherical particle, the intensity will diminish towards the edge in a continuous fashion, such that the edge contrast is diffuse. Because of this it is very difficult to define the edge of a nanocrystal based on the micrograph. It becomes largely a matter of judgement and hence human error is the largest source of error.

Contrast can be increased by lowering the TEM operating voltage (which increases the scattering cross section) and using the smallest possible objective aperture (which maximizes the range of scattered electrons that get intercepted), but these operations provide only limited improvement in contrast. A better way to increase contrast is to use centered-dark field (CDF) imaging. This inverts the normal image forming process by selecting a portion of the scattered electrons while blocking the direct beam. This is accomplished by tilting the illumination such that the direct beam hits the aperture and the electrons scattered through the tilt angle travel down the optic axis.[1] To get significant contrast from particles on a support substrate in this fashion requires that within the solid angle defined by the aperture, the scattered intensity from the particles is very different from the intensity due to the substrate. For an amorphous substrate, the best contrast is obtained when the aperture is set to pass diffracted beams from the particles. CDF operation is schematically shown in Figure 2.2. Under these circumstances, the particle image appears as a bright feature on a dark background, see Figure 2.3. The background consists mostly of incoherently scattered electrons from the amorphous substrate and is consequently very weak. The entire dynamic range of the film is thus available to record the feature, instead of the background, resulting in much higher

---

[1] An alternate method is to displace the objective aperture from the optic axis so as to pass the diffracted beam instead of the direct beam. The disadvantage to this method is that the off axis beam suffers from lens aberrations and astigmatism.

contrast. The edge contrast remains diffuse, but should be limited by particle morphology and the TEM optics rather than film sensitivity. The main drawback to CDF imaging is the long exposure time (10's of seconds) required to obtain an image. If the samples are unstable or the substrate is drifting during the exposure, this method will yield poor results.

Another factor to keep in mind is that, apart from the residual background signal from the substrate, only crystalline material contributes to the image contrast in CDF imaging. This reduces the likelihood of counting contaminants as part of the sample. On the other hand, the presence (and identification) of contaminants may be of value for other reasons. Therefore one should be careful in judging the quality of samples solely from CDF images. Additionally only a subset of particles oriented so as to diffract into the chosen reflections is sampled. If the sample has a tendency to orient preferentially in some direction, this may cause a problem. In this case it would be necessary to collect data at with the specimen tilted at several angles, so as to sample all necessary orientations.

The final problem in low-resolution sizing is calibration of the microscope magnification. Ideally this should be done under identical conditions (i.e. in the same session) as the actual data collection. In practice, a full calibration is a major undertaking in itself. However, it is generally possible to spot check a calibration quickly by imaging a suitable standard.

The actual size measurement can be done by hand with a ruler. Negatives should be enlarged for prints. If the contrast is high, e.g. for CDF images, one can get more enlargement by projecting the negative onto a wall using an overhead projector in a darkened room. The particle outlines can then be traced onto paper for subsequent measurement. An example of such a trace is shown in Figure 2.4. A transparent plastic ruler projected with the negative provides size calibration. If the negative position on the projector, and the projector-to-wall distance are unchanged, this needs to be done only once. The uncertainty in this measurement is on the order of 1%, far less than the uncertainty in the negative magnification. To prevent curling of the negative from the heat of the projector lamp it is best to cover the negative with a glass plate to keep it flat. A mask around the negative helps to keep excess light in the room to a minimum. The process is depicted schematically in Figure 2.5. When tracing outlines, it is important to remain consistent with regards to tracing the outside or the inside of the particle edge as the thickness of the pen line can be significant. Using the projection method incurs a significant time savings relative to preparing enlarged prints if a lot of particles need to be counted. On the downside, there is no method for adjusting the contrast of the projected image as there is with print processing.

Size measurements can be somewhat automated by computer. To do so the print or projector trace has to be digitized, which is easily accomplished with a flatbed scanner. NIH Image's **Analyze Particles** feature can very rapidly measure particle sizes after calibration. The main advantage over measurement by hand is that the particle shapes can be fit to ellipses. Both the major and minor axis diameters are measured, such that both an average size and an average aspect ratio can be determined. This method works best with traced outlines, as the background in a typical print tends to confuse the measurement algorithm. While background removal routines exist, the best is still visual determination of the particle edge by human judgement and tracing the outline onto paper, which ensures a background free measurement.

2.2.1.b Size data from CDF sizing

The results of a computer-sized CDF measurement of sample AKL-74D are shown in Figure 2.6 for a sample size of 320 particles. The CDF images were collected with the 100, 002 and 101 reflections passing through the #3 (6 nm^{-1} radius) objective aperture on the 002B. Murray et. al. [15] reported that CdSe nanocrystals preferentially adhere to the carbon support with their long <002> axis parallel to the substrate. This will not significantly affect the chosen reflections for the purposes of sizing. The negatives were projected onto tracing paper and the projected particle images were traced using a Sanford® Sharpie® Fine Point Marker such that the outside of the trace matched the particle edges as determined visually. Sample raw CDF data is presented in Figure 2.4. Some particles exhibit DF-fringe contrast. Based on the calibration, the set of fringes indicated in the figures has been assigned to the {001} spacing of CdSe. This arises in particles that are oriented such that both the 100 and 101 diffracted beams pass the objective aperture. These particles are effectively imaged in a two-beam condition, with the fringes arising from interference between these two beams.

The average mean diameter for this sample is 4.05 ± 0.58 nm (standard deviation). The average aspect ratio determined from TEM was 1.24 ± 0.15, consistent with other measurements in the range of 1.05-1.3. [15, 16] However, with such an aspect ratio one must question the wisdom of defining particle size by a single diameter. Indeed if one measures the major and minor axis diameters separately, one obtains average values of 4.47 ± 0.74 nm and 3.63 ± 0.51 nm respectively. Within this sample, these values are within the standard deviation of the mean value. However, many reports in the literature show samples with >5% standard deviation. For such a sample, an aspect ratio on the order of 1.2 will cause a significant error in the reporting of the diameter.

A histogram plot is a quick way of summarizing the size distribution, but care should be taken in the analysis. The histograms in Figure 2.6 were obtained using 0.25 nm bin sizes, chosen randomly. The peaks of the distributions match the average values, but there appears to be a second peak in the major axis distribution at 3 nm. This could suggest magic numbers in the size distribution but more likely is an artifact of the binning. Indeed, if the graphing program (Kaleidagraph™ 3.08 for Power Macintosh) is allowed to set the binning automatically, smooth distributions are obtained, Figure 2.7. However, an even better method is to choose natural parameters to bin the diameters. In particular, it is known that CdSe nanocrystals are elongated along the <002> axis [15, 16]. This is also confirmed by an occasional occurrence of fringe contrast in the CDF images, which shows {001} fringes perpendicular to the long axis, Figure 2.3 (arrow). It is therefore natural to bin major axis diameters in units of the {002} spacing, whereas the {100} spacing perpendicular to it is a sensible choice for the minor axis diameter. Using these parameters, one obtains the smooth distributions seen in Figure 2.8. However, one obtains smooth (indeed better-looking) distributions when one bins the major axis in units of {100} spacings and the minor axis in {002} units, Figure 2.9. This is not too surprising since the tracing action introduces some uncertainty into the measurement. Additionally, some particle orientations (e.g. <002> parallel to the electron beam) will have the <100> direction be the major axis. Overall it is more important then to choose a bin size around 0.35, which is the average of the {100}, {002} and {101} spacings, rather than any one of them. One certainly should avoid artificially small spacings, which will result in noise in the histogram, such as the 0.1 nm bin size used in Figure 2.10.

Similar considerations apply for measurements of the aspect ratio. Figure 2.11 (a) represents the distribution of aspect ratios measured as the quotient of major axis to minor axis diameters. The two sharp peaks present in this histogram disappear if instead of nm, the major and minor axis diameters are measured in units of {002} and {100} spacings respectively, as done in Figure 2.11 (b). However, it is not as obvious how to bin the measurements in (a) to avoid artifacts, as the natural aspect ratios depend on the size. This will be easier for samples where the size distribution is sharper.

Within the relatively broad size distribution however, one may ascertain some interesting features. In particular it is obvious from Figure 2.8 that the size distribution is sharper in the minor axis than in the major axis. This is also borne out by the standard deviation for the average diameters. This has been observed for all our wurtzite samples which suggests that growth occurs more readily on the <001> axis, consistent with observations on wurtzite crystal growth [17, 18] and evaporation[19]. The growth faces for this are the {001} faces which can be expected to be more chemically active due to their polar nature. These are known to be high-energy surfaces for bulk semiconductors in vacuum [20] which readily undergo surface reconstructions to lower their energy.

Based on this one would expect the aspect ratio to increase with size. Indeed if plotted as a function of the mean diameter (which should correlate to volume), Figure 2.12, there is a slight increasing trend in the aspect ratio. The scatter in the data is too great to draw any firm conclusions, as manifested by the poor R-value of 0.24 for the linear regression fit. Yet, size dependent aspect ratios have been previously reported for CdSe nanocrystals in glass [21], and various aspect ratios from 1.1 to 1.3 have been reported for colloidal CdSe nanocrystals. [15, 16] The scatter is less if the aspect ratio is plotted as a function of the major axis diameter, as in Figure 2.13. A definite correlation emerges here, also evidenced by the R-value of 0.5. On the other hand, if plotted against the minor axis diameter, a negative correlation, if any, is obtained, Figure 2.14, again with a lot of scatter. In conclusion, judgement as to whether CdSe nanocrystals exhibit a size dependent aspect ratio should be reserved for further, systematic study, especially as better samples are now available than were at the time of this research.

2.2.1.c HRTEM Sizing

HRTEM (phase contrast imaging) Sizing is a very powerful method for obtaining highly accurate size measurements. Particle sizes are determined from the number of lattice fringes in the image. Since the fringe spacings are known, there is no need to calibrate the magnification of the images (except to verify the identity of the fringes). Additionally, if cross fringes are present in the image of a nanocrystal, the orientation can be uniquely determined and hence the major and minor axes can be rigorously defined. Even if there are no clear cross fringes, there is frequently enough information to identify the nanocrystal orientation based on the details of simple fringe patterns, though it may not be possible to measure both axis diameters in this case.

In principle, the same particles that are properly aligned for CDF should display fringe contrast in HRTEM. In practice, the tolerances for HRTEM are more restrictive and fewer particles will be sampled in a HRTEM exposure than in the equivalent CDF exposure. Hence it is more difficult to find a suitable area on a specimen for imaging, and there will be fewer particles in a given exposure. This is the major drawback to this method of sizing. Sampling statistics are much worse, even though the accuracy of each individual measurement is much better. The only way to improve this is to spend more time collecting data. The amount of labor required for the latter ultimately limits the quality of the size measurement.

One significant advantage over CDF is that exposures take only a few seconds such that beam-induced changes to the specimen can be minimized. A trained operator can translate the specimen into position, adjust focus and astigmatism, take an exposure in less than 30 seconds and then move on. Such guerilla tactics are not necessary with most CdSe samples but are essential when trying to image less robust samples such as III-V nanocrystals. With these it is in fact desirable to use low dose techniques. For this the sample was translated such that the area of interest was outside the beam for adjustment of focus, voltage center and astigmatism. The beam was then spread out to reduce the electron flux per unit area. The beam remained so while translating the specimen back into position and compensating for drift. The beam intensity was increased just enough to fine tune the focus and astigmatism. (For the 002B, this was usually with the condenser 1 click from the position used for recording the image.) The intensity was then increased to the level required for a short exposure (1 to 2 seconds) and the image recorded.

The analysis of HRTEM data is fairly straightforward, albeit tedious. Fringe spacings can be assigned directly on the negative, using a loupe. For purposes of demonstration it is easier to use the enlarged positives of Figure 2.15. It should be noted here that none of the CdSe samples presented in this document were rigorously sized by HRTEM (except in the context of the core-shell studies) as this methodology was developed after the study of CdSe samples was completed. However, it is instructive to demonstrate the technique on this sample for comparison to the CDF method. Part (a) shows a nanocrystal in [001] orientation, i.e. with the unique wurtzite axis out of the plane of the image. Part (b) shows another crystallite in [010][1] orientation, with the unique axis in the plane and pointing up. The image contrast is such that atomic positions are dark and white areas correspond to channels in the crystal structure. This dark-atom contrast condition is normal for recording most images.

The hexagonal shape of the crystallite in Figure 2.15 (a) arises from the shape of the unit cell and will be discussed later. For sizing it is only important to know that the distance between channels is equal to the *a* lattice parameter (i.e. the magnitude of the <100> lattice vector), which equals 0.42999 nm for bulk CdSe. The angle between three mutually neighboring channels is 60°. The distance between adjacent rows of channels is equal to the {100} plane spacing of 0.37238 nm. The diameter is defined as the distance between the centers of atom planes on opposite surfaces. This measurement is indicated by the arrow in the figure. In units of {100} spacings, this diameter is obtained by counting the number of rows of channels perpendicular to the arrow. This yields a count of 16 and a corresponding diameter of 5.958 nm. Since the amount of lattice strain and surface relaxation is unknown (but should be $\leq$0.1nm based on bulk surface relaxations

---

[1] It is my convention to designate the orientation [010] such that I reserve the label of (100) for the fringes in the image and the corresponding surfaces. This is just for consistency. The [100] and [010] orientations are of course symmetry-related

[20]) this value is more reasonably recorded as 6.0 nm. Similarly measuring the diameter between the second set of opposite surfaces (rotated 60°) yields a count of 17 planes or 6.4 nm. The same value is obtained for the third set. An average diameter for this crystallite is then 6.27 ± 0.23 nm (standard deviation).

It is not obvious how to report an aspect ratio for such a crystallite. One can easily measure the diameter perpendicular to the lattice spacings listed above. The corresponding lattice spacing is the unit cell vector, 0.42999 nm, and the measurement runs between opposite apices. However, if defined in this manner, a perfectly hexagonal crystallite will have an aspect ratio of 1.15. A more meaningful definition is to report the ratios of the three diameters reported above, as this gives a measure of the quality of the crystallite. However, one needs to also bear in mind that at the present time most theoretical treatments of nanocrystals avoid the issue of morphology altogether and deal with nanocrystals as spherical particles [22] with at best slight deviations from spherical symmetry [11]. This approach results because these treatments are rooted in bulk electronic properties where crystallite shape plays no role, and because present-day samples generally lack the monodispersity required to discern effects due to shape details. For such a treatment it is sufficient to report the average diameter of the crystallite. For crystallite shape to matter, one needs to approach the problem from a molecular point of view as done by Hill. [23] This will become more important as single-nanocrystal spectroscopy is now probing very fine electronic detail as well.

A more meaningful aspect ratio can be obtained for the crystallite in Figure 2.15 (b). The distance between horizontal rows of channels is the 0.3505 nm {002} spacing. The zigzag pattern between rows is typical of the wurtzite structure. The spacing between channels within the rows is once again the {100} lattice spacing of 0.37238 nm. Counting as before, the height of the nanocrystal is nineteen {002} spacings. There is a twin fault near the top of the nanocrystal, but this particular fault, a single layer of zincblende type stacking, does not affect the {002} spacing. Meanwhile, the width at the equator is seventeen {100} spacings. From this, the size of the nanocrystal is 6.7 nm tall by 6.3 nm wide. This yields an aspect ratio for this particular crystallite of 1.05. However, if one accepts the hexagonal shape from Figure 2.15 (a) as universal, one can also infer the aspect ratio when the width is measured along the <100> direction, that is if the nanocrystal were oriented along [210]. To do so one merely uses the fact that the apex-to-apex diameter (along the <100> direction) is 1.15 times larger than the diameter between opposite faces (perpendicular to {100} planes).[1] This relation, and the orientation of the nanocrystal to the electron beam are illustrated in Figure 2.16. This alternate aspect ratio is 0.92. Hence it is important to specify which aspect ratio one is reporting in HRTEM. By comparison, CDF does not distinguish between the two orientations in Figure 2.16 if the 002 reflection is the diffraction condition. This may introduce some error into CDF measurements that is absent from HRTEM, and once again points out the difficulty of reducing low-symmetry objects to a few numerical parameters. This error may be removed by changing the diffraction condition. However, since ring diffraction patterns are the norm and only a few orders are seen with sufficient intensity, it is difficult experimentally to select a single diffraction condition.

An examination of the available HRTEM data for the same sample presented in the CDF study gives the histograms in Figure 2.17. Only 16 data points could be assigned so no firm conclusions can be drawn. The data does seem to correlate well with the TEM data on a qualitative level. The size distribution is sharper in the minor diameter and the peaks of the distributions approximately align with their CDF counterparts. The aspect ratio peaks at 1.15 and tails out to larger numbers. More statistics are clearly needed to assess the relative merits of CDF versus HRTEM sizing.

---

[1] The notation tends to confuse. Because of the hexagonal unit cell, the <100> direction is NOT perpendicular to the 100 planes. This confusion does not arise if one uses the four-coordinate Miller Bravais indices.

Discrepancies have been reported between HRTEM and SAXS measurements. [25, 26] Those studies have consistently found the HRTEM sizes to be smaller than those determined from SAXS. This has been ascribed to the difficulty of determining the edge of a curved particle in the presence of the background signal from the supporting substrate in the HRTEM experiment. The final atom layer at the edge, being very thin in projection, may not generate enough contrast to be visible above the substrate signal. Champagnon [26] used a multi-beam dynamical calculation to show that for thin layer of CdSe in vacuum a layer thickness of ~1nm is required to generate sufficient contrast to be detected by eye. However, our own simulations of wedge-shaped CdS nanocrystals (see Figure 3.1) shows contrast even in the last layer of the wedge, which is a single atom thick. Furthermore, the interpretation of the SAXS data is complicated by the fact that the particle shape and the size distribution are dependent parameters and need to be fit simultaneously. [27-29] At any rate, none of the samples treated in this document were sufficiently monodisperse for accurate SAXS sizing. An alternative TEM contrast mechanism, mass-thickness contrast (in the normal BF mode) does not depend on crystallinity but has been shown [6, 24] to yield smaller sizes relative to SAXS. The discrepancies are on the order of 0.03 nm in the diameter, or about one lattice spacing. While fairly small, this is nevertheless a significant amount in these crystallites, especially the smallest ones, so further study is indicated.

A final note is called for in the interpretation of HRTEM size data. While the measurements are rigorous in themselves, there are potentially different ways of converting lattice spacings to conventional units. The method described treats the diameter as the distance between atom centers on opposite surfaces. This is equivalent to saying that atoms are point objects with no extent. This is clearly not true. A reasonable alternative definition is to extend the diameter defined above with the average radius of the atoms on each side. To a first approximation this can be accomplished by defining the average atom radius to be half the bond length in the crystal structure. Hence, in this scheme all the diameters reported should be increased by one full bond-length (half a bond length on each side of the crystal). One could envision even more sophisticated treatments which account for the different size of surface atoms compared to bulk atoms, surface relaxations, etc. However, based on the data for the bulk surfaces [20] these should be much smaller corrections (1/100's of nm). Furthermore while theoretical calculations based on continuum solid state concepts assume a step function in the potential at the surface, they do not in fact define where that step occurs in terms of atom spacings. In that sense, each of the definitions offered above is a reasonable one, as long as it is made clear that when applied to continuum theories, there is an inherent uncertainty in the diameter on the order of a bond length.

The definition of a diameter is even more difficult for some of the less spherically shaped nanocrystals. For instance, the CdS nanocrystals in Section 2.3 are tetrahedral in shape. It is not obvious how to define a diameter for such a shape[1], and the edge length becomes a more natural choice for parametrizing the size. In general then, the definition of size itself has to be narrowed down when dealing with non-spherical particles. Some other implications of morphology will be addressed in the following sections.

2.2.2 Nanocrystal morphology

As one can see from the issues arising in sizing, the assumption of quasi-spherical particles is a poor one for many nanocrystals. Indeed, there is no a priori reason to expect that nanocrystals should be spherical as the crystal lattice does not possess that symmetry. Instead, one can use the projected structures from Figure 2.15 to postulate a three-dimensional structure for a CdSe nanocrystal. In particular, Figure 2.15 (a) clearly shows

---

[1] Two possible definitions are, the distance from an apex to the midpoint of the opposing side, or the distance between the midpoints of opposing edges. Both are reasonable definitions, but they differ by 14%.

that the nanocrystal is faceted along {100} planes, resulting in the hexagonal shape. Similarly, Figure 2.15 (b) shows faceting to occur along the {001} planes at the top and bottom of the nanocrystal. Additionally the sides in the equatorial region in Figure 2.15 (b) indicate faceting along {100} planes. The transition from the equator to the poles does not show any clear evidence of a unique surface plane. Rather it appears to be mediated through some sort of stepped or disordered surface. This leads us to postulate the nanocrystal shape shown schematically in Figure 2.18. The basic shape is that of a hexagonal prism with {001} surfaces top and bottom, and {100} surfaces forming the sides. The right angle edges of the prism have been tapered off, resulting in the surfaces shown. Based on the angle between the endpoints in the HRTEM micrographs these are assumed to be {101} or {103} surfaces or a combination of such surfaces. However, the HRTEM images are not clear on this point and these surfaces could be significantly reconstructed or disordered. It should be noted that in any given micrograph, all the nanocrystals exhibiting cross fringe contrast share these basic features. For example, Figure 2.19 shows all the nanocrystals with cross fringe contrast from the same negative as Figure 2.15 (a). In each case the observed faceting supports the model presented here. Other samples have the same basic morphology, as shown in Figure 2.20 (the sample used for the CDF size analysis) and Figure 2.21.

The observed shape can be explained from the Wulff theorem and some reasonable assumption about surface energies. The Wulff theorem can be stated as such: A crystalline solid at equilibrium will be faceted along low energy surfaces such as to minimize the total surface energy. The surface area of each facet is inversely proportional to its surface energy.

Unfortunately, surface energies are very difficult to measure experimentally and no data is available for the relevant CdSe surfaces. However, one can use theoretical estimates to at least establish a relative ordering of different surfaces. Oshcherin [30] calculated surface energies for a variety of semiconductor materials using a simple formula that accounts for the areal density of dangling bonds in a surface with a correction for compound semiconductors to account for Madelung effects arising from their ionic nature. The lowest energy surfaces for wurtzite CdSe were found to be the {100} and {001} surfaces. These are surfaces with one dangling bond per surface atom, indicating the importance of this effect relative to ionicity.

In this idealized case the Wulff shape for CdSe nanocrystals would be a hexagonal prism. However, this assumes unreconstructed, infinite surfaces in vacuum. In reality, it is a well-documented fact [20] that semiconductor surfaces reconstruct to lower their surface energies under UHV conditions. Furthermore, the assumption of noninteracting surfaces can hardly be true in the regime of nanometer sized crystallites. Finally the presence of organic ligands on the nanocrystal surface further complicates the analysis, although this at least counteracts the tendency to reconstruct. This latter consideration is particularly important for the polar {001} surfaces which are known to undergo severe reconstructions. [31]

While it is difficult to postulate the equilibrium crystal shape (ECS) for a CdSe nanocrystal from first principles, a rational argument can be made that the shapes observed in HRTEM do represent the ECS, starting with the hexagonal prism.

To begin with, adsorbates counteract the tendency of a surface to reconstruct if they remove dangling bonds from the surface. [20] Thus, the presence of the capping ligands should suppress any severe reconstructions. The capping group used with the CdSe studied was trioctyl phosphine oxide (TOPO). TOPO is not ideal in that its large size makes it sterically impossible to saturate all surface dangling bonds. Additionally, as might be expected from its Lewis Base nature, it preferentially binds to Cd sites on the surface. [13] The following analysis considers the effect of TOPO on each surface separately.

The {100} surface reconstruction has been studied [32] and shown to be mild. Structurally is looks more like a relaxation than a reconstruction. This is a universal feature of this surface[1] for binary tetrahedral semiconductors. [20] It only involves a small bond-length conserving rotation which does not significantly change the surface connectivity or planarity. Its main effect is to shift electron density from the cationic atoms, Cd in this case, to the anionic species, Se here. In essence the surface atoms rehybridize from an sp^3 configuration with a lone electron in each dangling orbital to an sp^2 configuration with an empty p-orbital on the cation and a p^3 configuration with a lone pair on the anion. TOPO binding to Cd is unlikely to have a major effect on this since the empty orbital on Cd is essential for TOPO to form a bond. At best the electron affinity of the oxygen will serve to withdraw some electron density from the Se atom, resulting in a reversal of the reconstruction and a return to the bulk structure.

The situation is quite different for the polar (001) (Cd) and $(00\bar{1})$ (Se) surfaces. In the unreconstructed form these surfaces would lead to large electric fields at the crystal surface. Hence there is a strong driving force for reconstruction. For wurtzite CdS this has been shown to lead to large-scale corrugation of the {001} surface, resulting in a {103} textured surface. [31] The equivalent reconstruction has been observed for the {111} surface of zincblende semiconductors, suggesting a universality similar to that for the {100} surfaces. Yet this reconstruction is never observed in room temperature measurements of colloidal CdSe nanocrystals, which always show flat {001} faces. This suggests that this reconstruction is suppressed by the TOPO bound to this surface. Further support for this hypothesis comes from high temperature HRTEM observations. Figure 2.22 (a) shows a TOPO-passivated CdSe nanocrystal heated to 540°C. This is well above the decomposition temperature of TOPO so the surfaces are assumed to be clean or

---

[1] This same reconstruction occurs with the (110) surface of zincblende type semiconductors. This surface is the zincblende analog to the (100) surface in wurtzite.

partially oxidized (with TOPO as the oxygen source) at this point. The nominal vacuum in the column is 10^{10} torr. Further heating of the nanocrystal leads to the structure observed nine minutes later in Figure 2.22 (b) at 560°C. The upper (001) surface has completely disappeared in favor of {103} facets coming to a sharp point at the top of the nanocrystal. In the process, the {100} side faces have been partially consumed as well. In effect the nanocrystal has been vacuum annealed, forming the {103}-reconstructed (001) surface in analogy to the bulk surface.

Interestingly the bottom (001) surface has not changed noticeably at this point. Since it is chemically distinct from the top surface that is reasonable. If one assumes the top surface to be the Cd surface, then the bottom one is actually the Se $(00\bar{1})$ surface. Lamentably, the HRTEM data shown gives no direct indication of the identities of the opposing surfaces, so this assignment is tentative. It is based in part on the fact that reconstructions on the anionic surfaces have less effect on the planarity of these surfaces. Rather, they proceed by adsorption of adatoms or removal of surface atoms and concurrent in-plane motions of the surface atoms. [20] Thus this reconstruction would have a weak signature in our HRTEM experiment.

Furthermore, it is known that the surface Se atoms in TOPO-passivated nanocrystals are oxidized. [13] Additionally, since the TOPO binds preferentially to Cd, the $(00\bar{1})$ may be assumed to be purely oxide passivated. Therefore the reconstruction process can be assumed to be suppressed in the room temperature nanocrystal in a fashion similar to the (001) surface, except with the oxide acting as a passivant rather than TOPO. Since this bypasses the steric effects of TOPO, this surface is probably extremely well passivated, even though comparison to CdS [33] suggests that the surface oxide is amorphous. Campbell [33] also demonstrated that cleaning the CdS $(00\bar{1})$ surface by argon ion bombardment above 500°C does lead to faceting, with the formation of $(10\bar{3})$ facets near 800°C. Whether electron bombardment at 560°C will have the same effect on CdSe is not known. Presumably the main barrier to reconstruction is removal of surface oxide, driven by the ion bombardment. Given the small scattering cross section of electrons compared to argon ions, it is unlikely that electron irradiation will have this effect, even at 560°C. Nevertheless, this possibility needs to be considered until clear evidence can be obtained for disproving it.

At this point the argument for the ECS of CdSe nanocrystals calls for a hexagonal prism with relaxed {100} side facets and weakly reconstructed or relaxed (001) and $(00\bar{1})$ surfaces. To this one adds consideration of the edge energies between the {100} and {001} type faces. The edge atoms have two dangling bonds as opposed to a single dangling bond for the surface atoms. Since steric effects prohibit TOPO from saturating both bonds this leaves Cd atoms at these edges in a high energy state. Thus there exists a driving force for the {001} surface to form {103} facets at the edges, even in the presence of TOPO. While this argues for blunting the edges of the hexagonal prism, it does not really describe the observed shape very well. The actual transition between the {001} and {100} sides is facilitated mainly by {101} surfaces, not {103}. Furthermore the above argument would predict that the $(00\bar{1})$ surface would not suffer this blunting effect, as oxide would passivate the edge as well as the surface. This can be countered somewhat with the hypothesis that oxidation is not likely to take place until after the nanocrystals have been removed from the argon atmosphere of the reaction vessel. Hence the shape initially formed may be more indicative of a clean surface. A clean surface would favor removal of the edges in order to expose Cd atoms, which can interact with the TOPO in solution. Oxidation may smooth the $(00\bar{1})$ surface afterwards but not remove the edge curvature. More detailed knowledge of the interaction energies between {100} and {001} surfaces is clearly needed for a cogent discussion of the origin of shape at the nanocrystal edge. Corner energies should also be included, and in fact, corner-corner interactions may be of significance, especially in the smallest nanocrystals.

One should note that the shapes observed are identical to those seen for CdSe nanocrystals grown in a glass matrix at 700°C over the course of hours. [21] This long annealing process is likely to result in an equilibrium shape for these nanocrystals. While this matrix is very different from the TOPO passivation of colloidal nanocrystals, the similarity in shapes suggests that this is in fact a general ECS for surface passivated nanocrystals. This may however be very different from the ECS for nanocrystals with clean surfaces in vacuum, as evidenced by Figure 2.22.

The question remains why nanocrystals grown in seconds at 350°C in a solution should exhibit equilibrium behavior. The melting temperature of bulk CdSe is 1241°C so that annealing may be expected to occur near 800°C. The melting point does decrease with the size of the crystallite [6], but this should not drop the annealing temperature below 350°C except for the very smallest crystallites. Indeed, as Figure 2.22 shows, insufficient mobility exists for surface atoms to migrate even at 540°C. The growth process itself then must facilitate annealing of the crystallites as they grow in solution. This implies that the growth process is relatively slow after the formation of the initial nucleus. Reagent molecules impinging on the nucleus must not stick immediately but have the opportunity to sample most of the nanocrystal surface and find the optimum position before permanently bonding to the crystallite. Additionally, the surface ligands must be only loosely bound to the nucleus so that incoming reagent molecules can penetrate to the nanocrystal surface. This would promote a layer-by-layer growth mode similar to Frank Van der Merwe (FV) growth of bulk crystal surfaces.[34] This growth mode does appear to be operative based on the results of epitaxially grown core-shell nanocrystals, see Chapter 3. Indeed, details of the growth dynamics are best reserved for that chapter.

2.2.2.a Implications of Nanocrystal Morphology

The observed morphology has consequences for the properties of these nanocrystals. The presence of well-defined surfaces allows for the rational selection of ligands to attach to various surfaces. In principle, the different chemistries of the various surfaces could be exploited to attach different ligands to different surfaces. These different ligands could then act as "handles" for aligning nanocrystals on a substrate or within an array. Similarly it should allow orientational control when linking nanocrystals together by molecular means as done by Alivisatos et. al. [35] The realization of this idea requires the synthesis of proper, surface-specific ligands, which is a challenging proposition and such ligands do not exist at present. However, this is well within the realm of synthetic chemistry and may be a fruitful endeavor in the future. Indeed, if nanocrystals really are to become molecular "lego blocks" for nanotechnological applications, this is a necessary step on that road.

Even in the absence of surface-specific ligands, the shape itself can be exploited to mechanically align nanocrystals. See Chapter 4.

The shape also affects the electronic properties. Most theoretical treatments of nanocrystals view the nanocrystal as a featureless, spherical dot. Additionally, solutions to the wavefunctions are usually found using cubic symmetry of the unit cell [36-38] with deviations from cubic symmetry added perturbatively. [39] This leads to wavefunctions with threefold degenerate symmetry, or T states. However, in a wurtzite lattice, there is an inherent asymmetry due to the unique c-axis of the unit cell. Among other things this makes it impossible for a wurtzite CdSe nanocrystal to have an aspect ratio that is rigorously equal to 1. The wurtzite unit cell also lacks a mirror plane perpendicular to the unique axis. Consequently even in an infinite (macroscopic) crystal, which could approach an aspect ratio of 1, the symmetry is less than T and the electronic states will split into singly degenerate A states aligned with the wurtzite c-axis, and double degenerate E states perpendicular to it. Shiang [16] used Resonance Raman spectroscopy to show that this is in fact the case for these nanocrystals, and that these should be treated not as spherical dots, but as molecules of point group symmetry C_{3v}. Theoretical treatments that take this into account now exist. [40, 41]

This also argues for the possible presence of a ground state dipole in these nanocrystals. This would affect the use of these particles in non-linear optical media. Furthermore, the presence of the polar faces provides a natural route for carrier trapping and charge separation, which may explain some Stark data on these systems. [42, 43] However it remains to be seen if the broken symmetry results in sufficient electrostatic separation for this dipole to be of appreciable magnitude. Recent experiment indicate that it is and results in an appreciable internal electric field. [44]

2.2.2.b Concluding remarks

In conclusion, it has been found that CdSe nanocrystals grown at 350° in TOPO adopt a shape that is consistent with an ECS for a wurtzite structure semiconductor with passivated surfaces. This shape is a truncated hexagonal prism with {001} and {100} facets dominating the morphology. This has definite implications for the chemistry of these particles and may also affect the photophysics.

2.3 Aqueous CdS

CdS nanocrystals can be prepared in an analogous fashion to CdSe nanocrystals. However, they can also be prepared by aqueous ion chemistry and indeed this synthesis method has a long history. [45] We studied CdS nanocrystals prepared by the method of Eychmüller and Mews [46, 47] in the context of the preparation of CdS/HgS/CdS quantum-dot-quantum-well composites.

Aqueous ions serve as precursors. Cd^{2+} ions are obtained from $CdCl_2$ salt, while H_2S gas acts as a source of sulfur. Again, size control is achieved by rapid nucleation followed by slow growth of the remaining precursor material on the newly formed nuclei.

However, in this method, nucleation is controlled by the pH of the solution, which is self-adjusting as the consumption of H_2S lowers the pH below the nucleation threshold. Polyalkylphosphates, derived from their sodium salts, act as passivating ligands.

2.3.1 Morphology

Images of as-prepared CdS nanocrystals are shown in Figure 2.23. The fringe pattern is indicative of zincblende in [110] projection (see Appendix 2-A). While the equilibrium structure is wurtzite, low temperature syntheses, such as this one, usually yield zincblende. The trigonal shape observed in the images is indicative of {111} terminated tetrahedra. This is also supported by the loss of contrast in going from the apex of the triangle to the base, indicating a corresponding decrease in thickness. This is easily seen by the simulation of a Cd-{111} terminated, tetrahedral nanocrystal in Figure 2.23 (e). However, the experimental images also show some loss of contrast near the apex, such that the triangle does not come to a sharp point there. This implies that there is some loss of thickness near the apex, which means that the corners of the tetrahedron are truncated, most likely by the formation of S-{111} facets. Such a truncation should also be visible at the corners along the base of the triangle. This may be the case, but the weak contrast in the experimental images makes it difficult to state so with certainty.

The predominance of {111} surfaces is surprising at first. While this is a low energy surface with one dangling bond per surface atom, it is not the only one. Indeed the {110} surface should be even lower in energy as it is charge neutral.[1] Yet, there is no evidence for the existence of {110} facets in any zincblende CdS nanocrystals. Furthermore, the tetrahedral shape also implies that one of the polar {111} faces, either Cd terminated or S terminated, dominates over the other. A priori, one would expect a stoichiometric, {111} terminated zincblende nanocrystal to have an octahedral shape

---

[1] By comparison, the (110) surface corresponds to the (100) surface in wurtzite, whereas zincblende (111) is equivalent to wurtzite (001).

which would project in [110] as a rhombus as seen in Figure 2.23 (f). Yet, only a small fraction of nanocrystals are observed with this shape and roughly 75% of all nanocrystals are tetrahedral.

A clue to this statistical imbalance may be obtained from the literature on inorganic molecular clusters. These molecular systems are truly monodisperse in both size and shape and have been analyzed by single crystal x-ray diffraction, so atomic positions are known for the nanocrystal, as well as the ligands. CdS zincblende nanocrystals prepared as molecular clusters [48-50] always exhibit tetrahedral morphology. These clusters are terminated in Cd-{111} surfaces with thiolate ligands passivating the surfaces. It is these charged ligands which neutralize the charge on the polar surfaces. In fact, in these clusters, the ligands are explicitly included in the formula. For instance, the 1.5 nm diameter nanocrystal in reference [48] is described as $Cd_{32}S_{14}(SC_6H_5)_{36}$•$DMF_4$. The 36 thiophenolates exactly compensate the formal charge on the $Cd_{32}S_{14}$ core. The positions of the sulfur atoms are in fact rigidly fixed to the core and may be considered a part of the nanocrystal itself.

The polyphosphate ligands used in our work are not likely incorporated into the CdS nanocrystals both because of their bulk and their different chemical nature. However, they are in fact negatively charged species and thus should interact more strongly with a cationic surface than with an anionic one. Hence they would stabilize Cd-{111} surfaces preferentially. This should result in a stoichiometric imbalance in the nanocrystal. Unfortunately, we were not able to verify this using conventional analytical tests due to the small amount of sample available from a typical synthesis. Indirect evidence of the presence of Cd on the surface comes from the epitaxial growth experiments of Mews [47] which proceed via substitution of surface Cd by Hg ions in solution. This resulted in closed shells of HgS, which implies a Cd-rich surface to begin with. This is discussed in more detail in Ch. 3.

The tetrahedral shape persists to large sizes. Figure 2.24 shows CdS nanocrystals grown to ~10 nm in size. The growth is accomplished by dialyzing sample solutions overnight in water. This exchanges sodium ions in the sample for protons. The accompanying change in pH increases the solubility of ions, which in turn accelerates Oswald ripening. Such a growth process will favor the formation of the ECS as the rate of dissolution is greatest on the least stable surfaces. [51]

At this size, the shape of the nanocrystal is no longer blurred by the capping groups and there is a pronounced tendency for the particles to lie with one of their faces flat on the substrate. Accordingly the majority of nanocrystals look like the triangle in Figure 2.24 (a). The crystallite is lying in [111] projection. One of the {111} faces is parallel to the substrate. There are {220} fringes perpendicular to the edges of the triangle, see the inset. The mass-thickness contrast increases towards the center of the crystallite, consistent with tetrahedral morphology.

On occasion other projections are still observed such as the [110] projection in Figure 2.24 (b) or the [100] projection in Figure 2.24 (c). However these are rare and likely arise from deformation of the tetrahedral shape due to defects such as the twin faults surrounding the tetrahedral core in Figure 2.24 (b). Similarly the outline of the shape and the thickness contrast in Figure 2.24 (c) are still consistent with a tetrahedral crystallite in [100] projection. On the other hand, for a tetrahedron to exhibit this projection requires that it stand on edge. This can only be if it is propped up by another particle, or if the crystallite itself is deformed at the edge so as to increase the contact area with the substrate.

2.3.2 Remarks

It is improper to ascribe an ECS to the CdS nanocrystals observed here, as the zincblende structure is by definition not at equilibrium compared to the wurtzite structure, at standard pressure and temperature. Nevertheless, within the constraints of the imposed crystals structure and surface ligands the Wulff theorem applies. The tetrahedral shape of zincblende CdS nanocrystals demonstrates the importance of the surface ligands in determining the nanocrystal morphology. This can be exploited synthetically by modifying the surface ligands to selectively stabilize different growth faces resulting in shape control as well as size control. [52, 53] Moreover, the stoichiometric imbalance may have implications for the choice of reactant concentrations. In the published synthesis, Cd^{2+} and S^{2-} are used in equimolar amounts. It may be desirable to work with an excess of Cd^{2+} as this would more closely mirror the final composition. Working with an excess of Cd^{2+} should also retard Oswald ripening.

2.4 InP

III-V semiconductors as a group are chemically very different from the II-VI systems discussed so far. One strong distinction is their much more covalent nature compared to the II-VI's. Because of this, aqueous synthesis methods do not exist and these compounds are rarely found in the wurtzite phase. Moreover, the synthesis requires considerably more input of energy to proceed. The basic aspects mirror the synthesis of CdSe nanocrystals except that the reaction requires heating for several days at 300°C. [54] As a consequence, the nucleation step is not as temporally discrete and poor size distributions are obtained. These can be improved post-synthesis by the technique of size-selective precipitation. [15] The nanocrystals are capped with TOPO and soluble in the same solvents as CdSe.

InP is very sensitive to degradation in the electron beam of the TEM. This can be mitigated somewhat by working at lower acceleration voltages (indicating that this is radiolytic damage), so data is collected at 120 kV. Even at this voltage, the sample is not stable enough for CDF sizing, so all size distributions were obtained by the HRTEM method. This is somewhat easier than for CdSe, as the main observable lattice spacing, that of the {111} planes, is unique. On occasion, InP nanocrystals were found to degrade to In_2O_3 nanocrystals which can cause confusion in the interpretation of HRTEM images. Fortunately the largest lattice spacing in In_2O_3 is significantly smaller than the InP {111} spacing so that one can distinguish the two by careful observation of the micrographs.

Another odd feature in these samples is observed in the electron diffraction pattern. While the peak positions match the reflections of bulk zincblende InP, the intensity of the 200 peak is much weaker than expected based on the published powder x-ray diffraction pattern. It is barely visible in the SAD patterns and appears only very weakly in the x-ray diffraction pattern as well. [55] The reason for this is not understood at this time, but may be due to substitutional disorder. The structure factor for the 200 reflection depends on $(f_{In}-f_P)^2$. This difference will be much more sensitive to changes in one of the structure factors than the other reflections which involve sums of the atomic scattering factors.

2.4.1 Morphology

All samples were in the zincblende structure as expected. Figure 2.25, Figure 2.26 and Figure 2.27 show HRTEM micrographs of InP. The nanocrystals shown are in or near [110] projection, showing {111} lattice fringes. The individual images are labelled by the ID of the print[1] they were derived from.

The nanocrystals in Figure 2.25 are shown with their <100> directions pointing up. Some of the images seem to be hexagonal in nature, but in fact, the fringe angles are different from 60°. Rather they show the 70.5° and 50.7° angles typical of zincblende in [110]. Hence the shape is a distorted hexagon or a truncated rhombus. The facets

---

[1] Print numbers are of the form (negative number)-X/Y. Here (negative number) is the number printed on the negative by the microscope and X is a running count indicating the number of prints derived from a given negative. Y is a running count of the digitized images derived from a print.

observed are {111} surfaces on the sides and {100} surfaces on the top. From this observation the 3-dimensional morphology is inferred to be a truncated octahedron as indicated schematically in Figure 2.28 (a). Figure 2.26 displays an alternate morphology. The triangular shapes are the same as those seen with CdS, and these are {111} terminated tetrahedra, as shown in Figure 2.28 (b). These occur less frequently but by no means are they rare. Finally, Figure 2.27 shows a sampling of various misshapen crystallites, including several multiply-twinned nanocrystals (IP4189-1, IP4201-1, IP4204-1).

From these data it is difficult to postulate a unique shape. The truncated octahedron morphology does seem to predominate. However, that shape in itself does not constitute a majority of the particles unless one considers that many of the misshapen nanocrystals contain a partially octahedral core. These particles may have grown from initially octahedral nuclei which developed a stacking defect. Rotation twin faults are commonly observed in tetrahedral semiconductors as they are low energy defects (typically a few to tens of meV per atom). [56] No broken bonds are created at the fault, which is merely a single layer of wurtzite stacking in the otherwise zincblende lattice.[1] Some may also have been created by the fusion of two crystallites with their matching {111} surfaces in contact.

While these faults only carry a small price energetically, they have big effect on the structure. The highest point group symmetry allowed in the zincblende lattice is T_d.[2]

---

[1] The zincblende lattice can be described as a face-centered cubic (fcc) lattice with a two-atom basis. (Similarly the wurtzite lattice is simply a hcp lattice with a two atom basis.) A zincblende lattice has the stacking sequence ABC, which repeats. By comparison, a wurtzite lattice has the stacking sequence AB (and the 111 direction becomes the 001). The energetic differences in the two stacking sequences arise from third-nearest neighbor interactions and are consequently small. A stacking fault is created by a single occurrence of the ABA (or BCB, CAC) sequence within the normal ABCABCABC...stacking. For a more detailed discussion of this see for instance P.W. Atkins, *Physical Chemistry*, fourth edition, p. 634

[2] Even the octahedral particles only have T_d symmetry, as the various faces have different chemical

The introduction of a single layer of wurtzite type stacking, which has C_{3v} symmetry, reduces the point group symmetry of a tetrahedral crystallite to C_{3v}, with a unique axis perpendicular to the fault. If growth proceeds with zincblende stacking in the next layers, the resulting stacking sequence is ...ABCABCA**BCB**ACBACBA... (the fault is indicated by the boldface, the bold **C** indicates the twin plane). In effect the orientations of the domains on either side of the fault have been rotated by 141° about the $[1\bar{1}0]$ axis, which reverses the stacking sequence. This is different from the case of wurtzite, where a C_{3v} fault does not significantly perturb the crystallite since it is already C_{3v}. No new unique axis is created by the addition of the fault, and the domains on either side of the fault have the same orientation, merely translated. In a sense, wurtzite nanocrystals are more "robust" in their shape.

The truncated octahedron shape is a surprising one. All the observed facets are polar. However, unlike the tetrahedral case, in an octahedron there is a stoichiometric distribution of the two chemical species at the surface as opposite faces have alternate terminations (In on one side, P on the opposite face). Even more surprising is the presence of {100} surfaces which, disregarding the surface cap, have two dangling bonds per surface atom. Conversely, the absence of {110} surfaces is puzzling, since, with one dangling bond per surface atom and a stoichiometric composition, they are expected to be much lower in energy than the {100} surfaces. Indeed, the symmetric shape implies that the surface ligands passivate indium and phosphorus equally well. In that case, by analogy to the Wurtzite CdSe case, the morphology should be determined mostly by the surface dangling bonds density resulting in a mixture of {110} and {111} surfaces. Yet no evidence for the formation of {110} facets is seen in any of the micrographs. Such facets, if present, would be visible as vertical side facets in the projection shown in Figure 2.25.

---

terminations.

A possible justification can be found in oxidation of the nanocrystals. This is known to be occurring upon exposure to air and may be several layers deep.. [54] All TEM specimens were prepared in air and oxidation could affect the shape if it is deep enough. The whole issue is complicated by the instability of the nanocrystals in the TEM, which may also affect the shape observed. While care was taken to minimize beam exposure of the particles, this effect cannot be discounted. It may be necessary to cool the specimen in the microscope and/or overcoat it with carbon as described on page 14.

2.4.2 Remarks:

InP nanocrystals have unique structural features that set them apart from the II-VI systems. At present, discussion of the morphology is complicated by experimental difficulties.

2.5 InAs

InAs nanocrystals are prepared similarly to InP nanocrystals, but are terminated in TOP rather than TOPO. An alternative method, similar to the synthesis of CdSe, exists now as well, but most of the particles shown were prepared by the old method. [55] Based on the limited data available, the two syntheses produce essentially identical results when looking at the nanocrystal structure.

InAs is even more sensitive to beam damage in the microscope than InP. InAs degraded in the microscope on a timescale too short to even take HRTEM pictures. When coated with carbon, the particles were stable for a few minutes. Using the low-dose method described previously, this allowed HRTEM data collection, without any noticeable deterioration. CDF imaging failed, with the sample signal visibly deteriorating over the long exposure times necessitated by the low signal strength. Unlike InP, InAs was observed to always degrade to amorphous material. This generally remained nanoparticulate in nature, but without diffraction information no identification of this phase could be accomplished. Attempts at using EDX to determine the chemical composition failed due to the weak signal obtained from the thin samples. However, no determined effort was made to optimize the specimens for EDX operation. [1] Alternatively EELS may be a more successful technique here.

2.5.1 Morphology

Due to the extreme beam sensitivity it is very difficult to obtain good HRTEM images of InAs. Some are shown in Figure 2.29. Again, the crystallites are shown in [110] projection with their <100> axes pointing up. Overall the shapes are similar to the InP case. One sees mostly {111} surfaces and some {100} facets, which suggests again a truncated octahedron structure. Albeit, the paucity of high quality data forbids any definitive assignment.

2.6 Si Nanocrystals

Si nanocrystals were prepared in our laboratory by the method of Littau. [57] This yields a large range of sizes, including some very large nanocrystals. The nanocrystals are passivated by an amorphous silicon oxide layer on the surface and soluble in ethylene glycol. These samples did not stick well to carbon film. Specimens were prepared with the glow-discharge technique or alternatively, by letting a drop of solution evaporate completely while sitting on a grid.[2] Even so, coverage was sparse and only a few crystallites could be examined for each specimen within a reasonable time frame.

---

[1] Since the EDX signal scales with the amount of material in the beam path, a thick specimen yields a better signal. With nanocrystals this could be accomplished by depositing several layers of nanocrystals. Such a specimen would be unsuitable for structural characterization by HRTEM. However, the degradation process can be monitored from the SAD pattern. On the other hand, this would still require very long collection times (typically 1+ hours) and it may be that this would change the nature of the material even more.

[2] This has to be done overnight and can be aided by some mild heating in an oven. Samples should be placed in an enclosure to avoid dust contamination.

However, all samples were stable in the microscope under normal imaging conditions so that no images were lost due to sample degradation. Some of the larger samples were used as diffraction standards for calibration of the TEM camera length.

2.6.1 Morphology

The crystallite in Figure 2.30 (a) is representative of the nanocrystals obtained in this synthesis. It is shown in [110] projection with a $[1\bar{1}1]$ axis pointing horizontally. The particle is quasi-spherical, but still exhibits some faceting along {111} surfaces (top and sides). A rotation twin plane traverses the crystallite in the center. In all, 20 crystallites exhibited sufficient cross-fringe contrast for analysis. These ranged in size from 2.5 nm to ~20 nm in diameter.

Large particles (>10 nm) were quasispherical as seen in Figure 2.30 (a). Smaller nanocrystals exhibited a more strongly faceted shape, Figure 2.30 (b). {111} surfaces dominated in all cases, but {100} also occurred frequently. {110} facets were also observed occasionally but infrequently. This ordering is consistent with the relative energies of these surfaces in vacuum. [58] In Figure 2.30 (a) the transition from the top {111} surfaces to the side {111} surfaces seems to be achieved by a series of steps on {111} surfaces, which overall gives the appearance of a rough {110} surface. The {110} surface exhibits complex reconstructions [59-61] that corrugate the surface and this may be happening here as well.

Images of nanocrystals that straddle an edge in the supporting substrate allow imaging of the amorphous oxide overlayer as seen in Figure 2.30 (d). The {111} lattice fringes in the crystalline core serve as a calibration of the magnification which allows determination of the oxide thickness to be ~2 nm, consistent with reference [57] and other studies on similar nanocrystals. [62-64] The amorphous nature of this film probably serves to smooth out energy differences between different surfaces, hence creating the quasi-spherical shape.

2.6.1.a 111-Twins in Si Nanocrystals

The twin seen in Figure 2.30 (a) is a common feature of these crystallites. An argument can be made that it is ubiquitous. Twelve of the 20 particles observed in [110] projection showed such a twin near the center of the particle. Four of these had additional twinsparallel to the first twin. For these twinsto be observed in [110] projection, the twin plane has to include the [110] lattice vector. There are 12 different <110> lattice vectors. For a twin plane perpendicular to <111> there are six such vectors that include the fault plane: [$1\bar{1}0$], [$10\bar{1}$], [011] and their inverses. [1] In all other projections, the twin plane will be inclined to the viewing direction, and hence the twin plane will not be visible. Furthermore, the twin splits the nanocrystal into two domains and in these other orientations, only one domain will be in a [110] projection. The other domain will be above or below, and in [114] projection. In this projection only the {220} fringes (0.19 nm spacing) are resolved by the microscope. These fringes are near the resolution limit and therefore difficult to see. Moreover, they will be out of focus when the stronger {111} fringes are focussed and thus are likely overlooked unless a through-focal series (TFS) of pictures is collected. Hence, if all nanocrystals contain one twin, statistically one would expect half of the [110] projected lattice images to show the twin. If untwinned crystallites are also present, that ratio should be less.

A larger statistical sample is necessary to validate the claim that all nanocrystals are twinned. The above observation also does not rule out another possible explanation which is that the images without a visible twin correspond to untwinned particles and that all the twinned particles will give images with a twin. This assumes that a twinned

---

[1] To find the various indices hkl (being any set belonging to the family of <110> vectors) that will yield the desired vectors we must satisfy the condition <111>•<hkl>=0.

particle with the twin inclined to the image plane will never give {111} cross fringe contrast. The latter is unlikely however, since fringe contrast has been observed when individual particles are lying on top of each other.

It may be possible to distinguish the two cases by collecting a TFS. The fringe patterns should be different for the two cases and can be identified by performing image simulations of the appropriate model structures. Alternatively, the larger nanocrystals may give sufficient diffracted intensity to employ nanodiffraction or CBED on individual crystallites. These diffraction techniques should directly reveal if one or two domains are present in the crystallite. They may still fail with twin bands such as in the crystallite in Figure 2.30 (e).

Based on the above arguments, it is reasonable to assume that the majority of nanocrystals have at least one twin similar to the one in Figure 2.30 (a). Similar behavior was observed by Iijima in Si particles grown by an arc discharge of Si electrodes in an Ar vapor. [62] These particles were significantly larger than the ones studied by us, covering the range of 20-200 nm in diameter. Nevertheless, these nanocrystals are remarkably similar. They are quasi-spherical and most of the particles have a twin running through the center of the crystallite. Iijima interpreted this in terms of nucleation on a liquid droplet. Albeit, he did not suggest what the critical nucleus size may be, and for the smaller nanocrystals in our study the crystallite size may be perilously close to the nucleus size. A better assumption may be growth by condensation on a solid nucleus. The ubiquity of the twin and its location suggests that there probably exists a universal nucleus, that contains, or promotes, this twin.

For such a universal nucleus to exist it would have to be of remarkable stability. Indeed, gas-phase silicon clusters are frequently observed to be particularly stable for certain magic-number sizes. [65-67] Furthermore, some such clusters are expected to have highly anisotropic shapes. [68] Such a shape creates a unique axis, which is akin to a stacking fault in its symmetry breaking. Kaxiras [69] proposed various candidate structures of particularly stable clusters in the 20-33 atom size range. Some, such as Fig. 1.(b) in [69] already form the core of a faulted diamond lattice. Others, such as Fig. 2.(b) and (c) in the same paper are clusters of D_{3h} symmetry which might promote a twin upon crystal growth. (The diamond lattice has T_d symmetry but the introduction of a twin will reduce this to D_{3h} symmetry, or lower depending on the position of the twin). At present the existence of such nuclei in our synthesis is speculative, but warrants further investigation.

2.6.2 Remarks

Oxide-passivated Si nanocrystals have faceted shapes at small sizes, which evolves to partially faceted, quasispherical shapes at larger sizes (>10 nm). {111} surfaces predominate, but {100} surfaces are also common. Many—possibly all—crystallites have a twin in their center, traversing the entire nanocrystal. This suggests a single common nucleus for the growth of such nanocrystals.

2.7 Conclusions

Colloidal nanocrystals prepared by a variety of techniques adopt shapes that are consistent with Wulff polyhedra. This suggests that these crystallites are at or near their equilibrium crystal shapes. Surface ligands have a big effect in determining this shape and can be used to favor some shapes over others. In the case of Si nanocrystals prepared by an aerosol reaction, the critical nucleus may profoundly affect the final morphology as well.

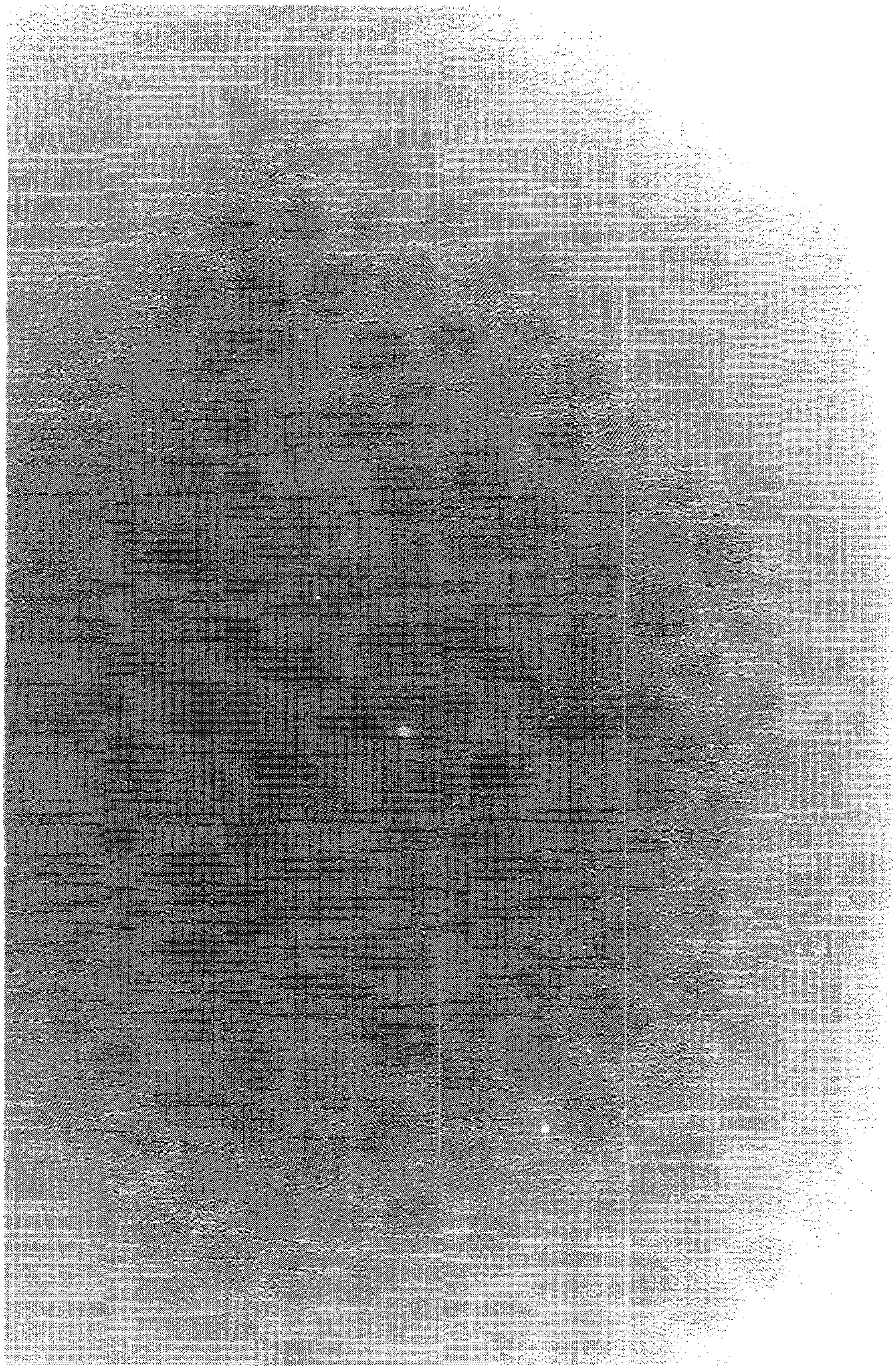

Figure 2.1: CdSe Nanocrystals
BF micrograph of CdSe nanocrystals supported on an amorphous carbon film.

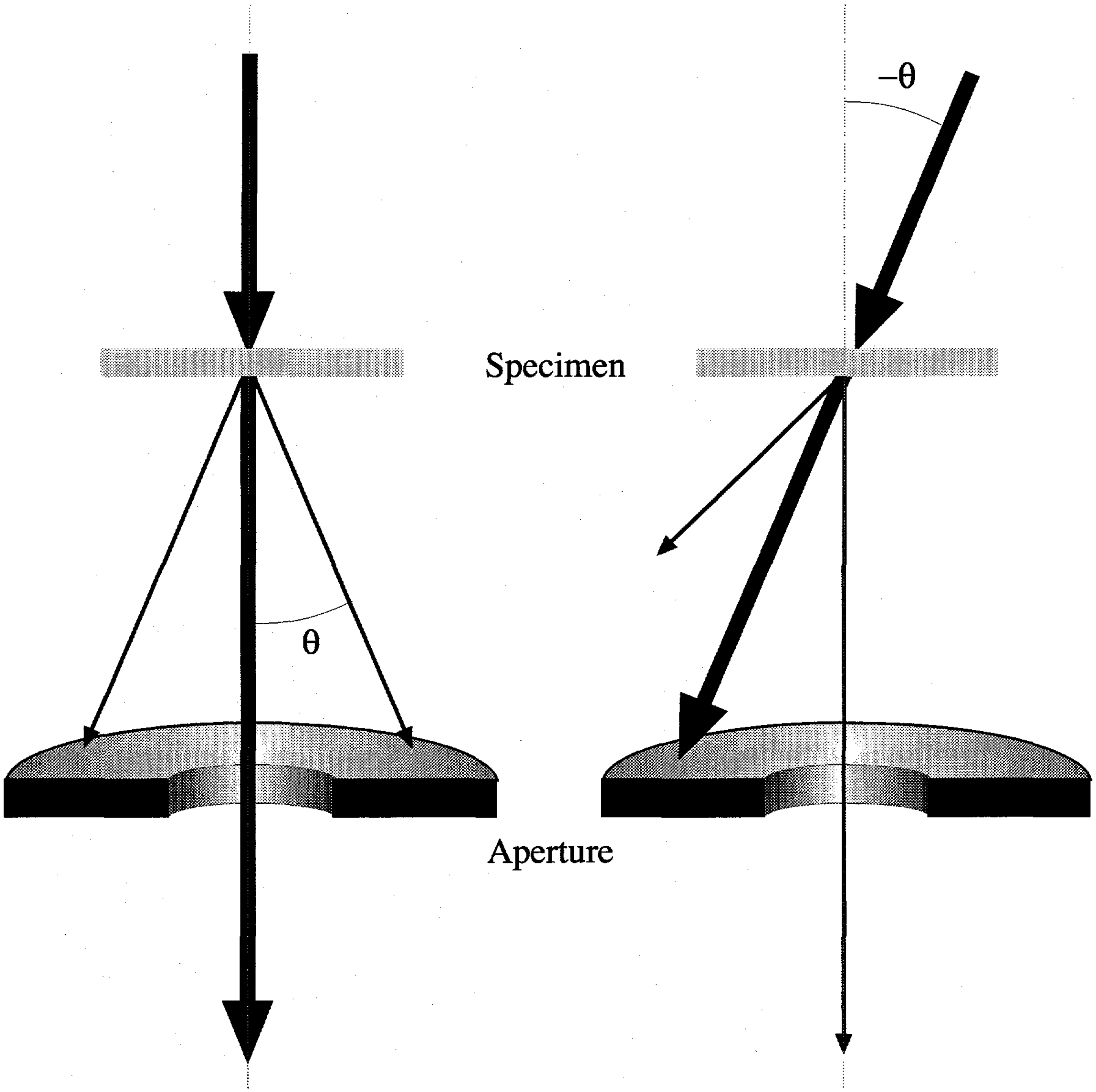

Figure 2.2: Centered-Dark Field Operation of the TEM

Schematic View of CDF operation:

In normal BF operation (left), the incident and direct beams travel down the optic axis (dashed line). The diffracted beams are intercepted by the Objective Aperture (or at high angles strike the TEM column) and do not contribute to the final image, which consists of dark areas corresponding to the projection of the diffracting areas on a bright background.

In CDF, the incident beam is tilted through an angle θ corresponding to the diffraction angle of the desired reflection. The direct beam and the other diffracted beams are intercepted. The final image consists of bright areas arising from the diffracting material on a dark background (with residual intensity arising mostly from incoherently and inealistically scattered electrons).

If a large objective aperture is chosen, more than one beam may reach the detector. Interference between multiple beams may lead to lattice fringes in HRTEM.

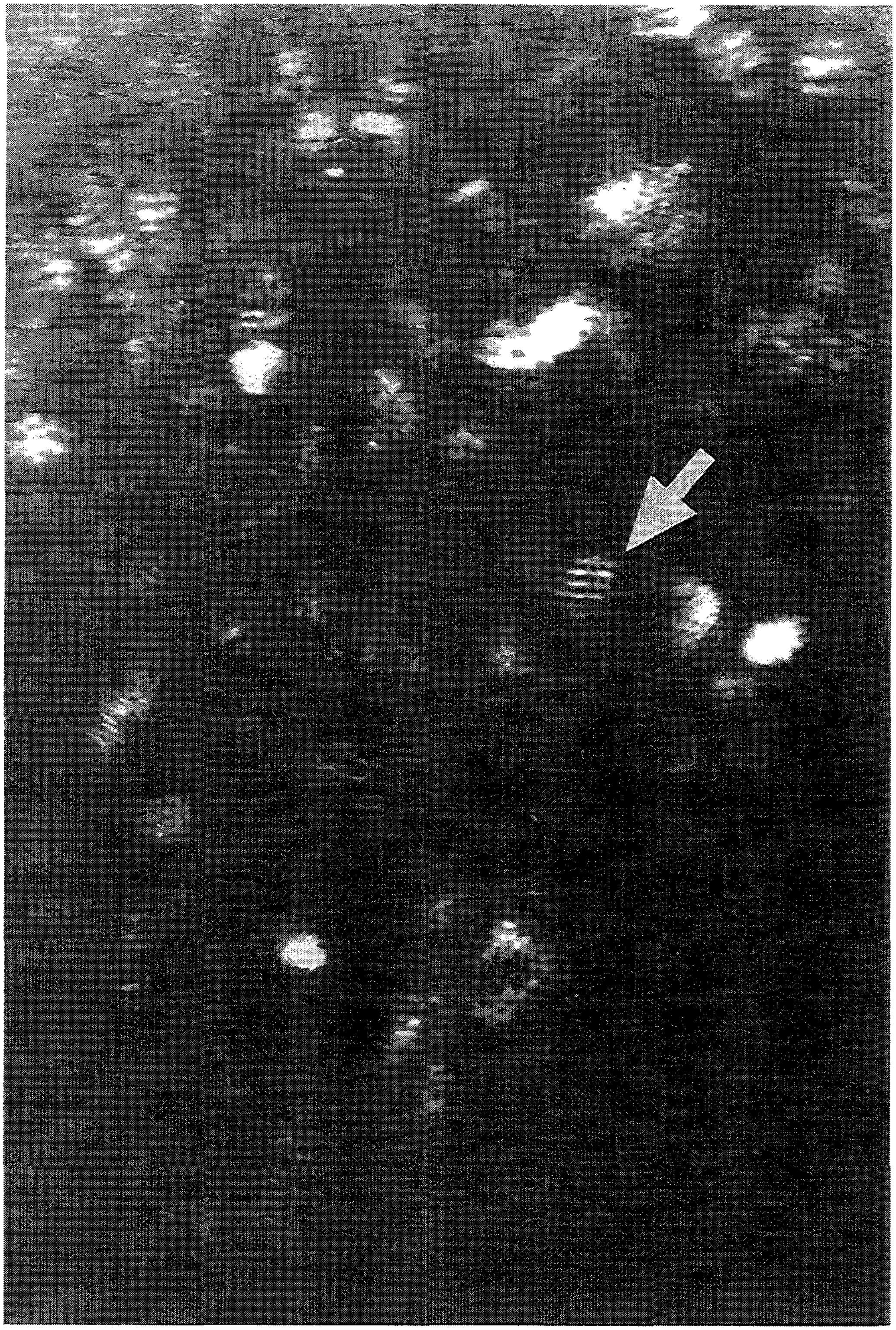

Figure 2.3: CDF micrograph of CdSe nanocrystals

A sample of ~4 nm diameter nanocrystals observed in CDF using an aperture that passes out to ~ 6 nm^{-1}, centered on the second triplet in the CdSe diffraction pattern. The crystallites are the white areas on the micrograph. Some, such as the one indicated by the arrow, show fringe contrast as well.

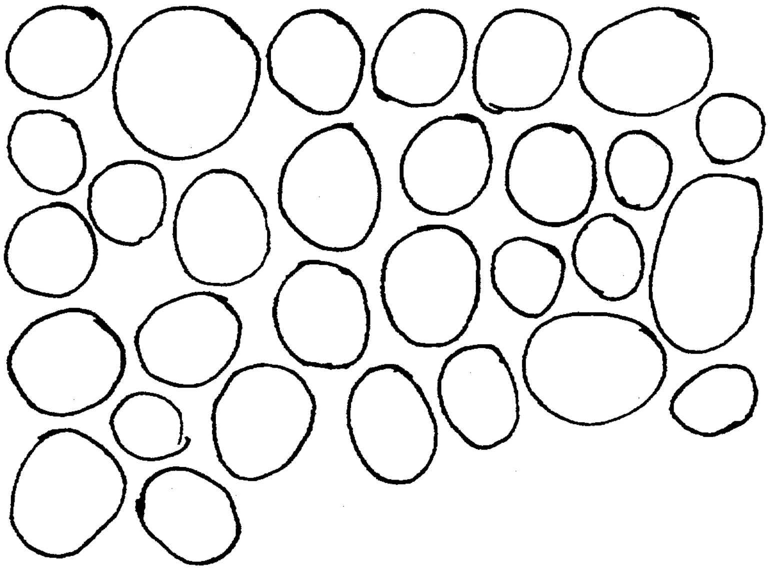

Figure 2.4: CDF Trace of CdSe nanocrystals

Traced outlines from an enlarged CDF negative at actual magnification (approximately 3X that of Figure 2.3). The outlines have been collected to fit onto a single page, i.e. positions in the figure do not indicate positions on the negative. Orientations and sizes have not been altered. At this magnification about eight 8.5" x 11" sheets of paper are necessary to cover a negative.

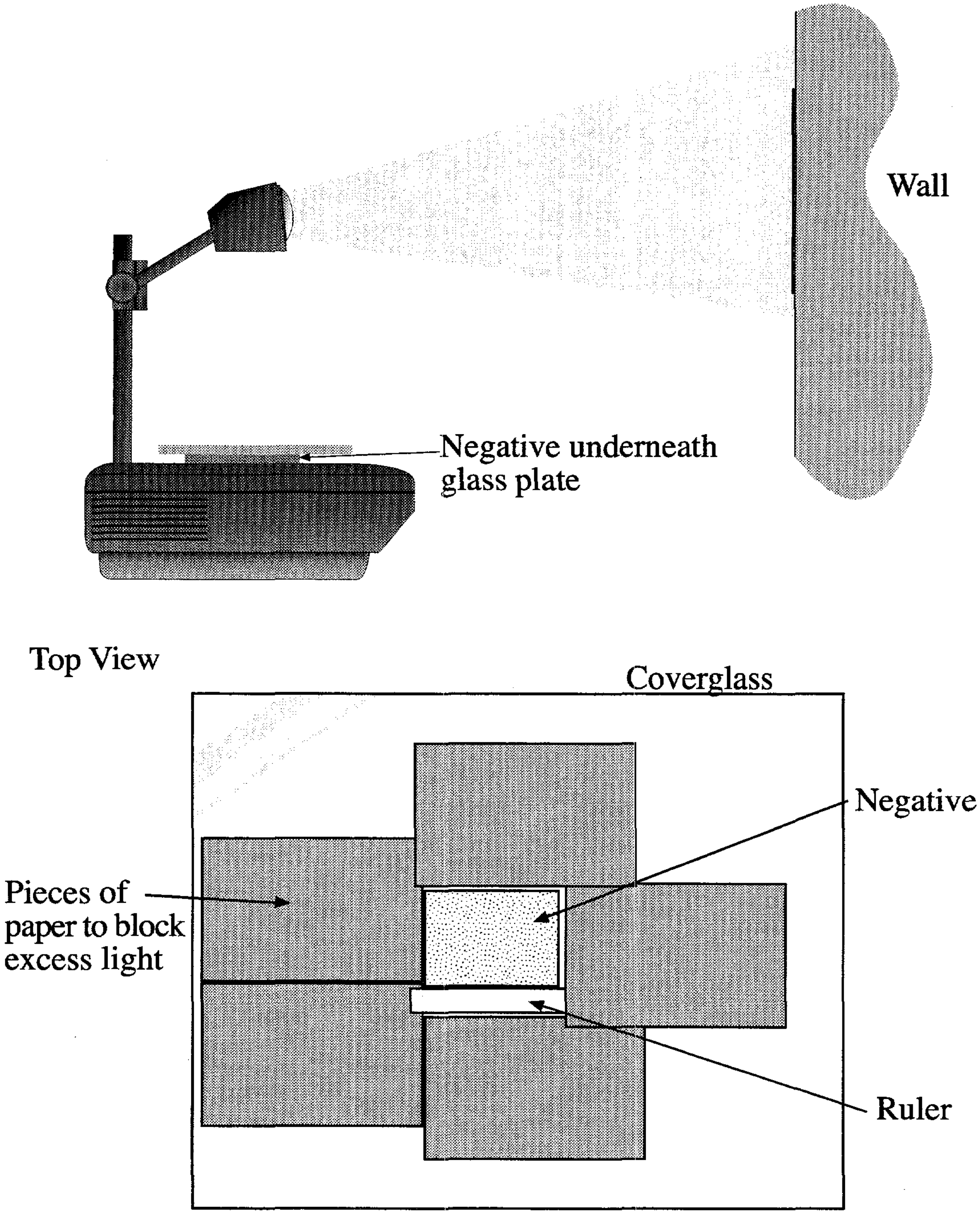

Figure 2.5: Arrangement for Tracing CDF images.

Negatives are projected onto a wall using an overhead projector. To calibrate the magnification, a transparent plastic rulers is placed next to the negative. To prevent curling of the negative from the heat of the projector lamp, a glass plate is placed atop the negative. To minimize excess light in the room, the area of the projector surface surrounding the negative is covered up. The projected image is traced onto sheets of paper, attached to the wall using Scotch™ 811 removable adhesive tape.

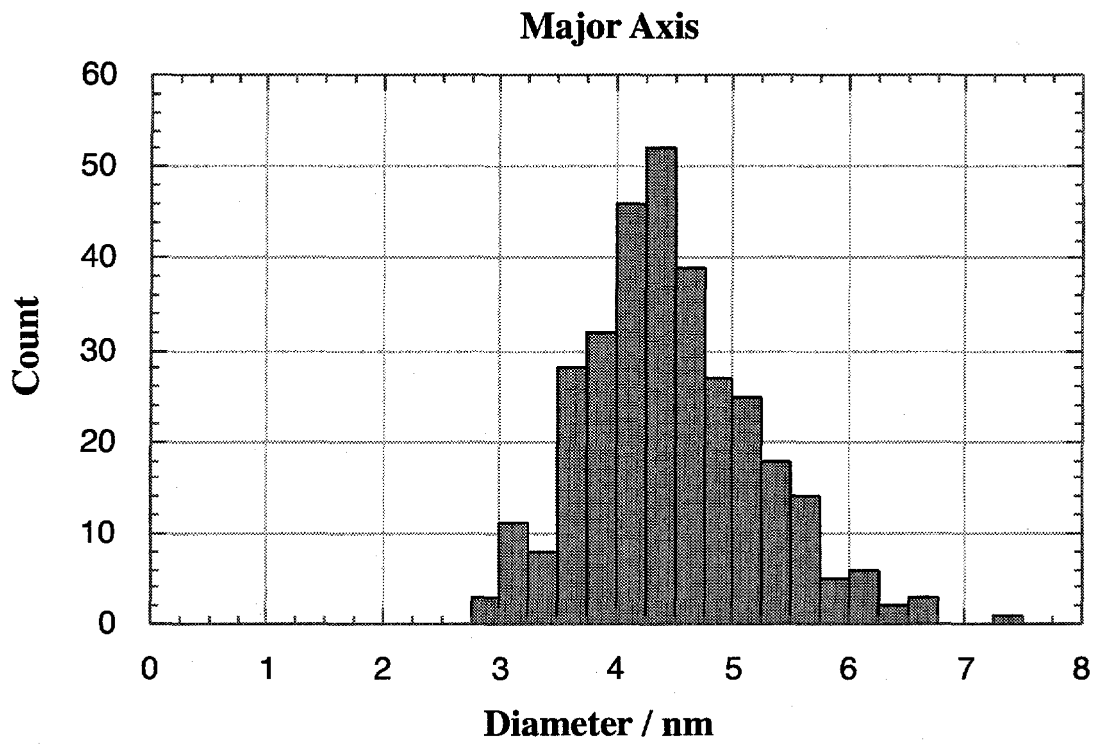

Major Axis

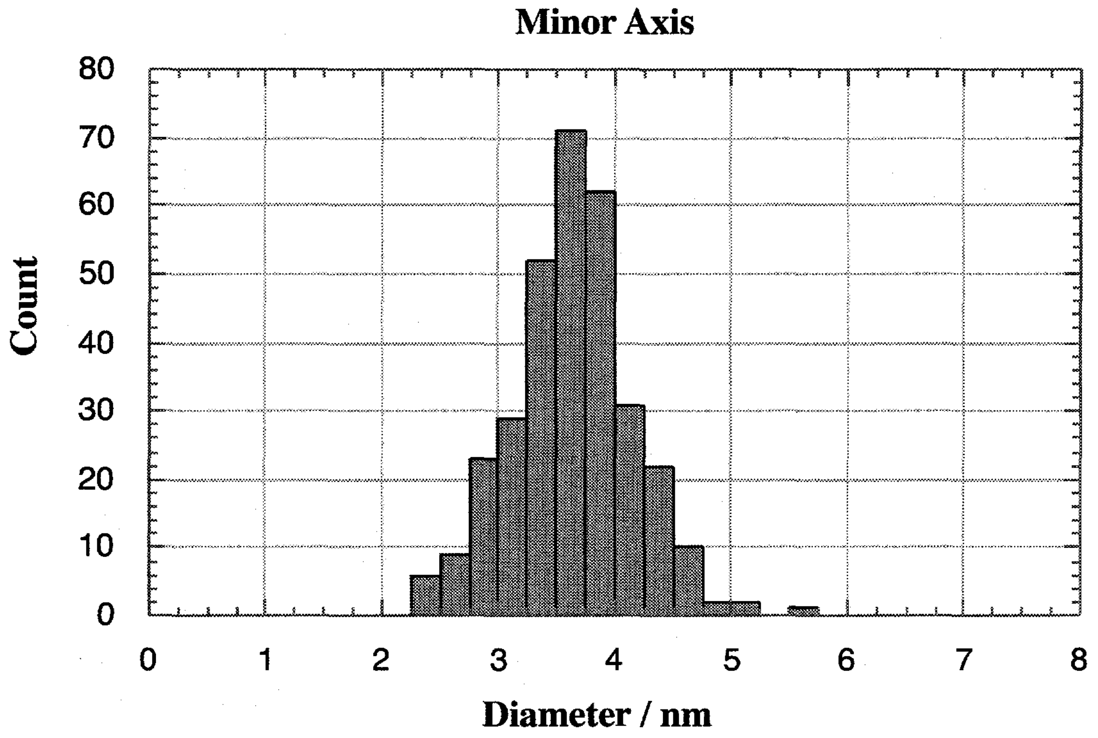

Minor Axis

Figure 2.6: CDF Size Data, using 0.25 nm bins

Size distributions in the major and minor axes obtained from CDF sizing of 320 nanocrystals. Binned in 0.25□nm increments.

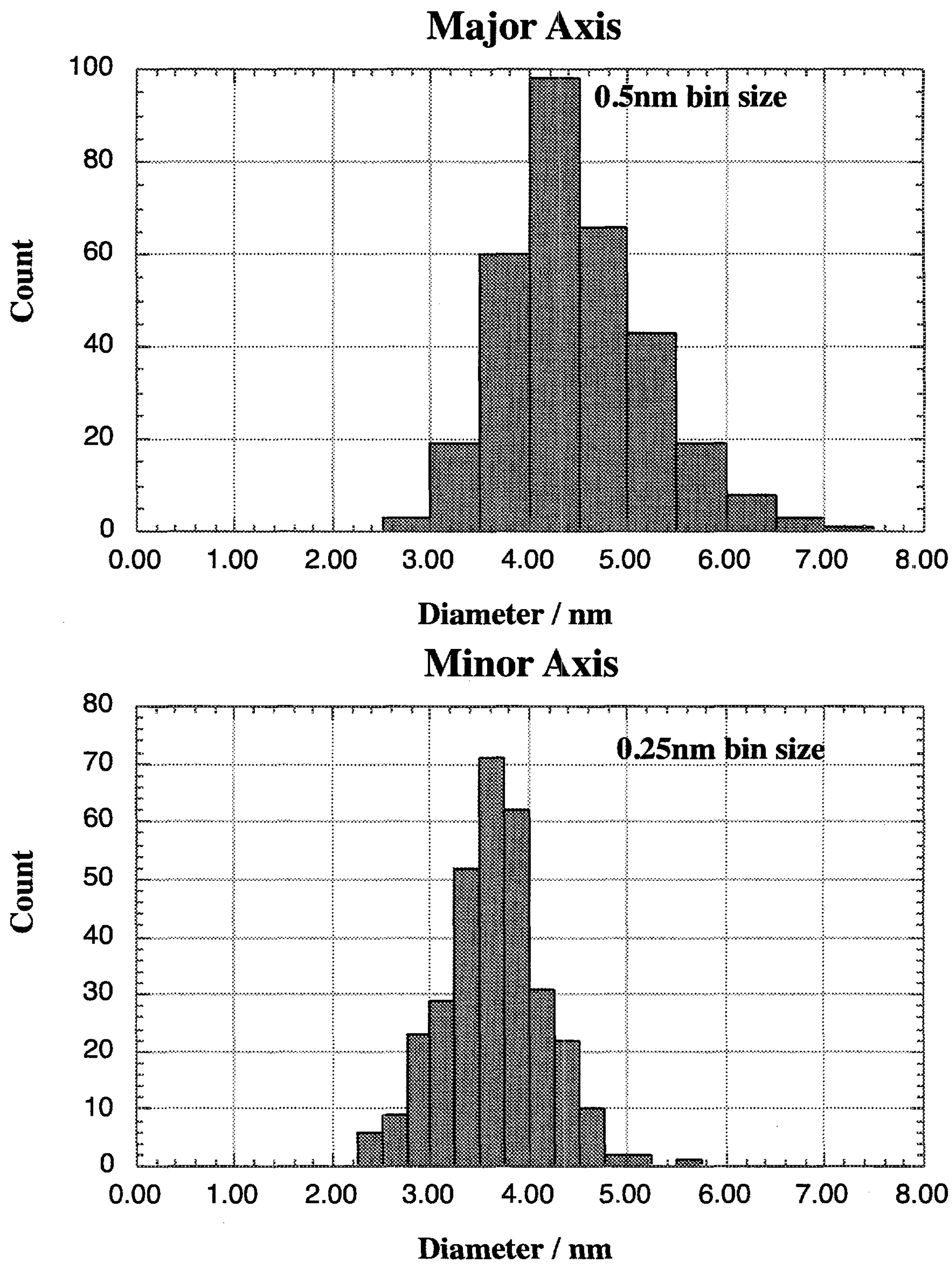

Figure 2.7: CDF Size Data, Automatic Binning

Size distributions in the major and minor axes obtained from CDF sizing of 320 nanocrystals. Binned automatically by Kaleidagraph™ 3.08.

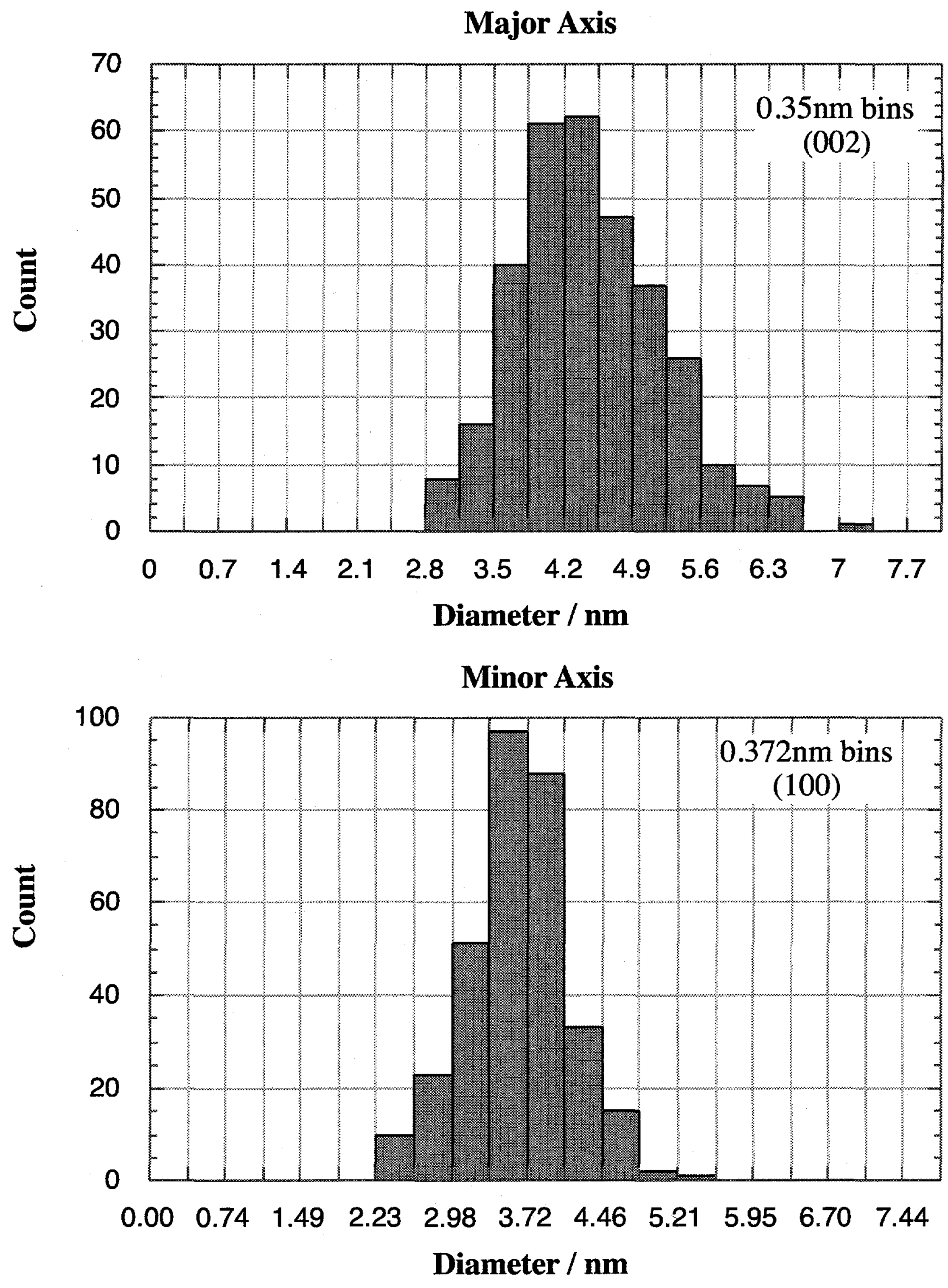

Figure 2.8: CDF Size Data, "Natural" Binning

Size distributions in the major and minor axes obtained from CDF sizing of 320 nanocrystals. Binned in "natural" increments: 0.35 nm (002 spacing) for major axis, 0.372 nm (100 spacing) for minor axis.

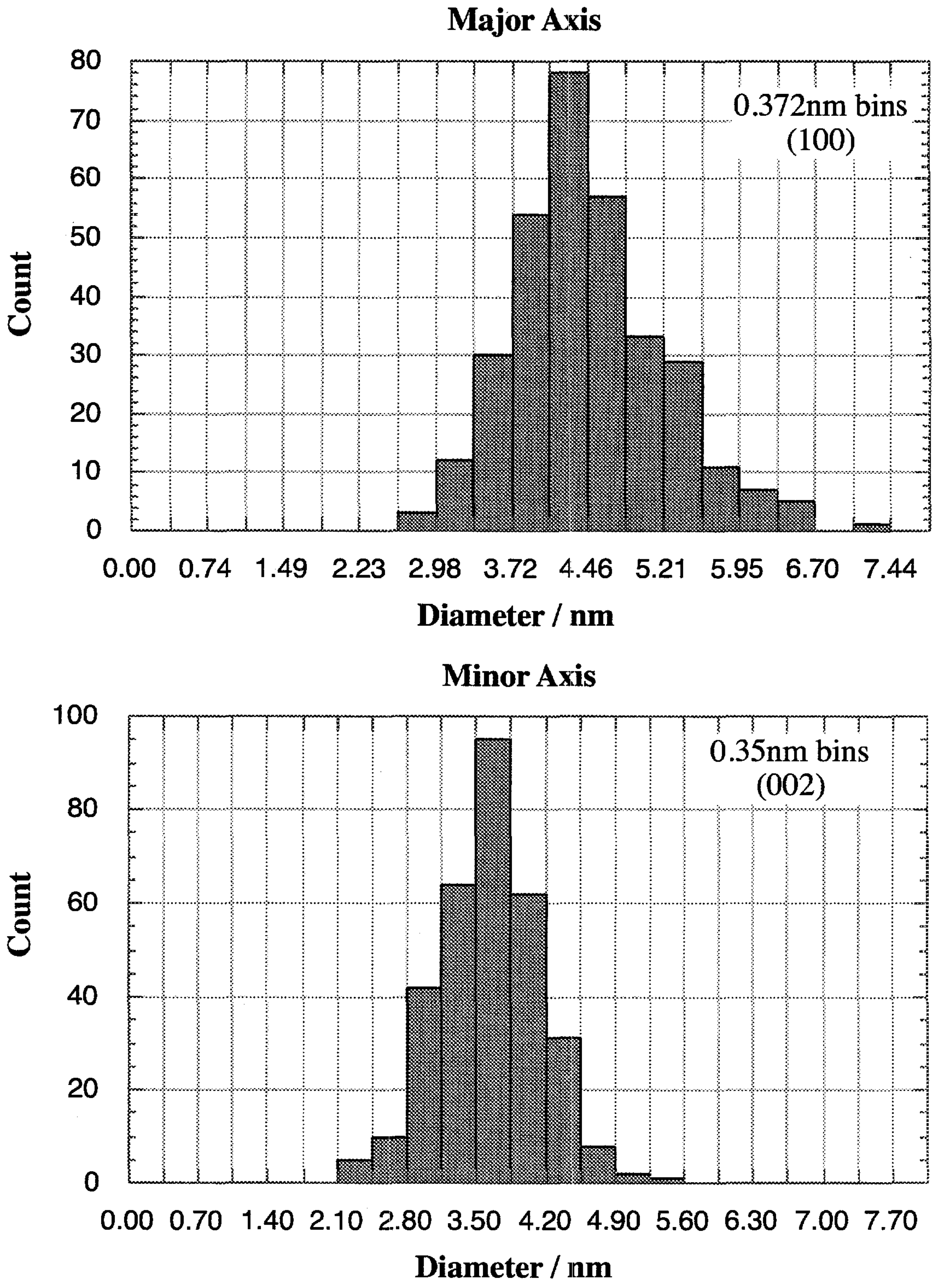

Figure 2.9: CDF Size Data, "Unnatural" Binning

Size distributions in the major and minor axes obtained from CDF sizing of 320 nanocrystals. Binned in 0.372 nm increments (100 spacings) for the major axis, and 0.350 nm increments (002 spacings) for the minor axis.

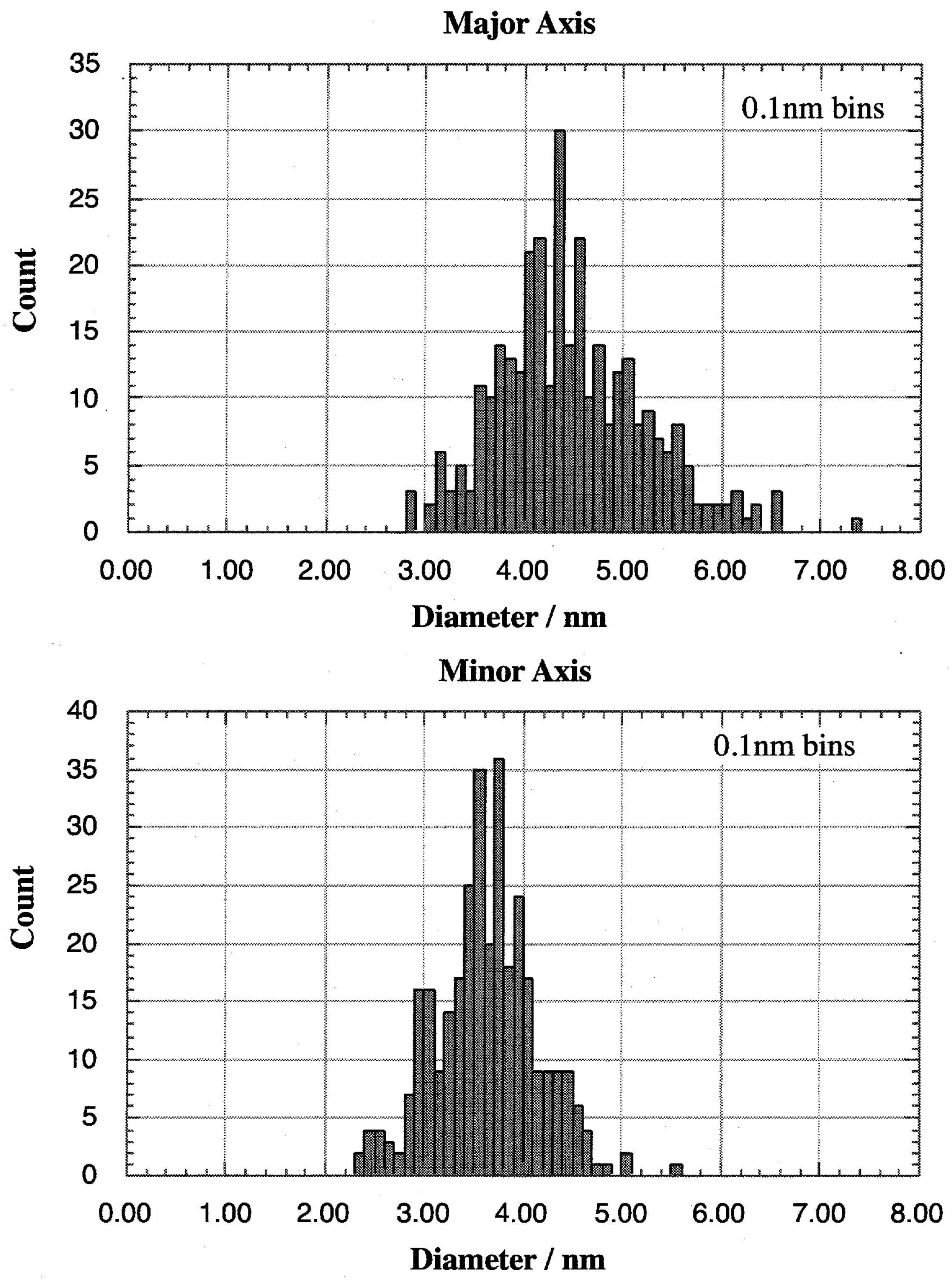

Figure 2.10: CDF Size Data, 0.1 nm Binning
Size distributions in the major and minor axes obtained from CDF sizing of 320 nanocrystals. Binned in 0.1□nm increments.

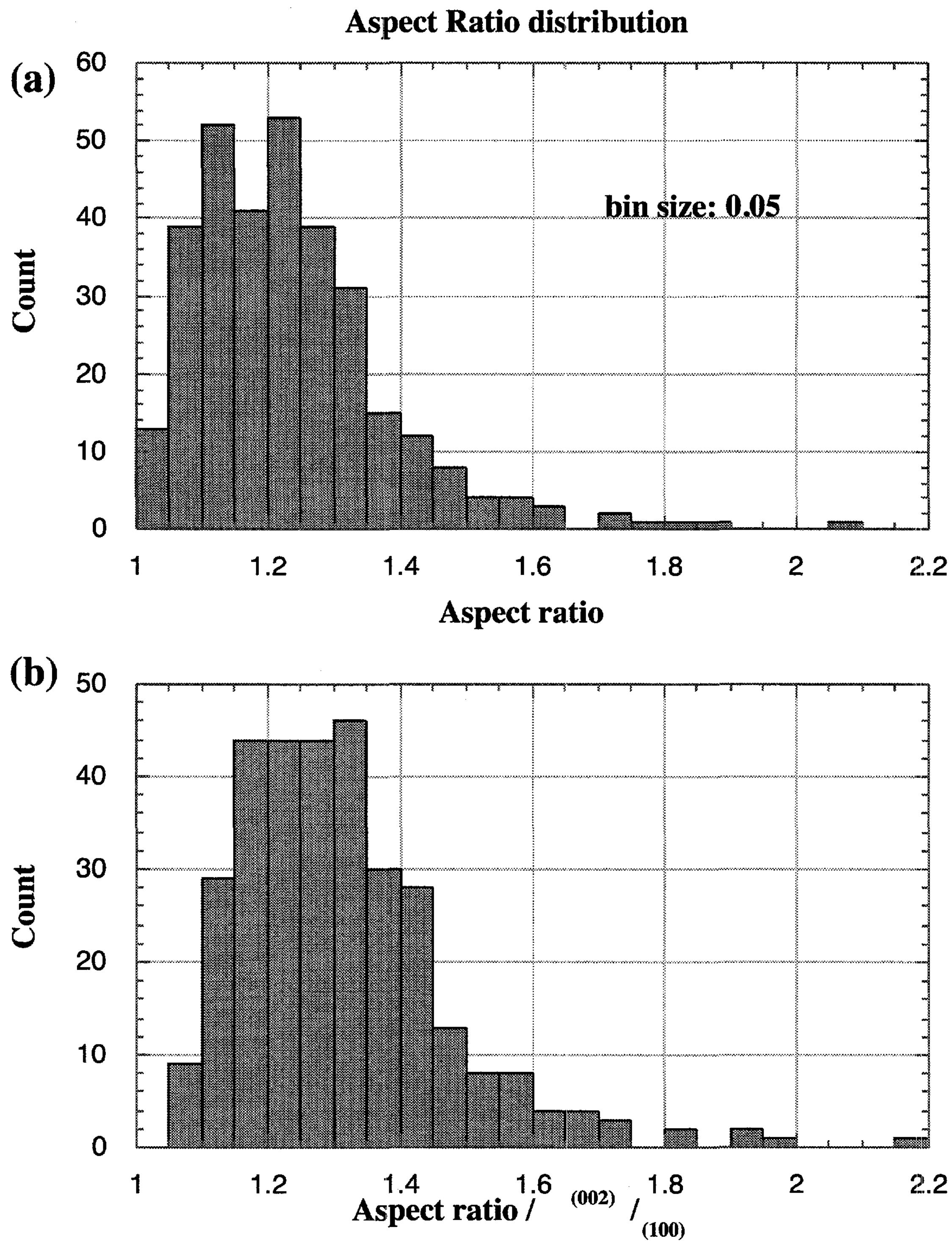

Figure 2.11: Aspect ratios from CDF measurements

CdSe nanocrystal aspect ratios obtained from CDF sizing of 320 nanocrystals. Aspect ratio = diameter of major axis/diameter of minor axis.

(a) Aspect ratio calculated in units of nm/nm

(b) Aspect ratio calculated in units of (002 spacings)/(100 spacings).

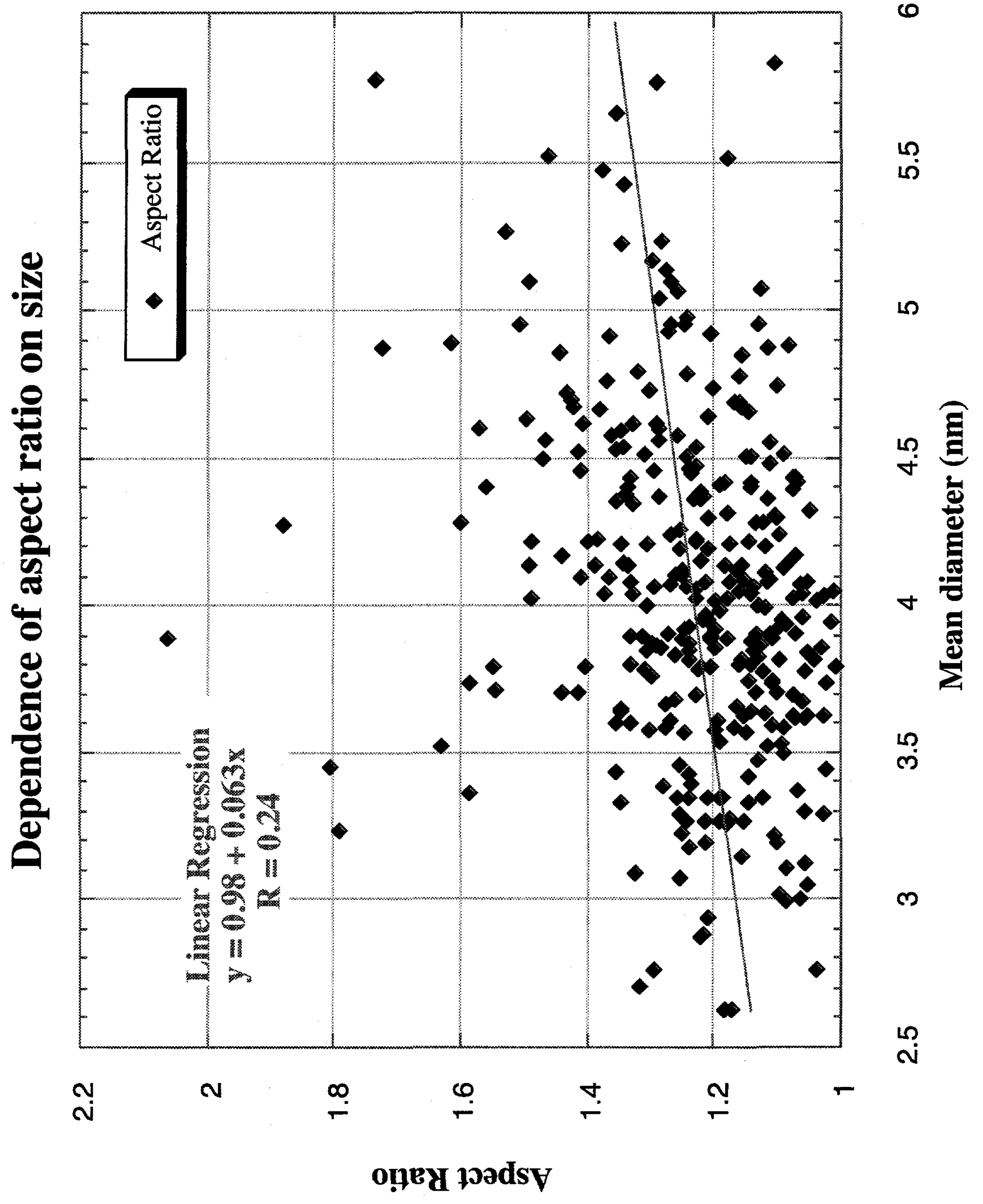

Figure 2.12: Nanocrystal Aspect Ratio vs. Mean Diameter

Nanocrystal aspect ratios (in units of nm/nm) as a function of mean nanocrystal diameter (average of major and minor axis) for CdSe nanocrystals. Data from CDF sizing of 320 nanocrystals. Best fit linear regression is indicated.

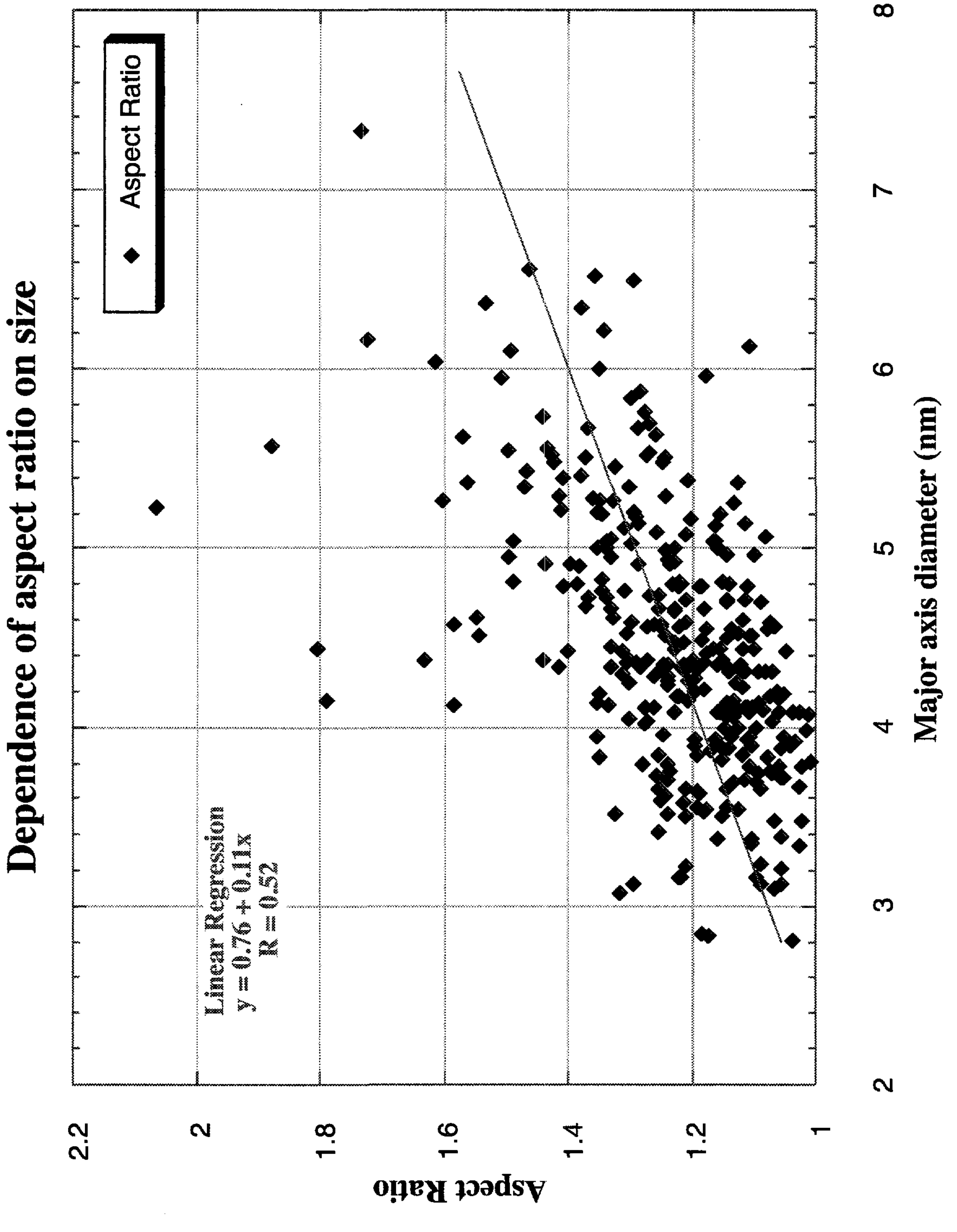

Figure 2.13: Nanocrystal Aspect Ratio vs. Major Axis Diameter

Nanocrystal aspect ratios (in units of nm/nm) as a function of major axis nanocrystal diameter for CdSe nanocrystals. Data from CDF sizing of 320 nanocrystals. Best fit linear regression is indicated.

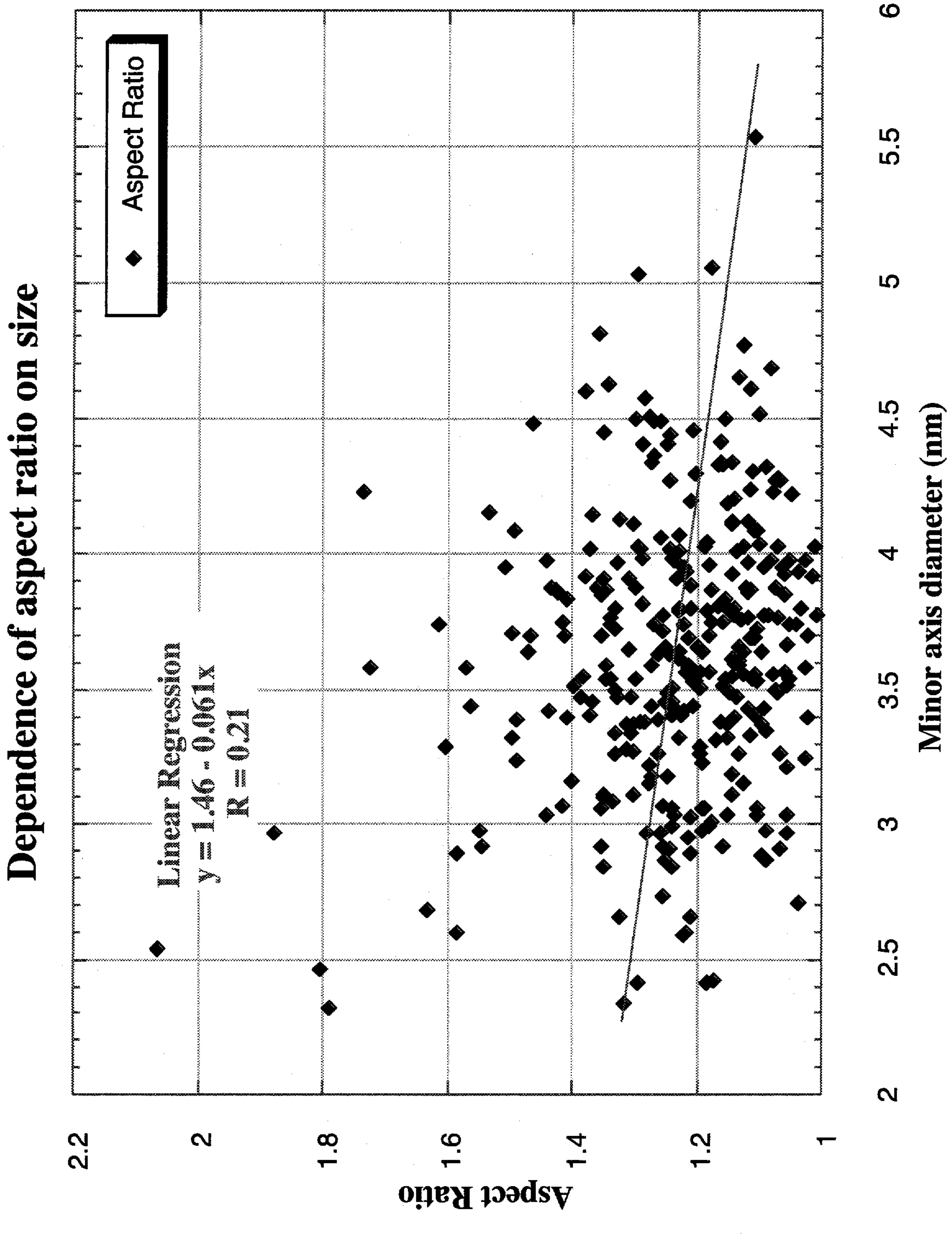

Figure 2.14: Nanocrystal Aspect Ratio vs. Minor Axis Diameter

Nanocrystal aspect ratios (in units of nm/nm) as a function of minor axis nanocrystal diameter for CdSe nanocrystals. Data from CDF sizing of 320 nanocrystals. Best fit linear regression is indicated.

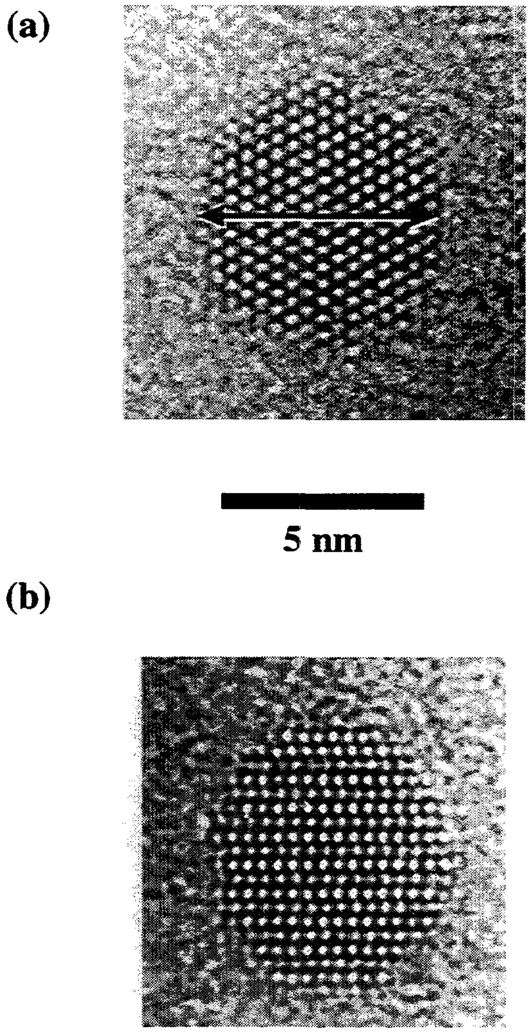

Figure 2.15: HRTEM Sizing of Wurtzite CdSe

HRTEM micrographs of CdSe Nanocrystals. Images taken near Scherzer defocus. The white spots correspond to channels in the crystal structure. The black areas indicate atomic positions. The speckled background is due to the amorphous carbon substrate.

(a) Crystallite in [001] projection. The double arrow indicates the measured diameter (see text).

(b) a different crystallite in [010] projection.

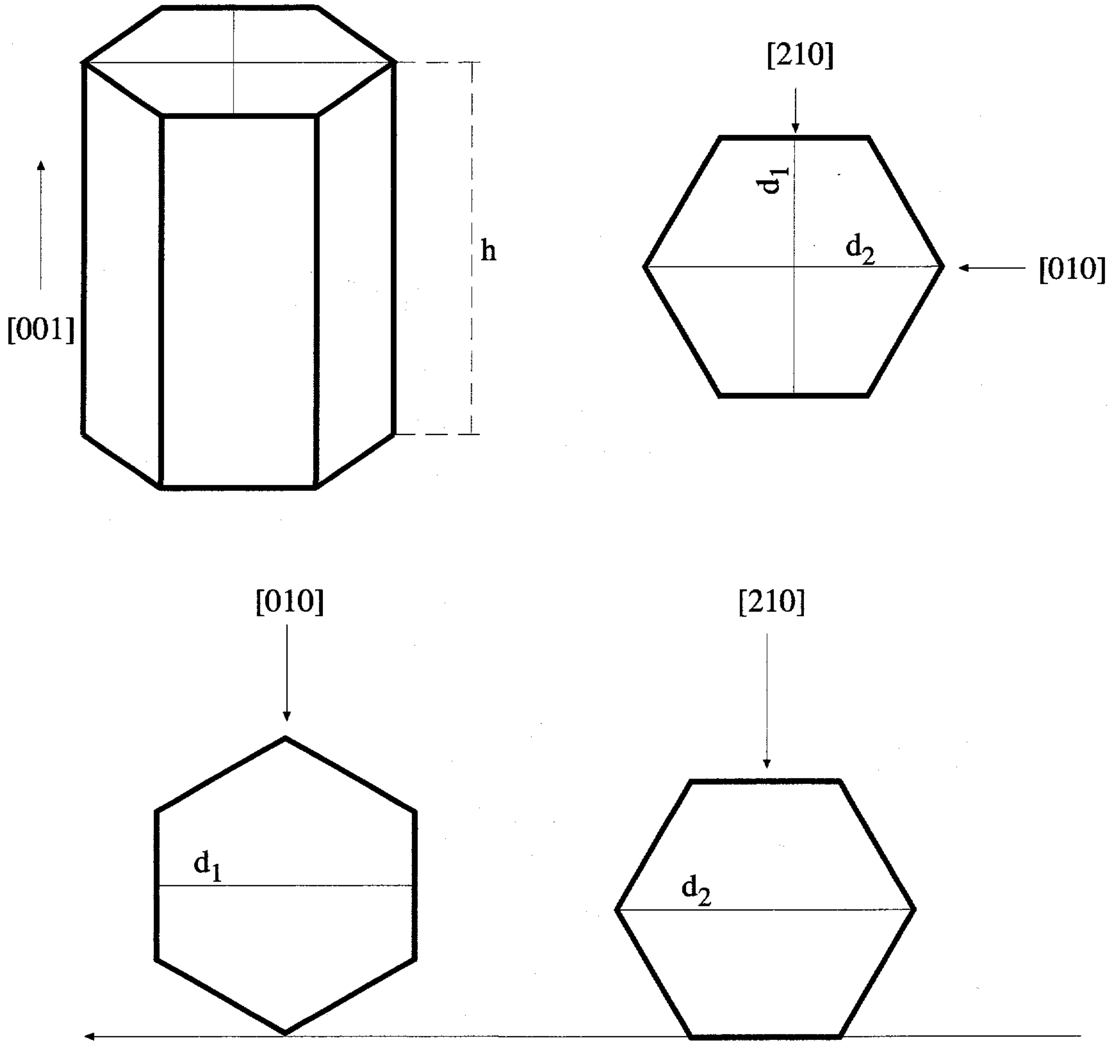

Figure 2.16: Projections of Hexagonal Crystallites

A simplified representation of a wurtzite crystallite is a hexagonal prism. The [001] axis is parallel to h, the height of the prism. The directions of the [010] and [110] axes are indicated. The aspect ratio is h/d where d can take on one of two values depending on the projection.

In [010] projection the measured diameter is d_1.

In [210] projection the measured diameter is d_2.

The ratio $d_2/d_1 = 1.15$ for a perfect hexagon.

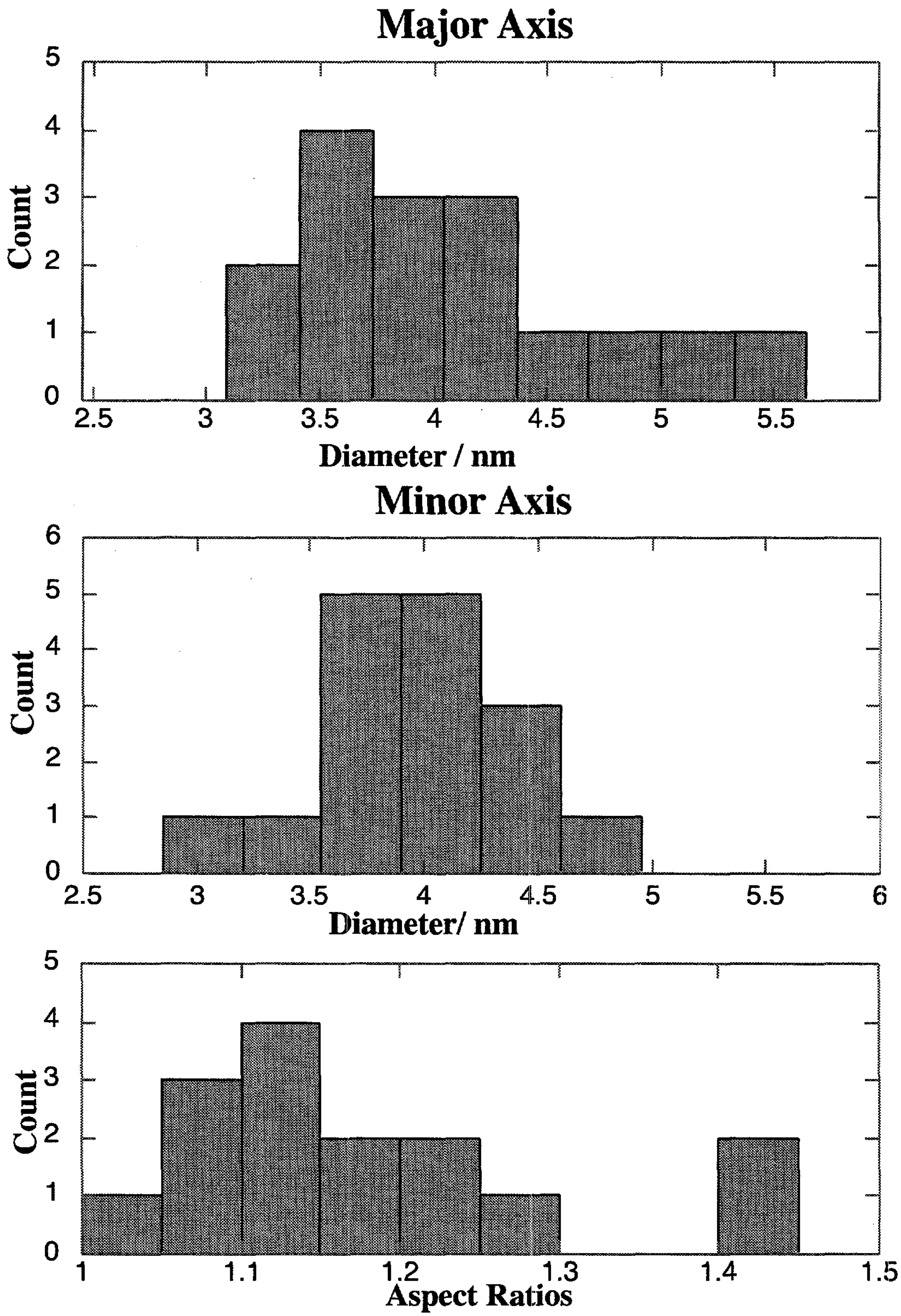

Figure 2.17: Sizing Data from HRTEM

Size data from 16 nanocrystals, obtained from HRTEM measurements. Same sample as in Figure 2.8. Binned using 002 spacings for major axis and 100 spacings for minor axis. Aspect ratio in units of nm/nm.

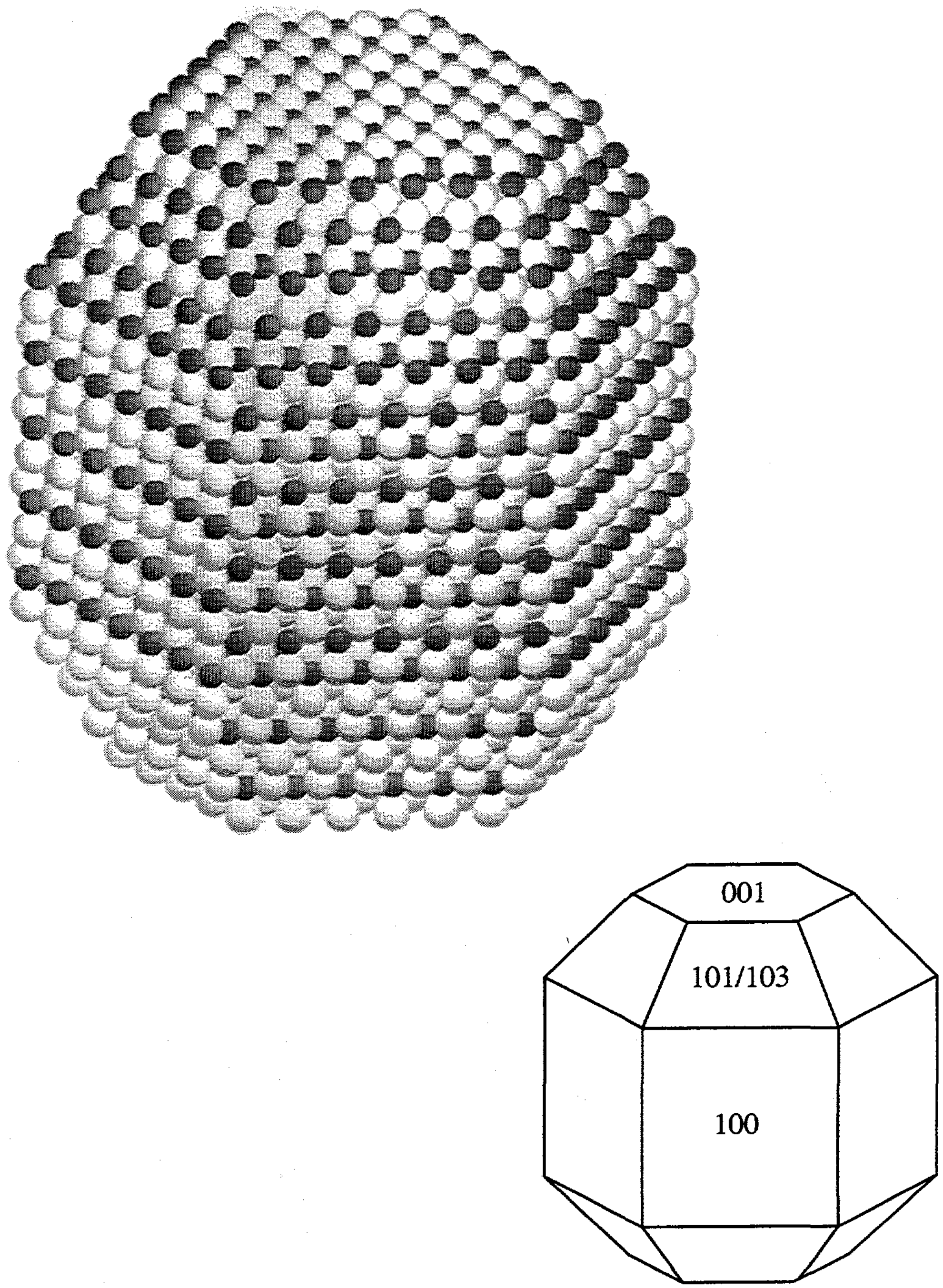

Figure 2.18: Model of CdSe Nanocrystal

Model of a CdSe nanocrystal structure. White atoms are Se, dark atoms Cd. The wireframe indicates the relevant surfaces. The model uses (101) surfaces to connect the (001) and (100) facets, but the actual structure is stepped, consisting of (101) and (103) surfaces.

Figure 2.19: Faceted CdSe nanocrystals

A sampling of all oriented nanocrystals from a single negative, average diameter 6.5 nm.

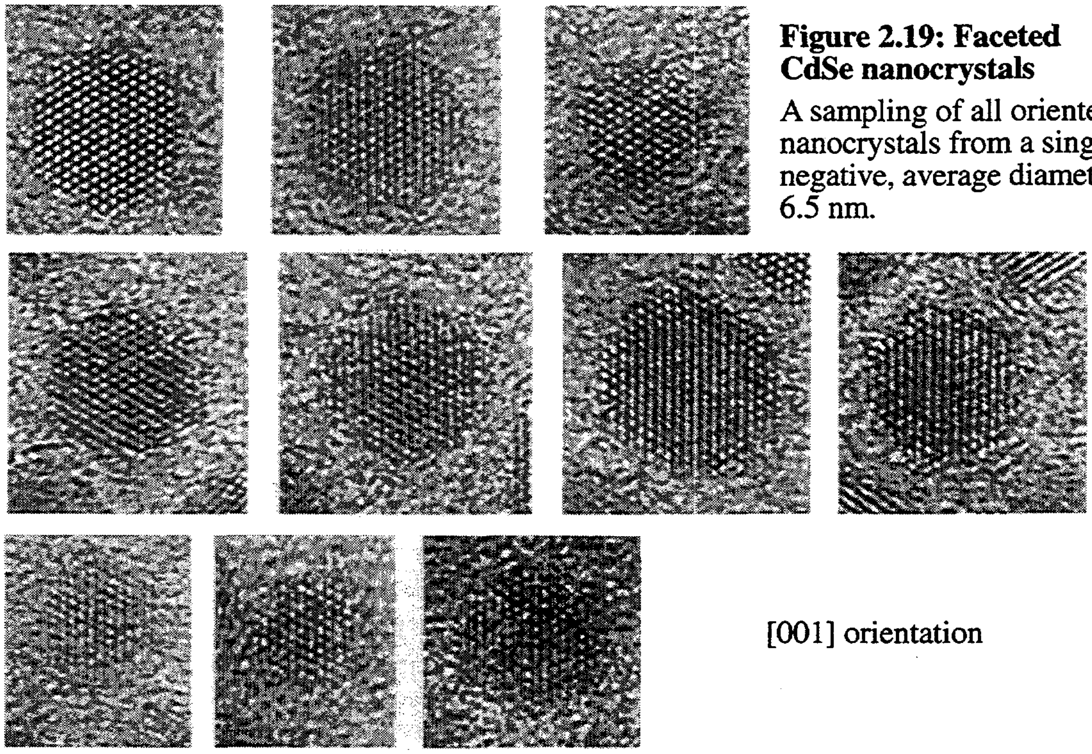

[001] orientation

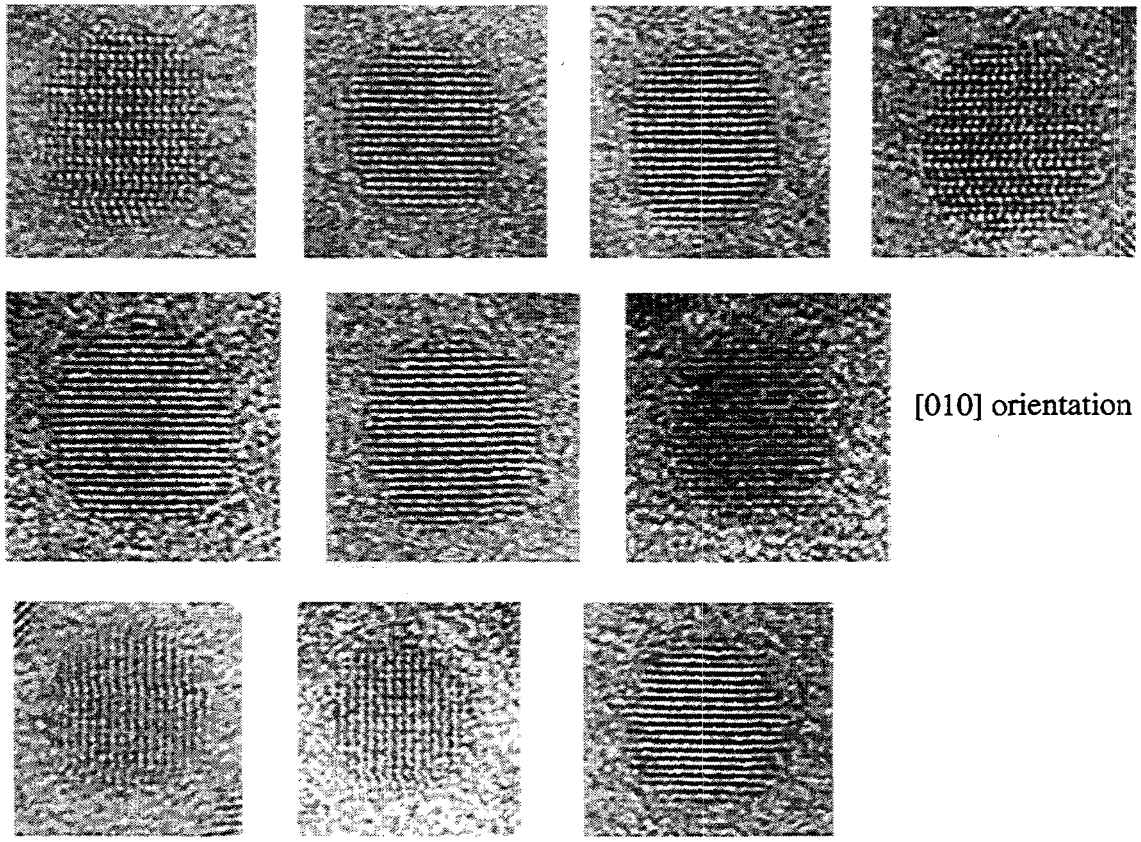

[010] orientation

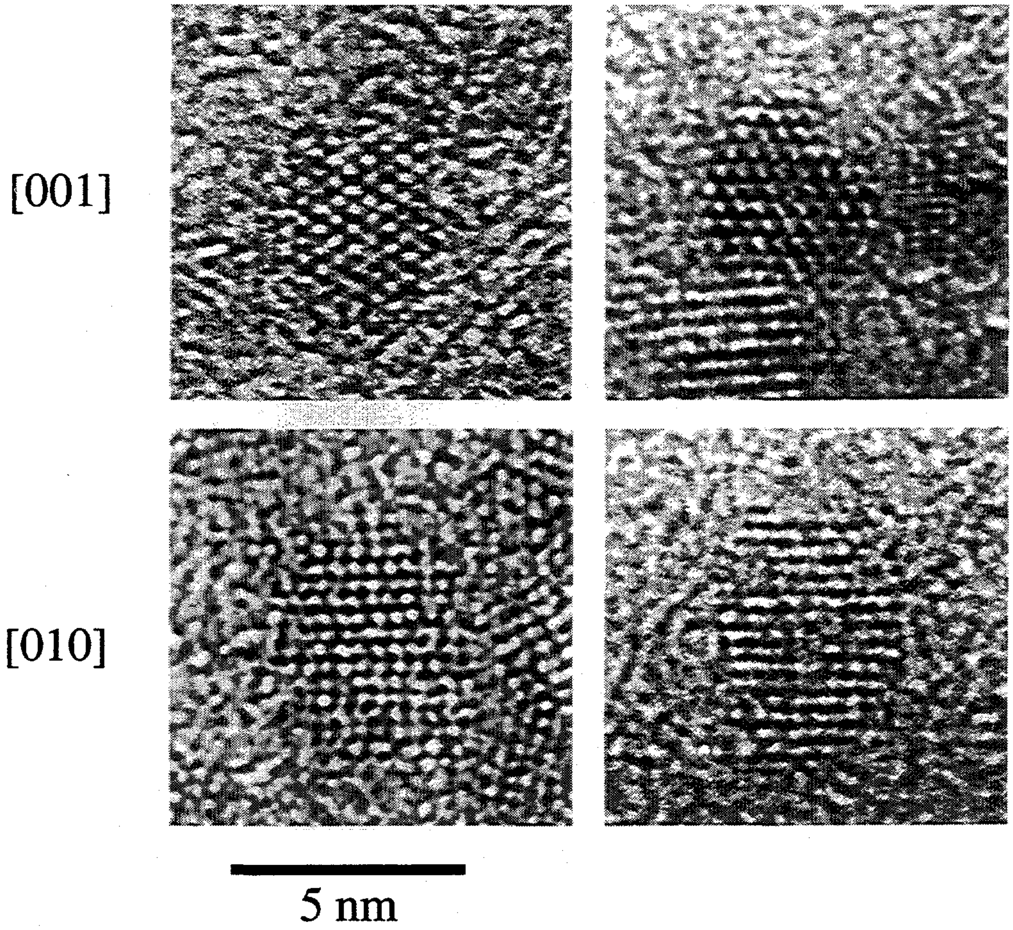

Figure 2.20 : Faceted CdSe Nanocrystals
Nanocrystals from sample AKL-74D, showing {001} and {100} facets. Average diameter (from CDF) 4 nm.

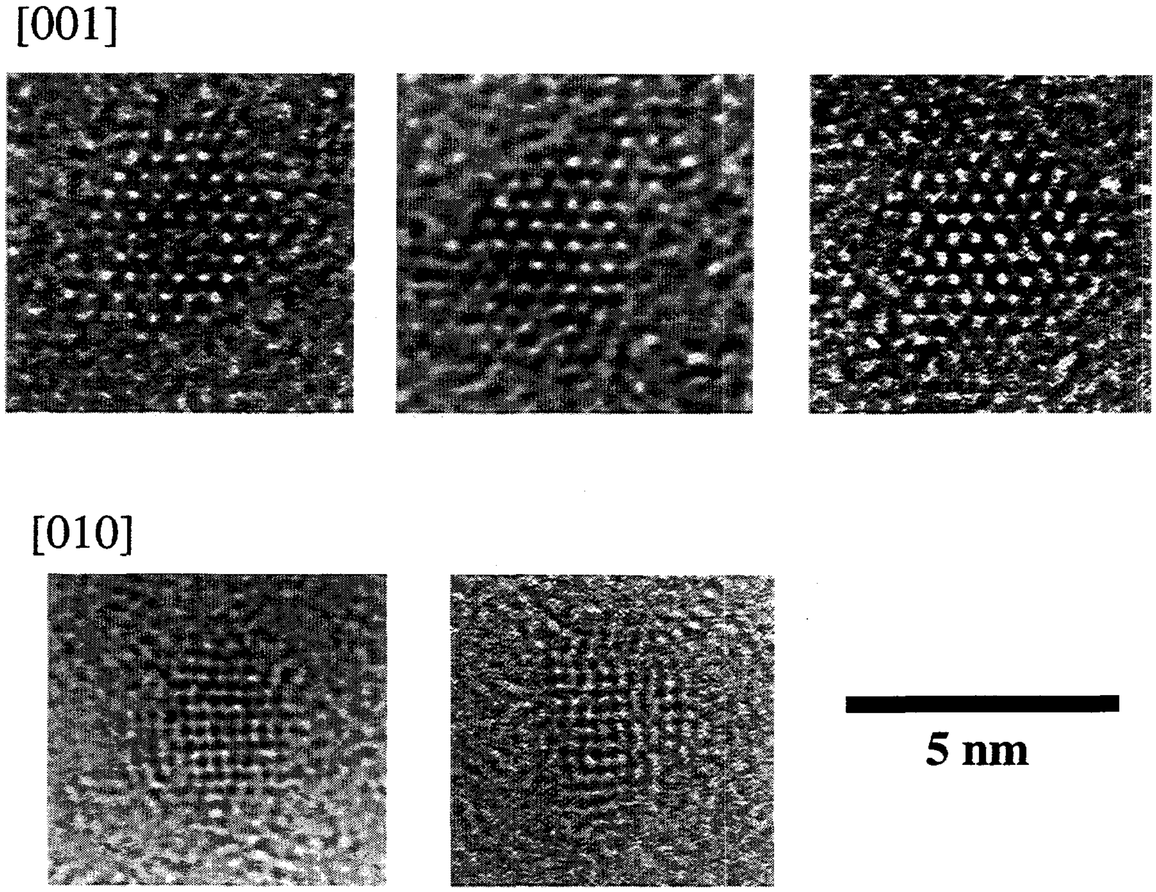

Figure 2.21: Faceted CdSe Nanocrystals
Nanocrystals from sample FL38, showing {001} and {100} facets. Average diameter 3.2 nm.

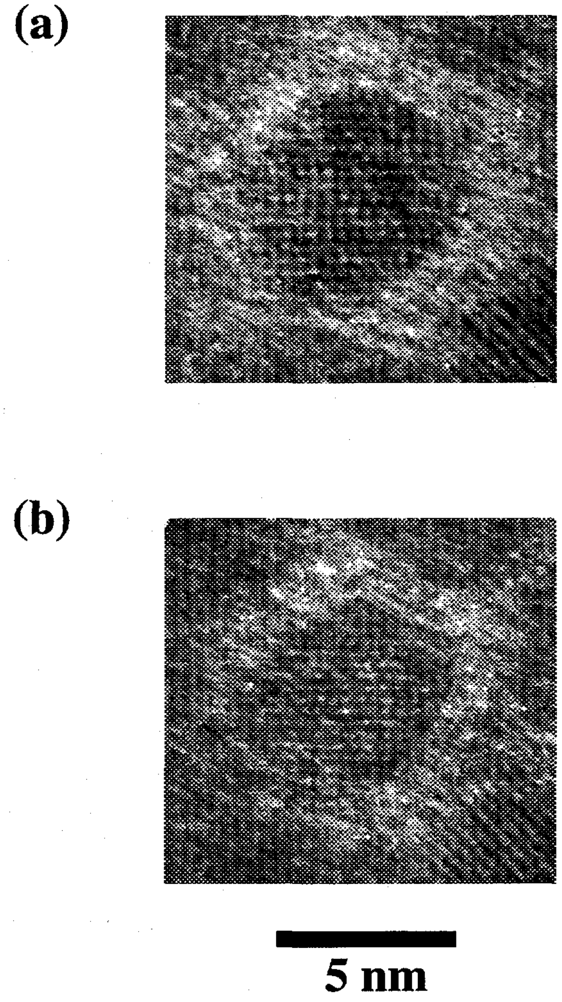

Figure 2.22: High Temperature Reconstruction of a CdSe Nanocrystal
Two views of the same nanocrystal in [010] projection.

(a) At 540°C the normal {001} and {100} facets are discernible.

(b) Ten minutes later at 560°C the top has refaceted along {103} surfaces. The side facets have been destroyed by this reconstruction. The bottom surface has not changed.

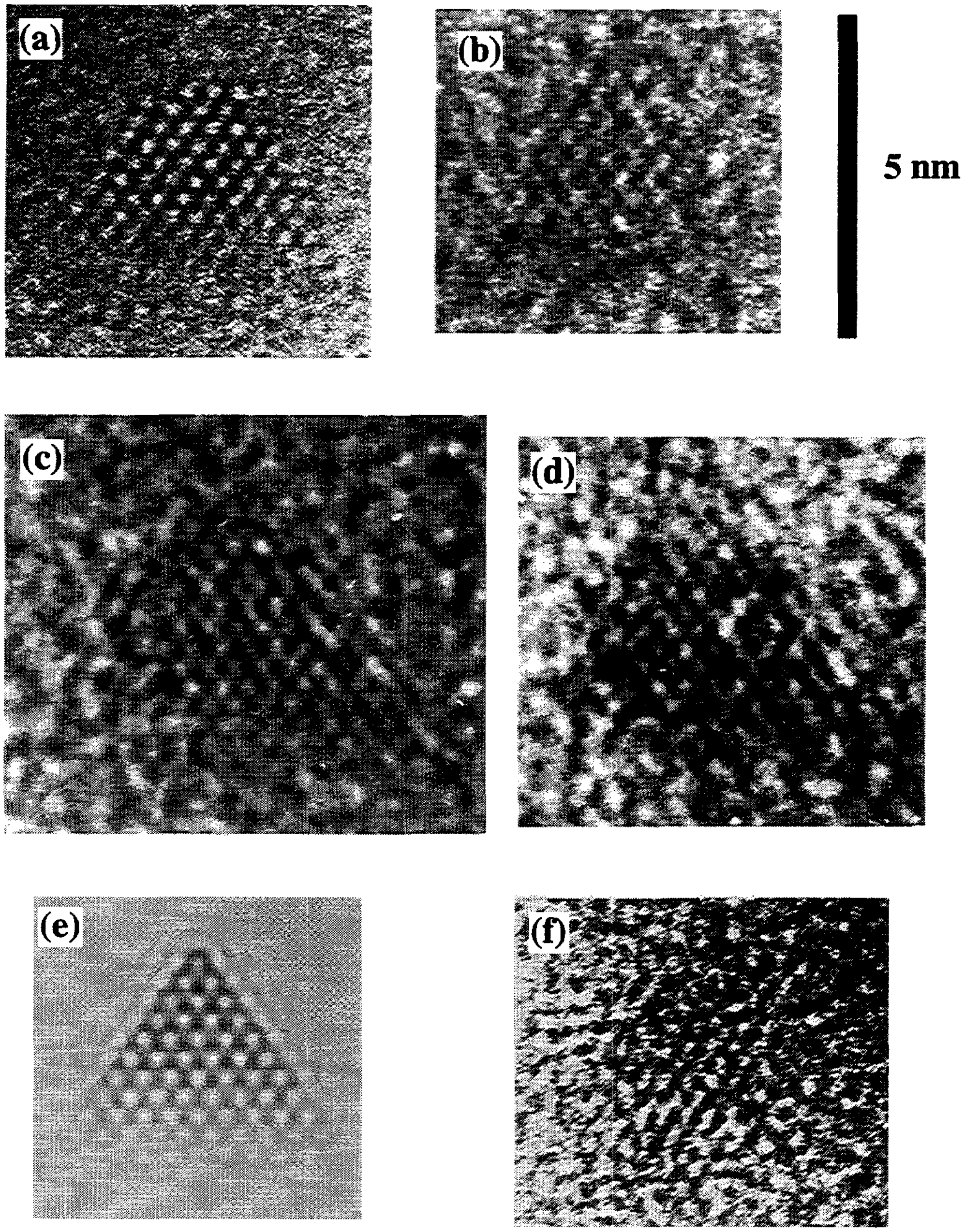

Figure 2.23: CdS Nanocrystals

HRTEM Micrographs of zincblende CdS nanocrystals in [110] projection.

(a)-(d) Triangular shapes, indicative of a tetrahedral structure. With the best quality images such as in (a) the loss of contrast in going from the apex to the base is readilydiscernible.

(e) HRTEM simulation of a Cd-(111) terminated tetrahedron in [110] projection.

(f) Rhombic shape observed in some images, indicative of a truncated octahedron structure.

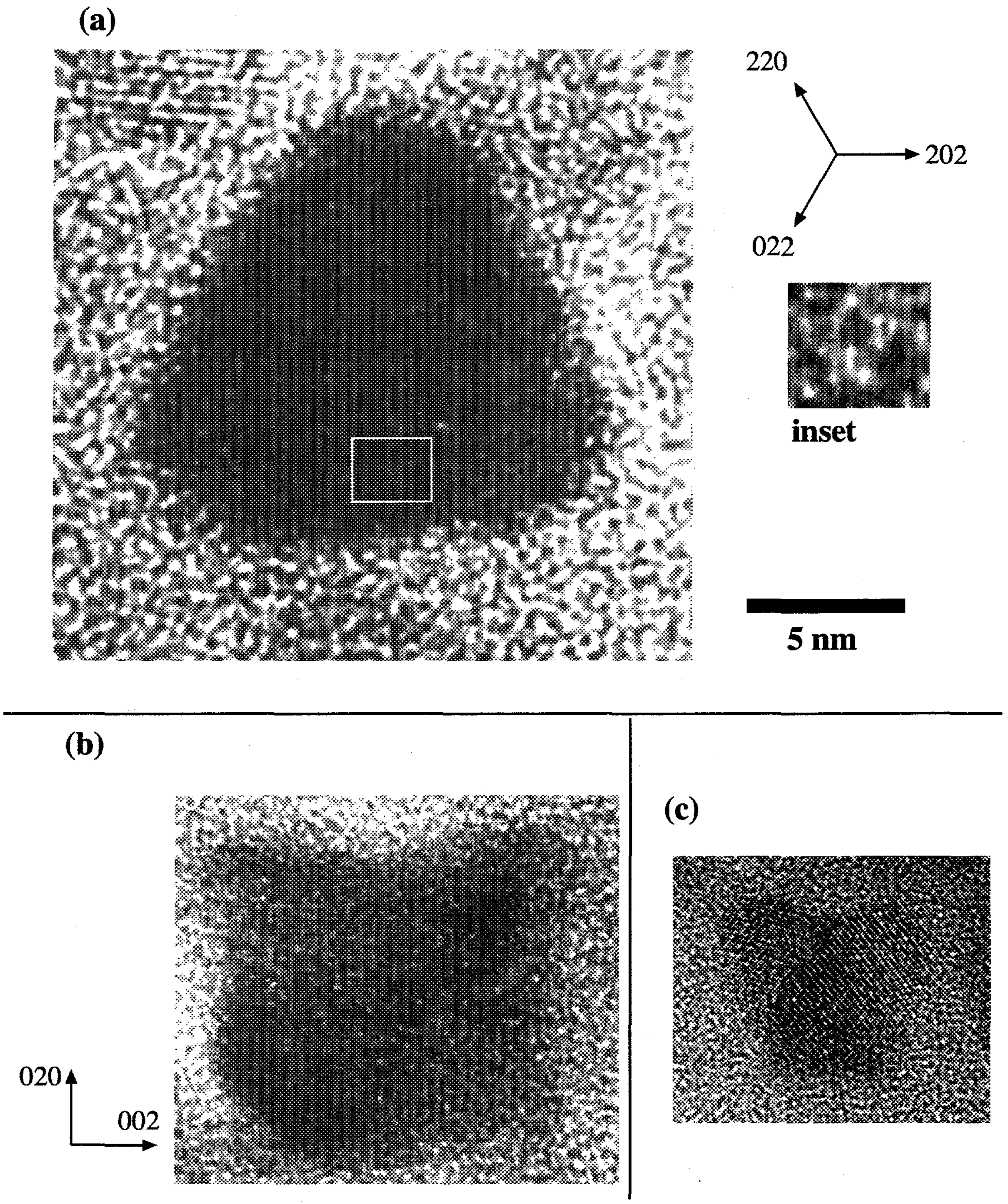

Figure 2.24: Large Tetrahedral CdS Nanocrystals

(a) CdS nanocrystal in [111] projection. 220 lattice fringes are visible in the enlarged inset.

(b) CdS nanocrystal in [100] projection. 200 lattice fringes are visible.

(c) CdS nanocrystal in the familiar [110] projection. Rotation twin faults have caused growth of the protuberances seen at the tetrahedral surfaces.

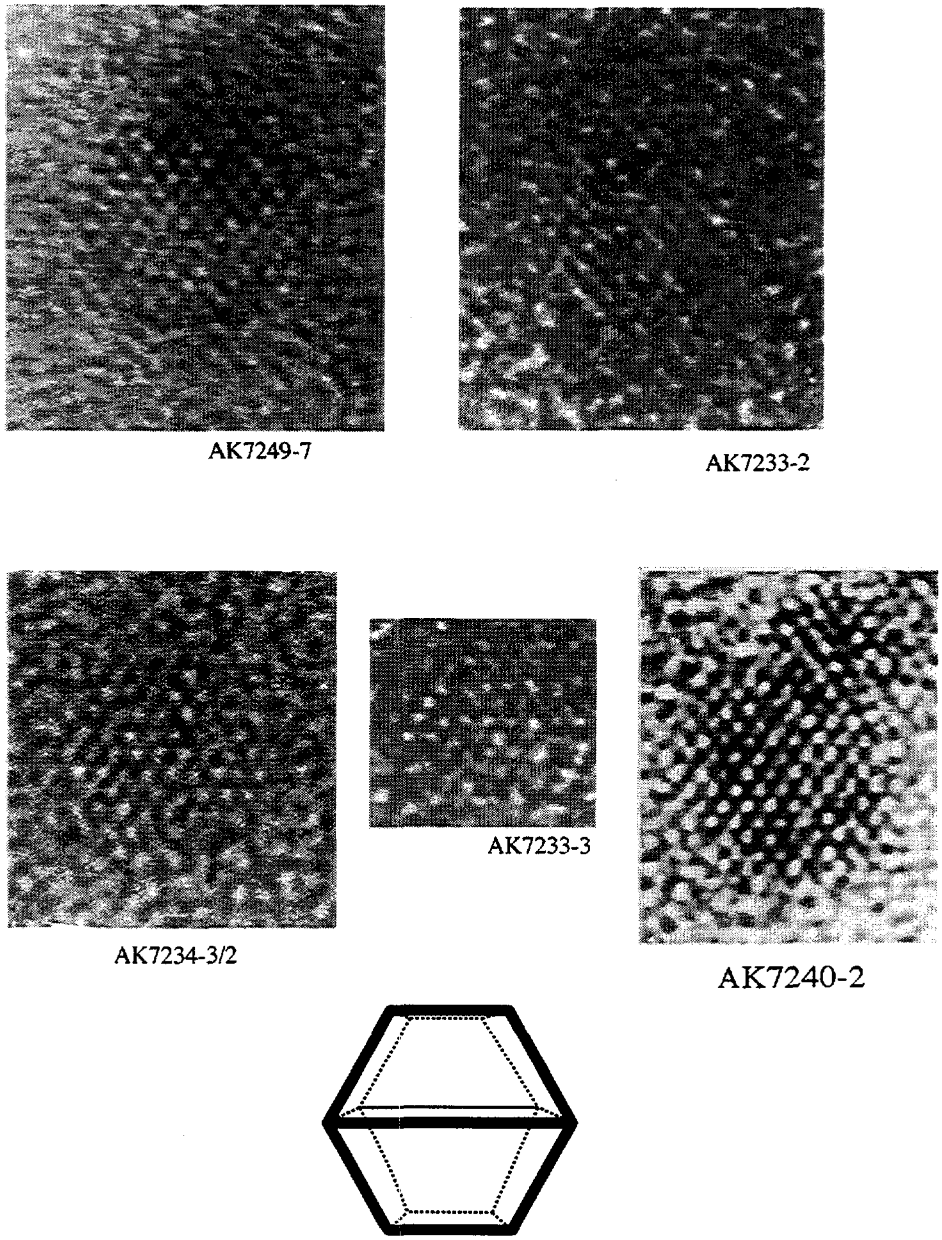
AK7249-7

AK7233-2

AK7234-3/2

AK7233-3

AK7240-2

Figure 2.25: InP Nanocrystals, Octahedral Shape
InP Nanocrystals in [110] projection, and model of truncated octahedron structure (see Fig. 2.28).

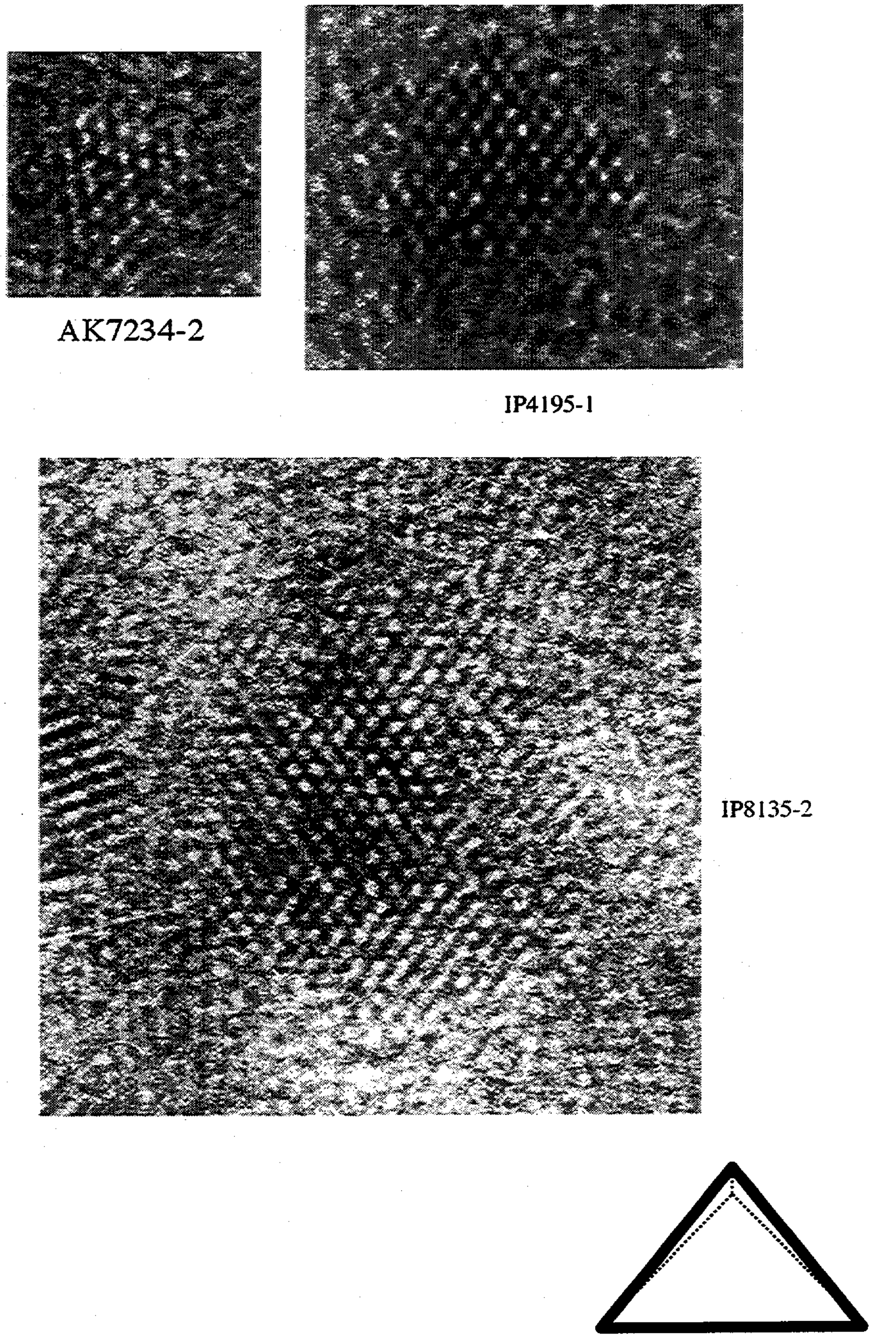

Figure 2.26: InP Nanocrystals, Tetrahedral Shape
InP Nanocrystals in [110] projection, and model of tetrahedral structure.

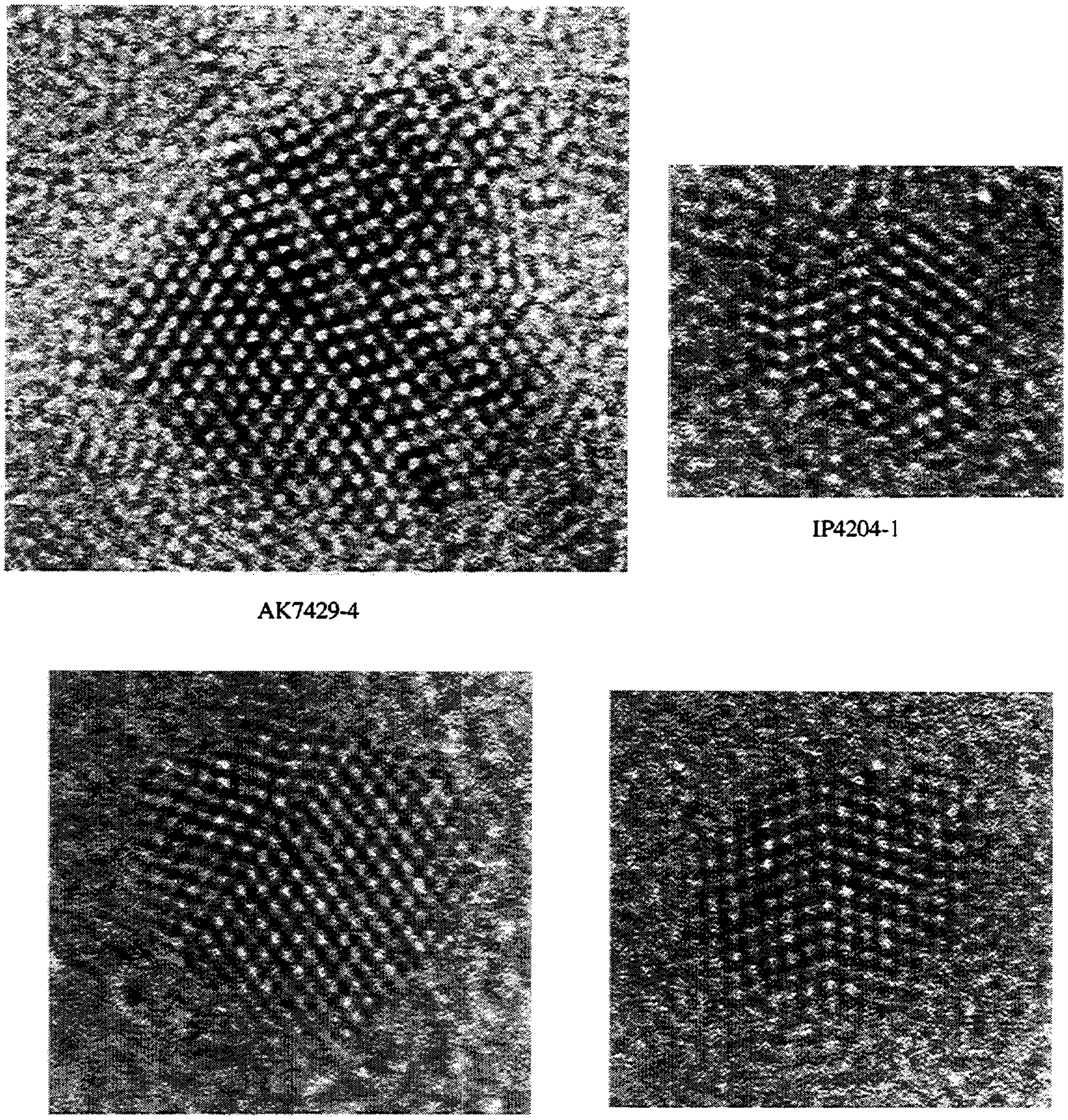

IP4204-1

AK7429-4

IP4189-1

IP4201-1

Figure 2.27: InP Nanocrystals, Defect Shapes

InP Nanocrystals in [110] projection.

Rotation twin faults change the symmetry and overall morphology, but the octahedral/tetrahedral motifs are still present

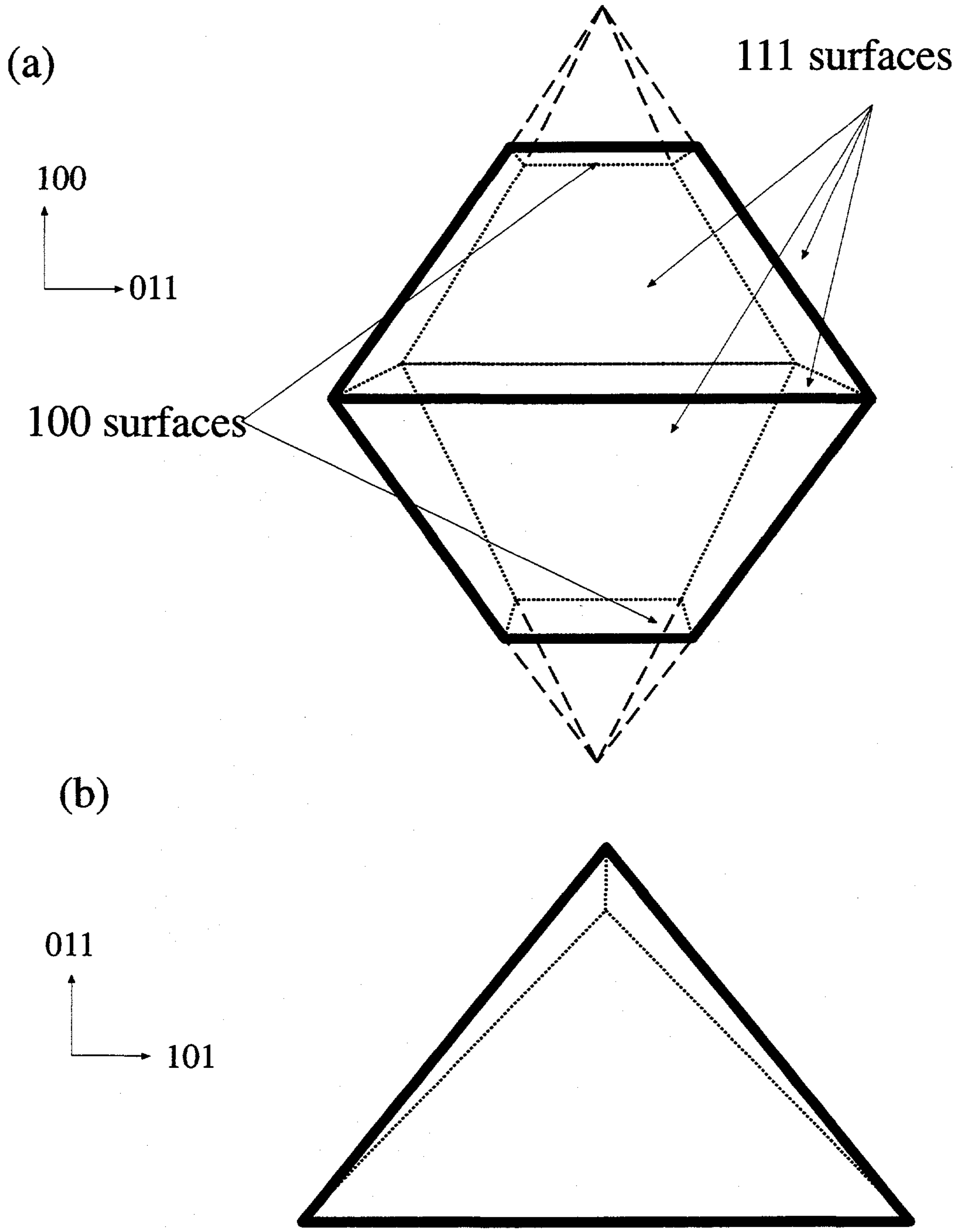

Figure 2.28: Models for InP Morphology

Perspective wireframe models for the (a) truncated octahedral and (b) tetrahedral shape in [110] projection. The thick lines indicate the outline that is projected.

The dashed lines in (a) indicate the truncated portion of the octahedron.

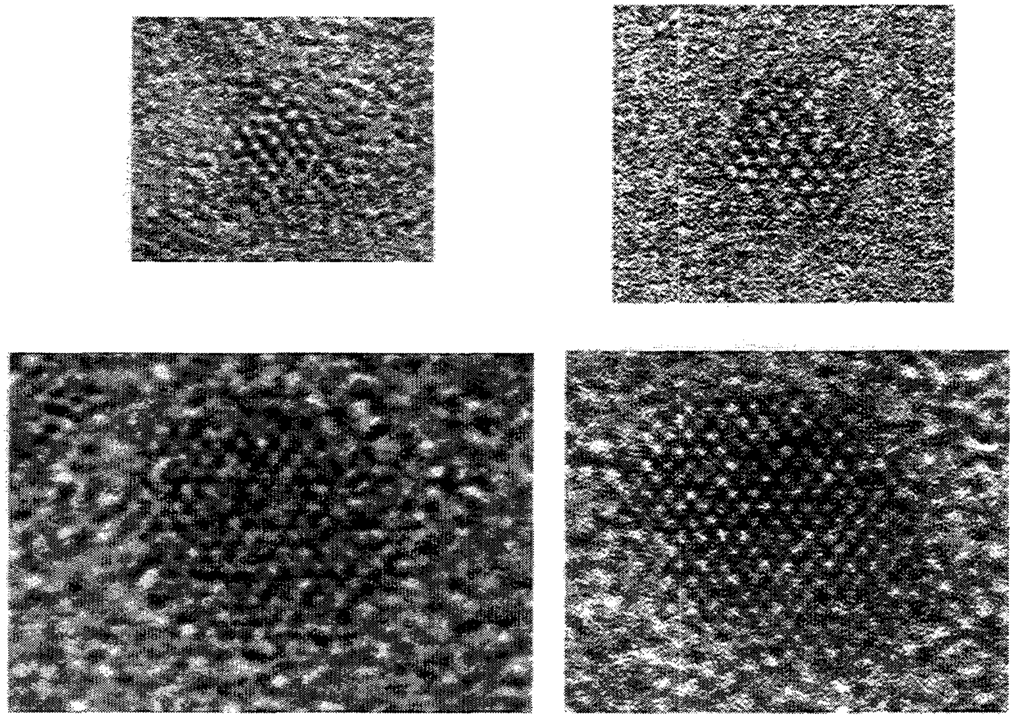

Figure 2.29: InAs Nanocrystals

InAs nanocrystals in [110] projection. {111} and {100} facets predominate similar to the case for InP.

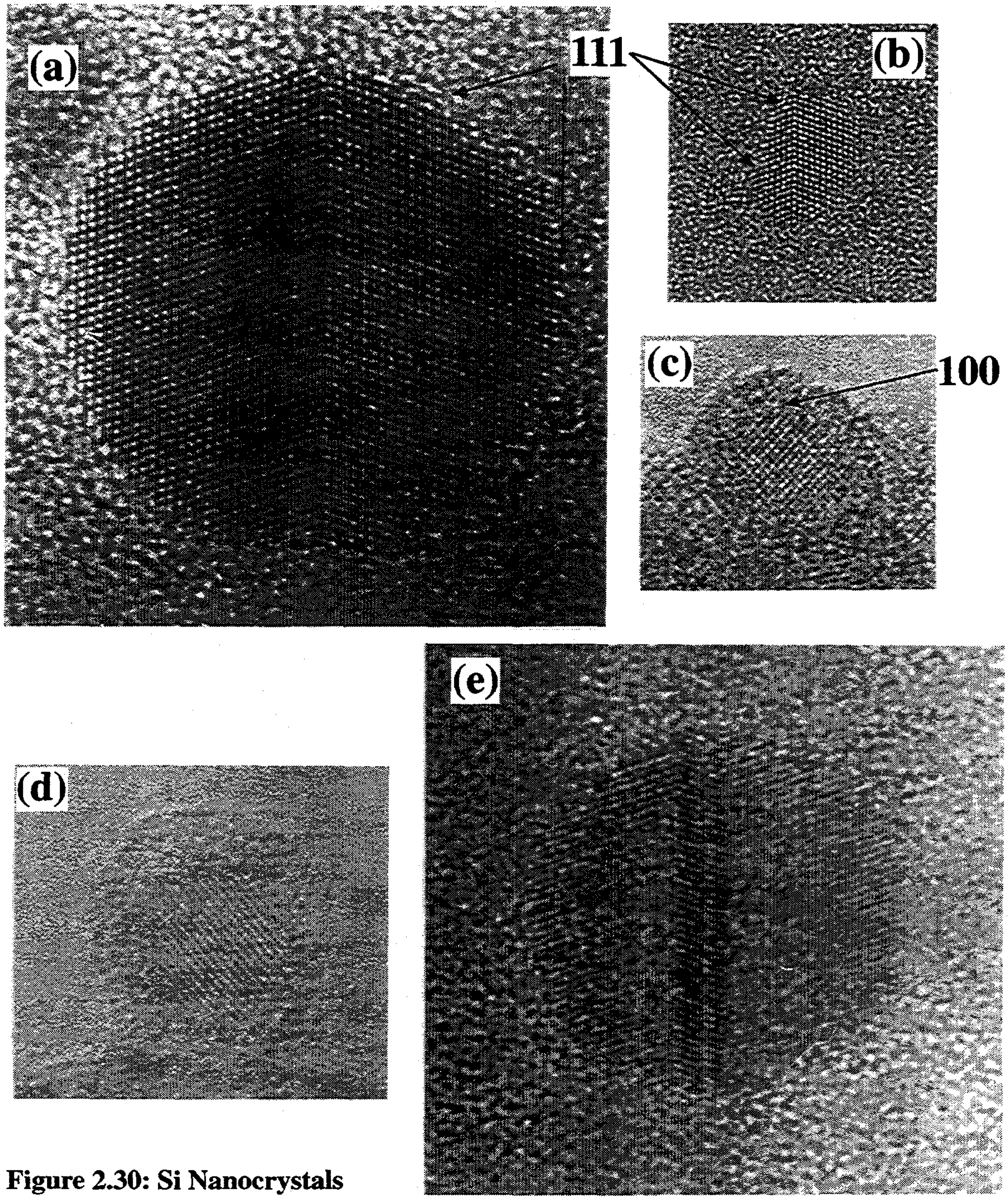

Figure 2.30: Si Nanocrystals

(a) Quasispherical nanocrystal with a single twin plane running through the center. [110] projection.

(b) Smaller nanocrystal, strongly faceted. [110] projection.

(c) Small nanocrystal showing evidence of (100) facet. [110] projection.

(d) Nanocrystal hanging over the edge of a hole in the amorphous holey carbon substrate. An amorphous shell is visible. By comparison to the 111 fringes visible in the core, the shell thickness is estimated to be roughly 2 nm.

(e) Nanocrystal with two parallel twin planes forming a twin band. Overall the morphology remains quasispherical. [110] projection.

Appendix 2-A: Identifying Common Semiconductor Crystal Structures And Orientations In HRTEM Images

In the following pages I have presented image simulations for CdSe nanocrystals in [001] and [010] projection and CdS nanocrystals in [110] projection. This is only for demonstration, and is not meant to be a rigorous analysis of the experimental images. It is included solely to allow the reader unfamiliar with the subject to approach the data presented in this document.

The dark areas correspond to atomic positions, but individual atom columns are not resolved. The images are near (but not necessarily at) Scherzer focus. The focus settings actually used were chosen to give the most resemblance to the experimental images, which may deviate significantly (~30nm) from Scherzer focus because of the thickness/scattering power of the nanocrystals. The image simulation for CdSe uses the model of Figure 2.18. The CdS simulation is based on the model in Figure 3.1. Detailed intensity distributions will depend on the chemical nature of the scattering atoms and the lattice parameters, but the general features (location of channels, orientation of facets, etc.) are relevant to all wurtzite and zincblende crystals respectively.

Lattice vector directions have been indicated for each simulation matched to the orientation of the simulated image. Relevant lattice spacings (d_{hkl}) have been marked on the simulated images. Similarly, lattice plane orientations are indicated. The orientation of {110}[1] planes has been indicated for the wurtzite [001] model even though they are not part of the model and are not expected to occur in these nanocrystals. This is merely for reference since the {110} family of planes constitutes one set of the bulk cleavage planes.

The features of the zincblende simulation are also applicable to diamond lattice

---

[1] These are the $\{11\bar{2}0\}$ in Miller-Bravais notation.

structures (i.e. Si, Ge).

Wurtzite [001]

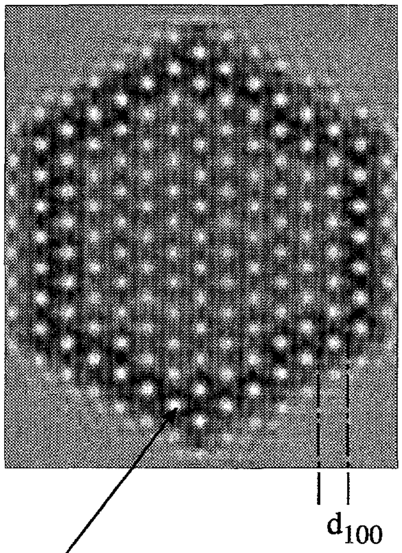

Channels in the crystal structure

Lattice Vectors

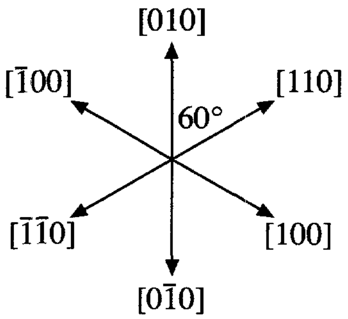

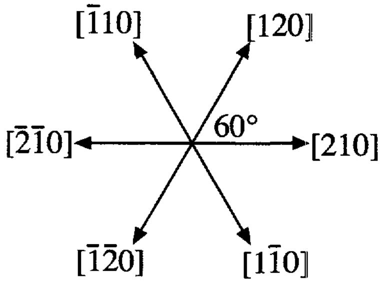

Lattice Planes

{100} planes

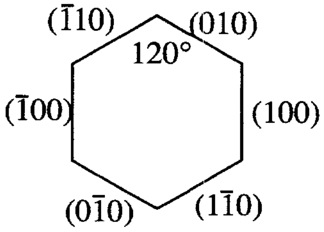

{110} planes

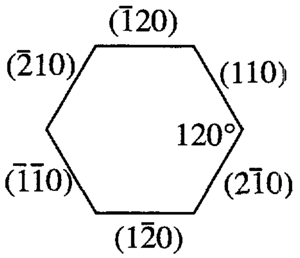

Wurtzite [010]

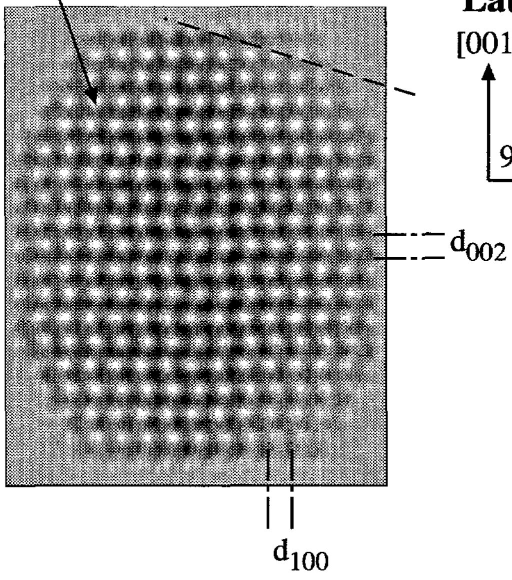

Lattice Vectors

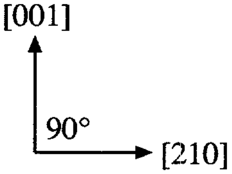

In this projection, the [100] vector is parallel to [210] but inclined to the plane of the paper 30°. The [010] vector points into the plane.

Lattice Planes

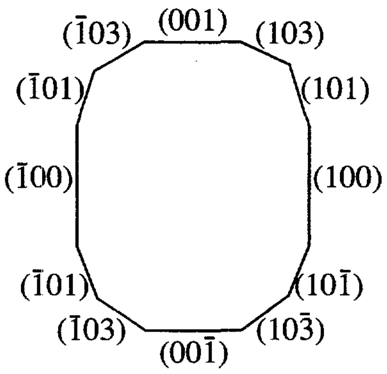

This simulation only has {100}, {101} and {001} facets. The crystal habit of {103} type facets is indicated by the dashed line.

Zincblende [110]

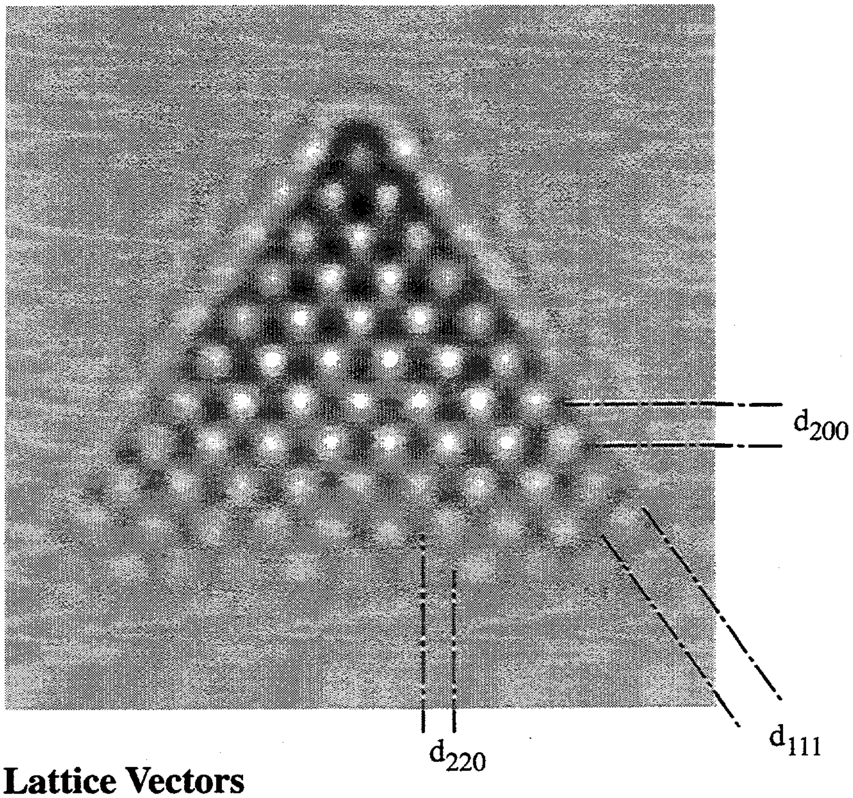

Lattice Vectors

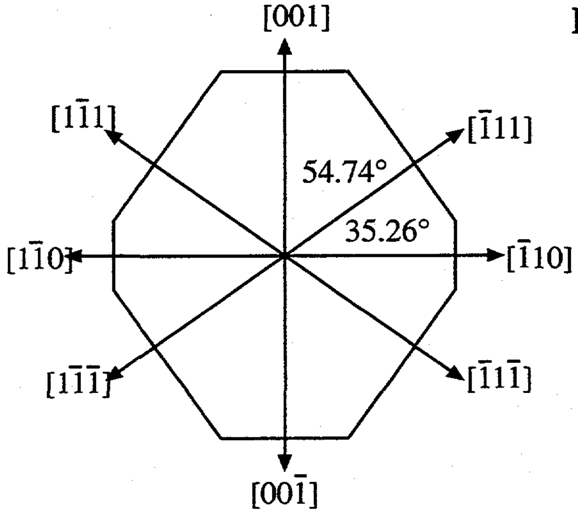

Lattice Planes

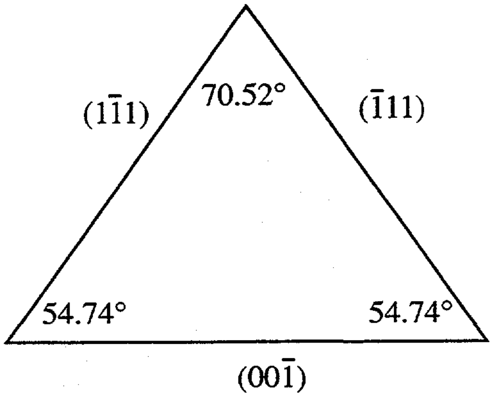

For cubic structures, each plane index is the same as the lattice vector perpendicular to it: [hkl] is normal to the plane (hkl)

Chapter 3: Epitaxial Nanocrystals

Amazement is the first step to a discovery.

—*Louis Pasteur*

3.1 Introduction

Both the chemical behavior and the electronic properties of nanocrystals are deeply affected by their surfaces. Consequently controlling the surfaces is of paramount concern in the development of nanocrystal syntheses. The task of controlling surfaces involves several distinct considerations. They are electronic passivation, chemical passivation, and chemical manipulation.

Electronic passivation refers to the process of removing undesirable electronic states from the nanocrystal surface, be they dangling bond states, impurities (such as oxygen) or any other trap site. An electronic passivant must remove all these states and introduce a barrier at the surface. Hence the passivant itself must have a higher band gap (or HOMO-LUMO gap) than the nanocrystal.

Chemical passivation protects nanocrystals from undesired reactions, such as coagulation, oxidation, or decomposition. Since most of these reactions involve surface electronic states, electronic and chemical passivation generally go hand in hand. Additionally, the chemical passivant must be stable towards replacement with undesirable compounds.

Finally the concept of chemical manipulation is a very important one, as it is the main feature distinguishing colloidal nanocrystals from other types of quantum dots (QD's), such as those grown by MBE or ion implantation. Unlike the latter, nanocrystals behave chemically as large molecules. They are soluble in common solvents (water, toluene, pyridine, etc.) which facilitates processing and further chemical manipulation. They can be arranged into higher order structures by chemical means, forming self-assembled monolayers (SAM's) [70], superlattices [71], and molecularly linked nanocrystal assemblages [35]. They can be treated as components in other processes to form polymer blends, thin films [72], even functional LED's [73]. Verily, this chemical manipulability is at the heart of what makes nanocrystals interesting. Regrettably, manipulability frequently requires that the surface be modified, which conflicts with the requirement for chemical passivation that the surface remain stable.

Generally, all three requirements of surface control have been met using a single chemical species, the capping ligand. This is the organic molecule that binds to the nanocrystal's surface during synthesis. For example, in the case of CdSe nanocrystals, TOPO electronically passivates the surface by saturating dangling bonds. It chemically passivates the surface as well, acting as a barrier to other molecules that may react with the crystallite. Additionally, the alkyl chains in TOPO confer solubility in organic solvents due to their ability to mix with solvent molecules.

Lamentably, TOPO does a fairly poor job at each of its tasks. As discussed in Section 2.2, the steric problems in coordinating to the nanocrystal surface leave dangling bonds, which act as electronic trap sites and easily oxidize. Other than solubility, TOPO does very little towards chemical manipulation, so it often needs to be replaced with other molecules for this purpose. Fortunately the TOPO-nanocrystal bond is rather labile, so this can be accomplished fairly easily. Of course, this also makes the nanocrystal vulnerable to chemical attack by undesirable species. It is perhaps too much to expect that a single molecule can fulfill all the discordant requirements of control of the nanocrystal surface. The logical conclusion then is to separate these functionalities into separate compounds.

One way to accomplish this is demonstrated by the Si nanocrystals in section 2.6. The oxide shell surrounding these particles is an excellent passivant as demonstrated by the stability of those nanocrystals. In general one may expect good passivation from an inorganic overcoat as the high density of atoms at the interface helps to passivate the maximum number of dangling bonds. Consequently there has been significant interest in the synthesis of inorganically passivated nanocrystals. [74, 75] In the ideal case, the passivating coat is achieved with a lattice matched epitaxial overlayer. This ensures that all surface dangling bonds are passivated and minimizes the effects of strain on the electronic properties of the nanocrystals.

3.2 CdS/HgS/CdS Quantum Onions

The first epitaxial system in a nanocrystal was the Quantum-Dot-inside-a-Quantum-Well (QDQW) system of Mews. [47, 76] This is built up from a CdS nanocrystal core, surrounded by 1-3 layers of HgS, capped off by another 1-5 layers of CdS. Polyphosphate ligands on the surface provide solubility. Due to the onion-like shell structure, these nanocrystals are better known as quantum onions.

3.2.1 Morphology

The structural features of this system are closely tied to the synthesis conditions, hence it is instructive to examine this process and look at the various intermediate stages. To begin with, as shown in section 2.3 the CdS core is in the zincblende structure, rather than the more thermodynamically wurtzite structure. This is a consequence of making these nanocrystals at room temperature. Similarly, the tetrahedral shape of the cores is dictated by the use of anionic polyphosphate ligands as surface passivants. Finally it should be reiterated that only 75% of the crystallites observed had this tetrahedral shape. The other 25% had truncated octahedral shapes similar to those of III-V nanocrystals, or, more commonly, were severely faulted. TEM images of tetrahedral CdS particles and defect structures are shown in Figure 3.1, together with a model structure for the tetrahedral crystallite. It should also be noted that the statistics above are based on a total of 14 identifiable images (only images with cross-fringes were counted), so the statistics are not very good. Part of the problem here is that the hydrophilic nature of these particles makes it difficult to prepare good specimens with a lot of particles on the grid.

The main morphology is preserved during the growth of the HgS layer, which is accomplished by precipitating Hg^{2+} ions onto the nanocrystal core. This can be done by addition of mercury ions to the solution because HgS has a lower solubility than CdS.[1] As has been shown, this actually results in exchange of the surface cadmium ions of the CdS crystallites with the mercury ions in solution [47], which further supports the notion that the surfaces are cadmium terminated. Within the statistical error, the mean size and size distribution is unchanged, which is expected if the HgS layer is grown by substitution, rather than overgrowth. Epitaxial layer growth is virtually assured in this step if the mercury ions substitute for surface cadmium atoms. However, defect structures become more prominent and only 64% of the particles have tetrahedral shape. 23 particle images were counted for this sample. Sample TEM images and a model are shown in Figure 3.2.

The final coating of these particles is carried out by adding excess cadmium ions to the solution and growing CdS on top of the HgS layer via slow H_2S injection. This reaction takes place at pH 5.5, where the chemical equilibria are such that nucleation of new CdS particles is suppressed. Sample TEM data is shown in Figure 3.3. The average size increases in this step, as expected. 63% of the resulting nanocrystals show tetrahedral features, based on counting 58 nanocrystals. However, half of these tetrahedral nanocrystals actually had rotation twin faults similar to the particle in Figure 3.3 (b), where a tetrahedral core remains discernible, but an outer layer has grown mismatched to the core. They are not truly tetrahedral, but do retain vestiges of their tetrahedral origin, so they were included with them. Furthermore, the particles remained fully crystalline throughout. There is no evidence of an amorphous phase within the crystallites and the twin fault creates no dangling bonds at the interface.

The size evolution is summarized in the histograms of Figure 3.4. To obtain these

---

[1] The K_{sp}'s differ by roughly 10 orders of magnitude.

data, all {111}-fringed crystallites were counted regardless of whether or not they had discernible shape. Using a different sample it was determined that the statistics do not change compared to counting only cross-fringed crystallites.

Optical Data [47, 76, 77] demonstrate the presence of a HgS phase in these nanocrystals. The TEM data above, especially the absence of any amorphous phase, shows that this phase is in fact composed of a crystalline epitaxial layer grown on the initial CdS core and that the final CdS shell also grows epitaxially. Further evidence for this comes from more detailed consideration of the structure seen in Figure 3.3 (b).

3.2.1.a Multiply-Twinned Tetrahedral Crystallites: Onions with Ears

To facilitate the study of the detailed morphology of multiply twinned crystallites we studied onion samples which had been dialyzed to remove excess ions from solution. This mostly gets rid of sodium ions bound to the polyphosphate ligands. Samples that have been treated in this way can be solubilized in methanol which makes it easier to prepare good TEM specimens. The drawback to this is that the dialysis process turns the sample solution acidic which promotes Oswald ripening. However, we have not found any significant morphological differences between images from these samples and the previous images.

Figure 3.5 shows several images of multiply twinned nanocrystals. The twin results in the outgrowths on the tetrahedral surfaces, which give the appearance of "Mickey Mouse ears" on the core. A model structure of the nanocrystal morphology giving rise to these images is shown in the same figure. This models, which is similar to the tetrapods observed by Kaito et. al. [18], consists of a tetrahedral Cd-{111} terminated tetrahedron, surrounded by a single layer of HgS, which leads to Hg-{111} termination for this core. At the interface between this core to the outer layer is a rotation twin fault. This arises by introducing one layer of hexagonal (wurtzite) stacking into an otherwise cubic (zincblende) structure and does not lead to a loss of passivation, as no bonds are broken. However, it does make the cap layers on adjacent faces crystallographically mismatched so that they cannot grow into each other. Instead they form lobes on the tetrahedral surfaces which appear as the "ears" in projection. We have made the outer shell three layers thick in our model because of computational limitations.

We assume for this model that the fault occurs in the outer CdS layer. However, our TEM images do not give information as to the exact location of the fault. It may also be the HgS layer that is faulted. Indeed, it has been suggested that HgS is more stable in the wurtzite form than in the zincblende form. [56] However, the room temperature stable form of HgS is actually cinnabar and we are not aware of any experiments indicating the existence of wurtzite phase HgS, whereas data does exist for the zincblende form. [78-81] CdS on the other hand is well known for its polytypism, so we have chosen to represent the fault as being in the CdS layer. Kinetic factors may also play a role though, so this is by no means definitive. The TEM data for CdS/HgS nanocrystals should indicate if the fault occurs in the HgS layer, but the quality of the images is woefully inadequate for making this determination.

Close inspection of the micrographs in Figure 3.5 shows a line of enhanced contrast along the twin fault. This does not normally occur in HRTEM images of rotation twin faults. One way this contrast change can arise is from the difference in atomic scattering factors between cadmium and mercury. Since lattice images are interferograms of diffracted electrons with the direct beam, the contrast increases with increased amplitude scattered into a particular reflection. For zincblende 111 diffraction, the amplitude term in the structure factor is $f_{A^{2+}}^2 + f_{B^{2-}}^2$ where *A* denotes the cationic species (Cd or Hg) and *B* denotes the anion (S). Hence, for the same defocus and specimen thickness, lattice fringes arising from HgS {111} planes will be more intense than those from CdS {111}. In a sense, the {111} lattice fringes are "chemically sensitive." This is a very simplified explanation assuming a simple kinematical picture of scattering under two-beam conditions. Sample thickness and tilt, and other diffracted beams can affect the details of the images, so a full multibeam dynamical simulation is required to verify this.

Such a simulation is shown in Figure 3.6 (a) for the model nanocrystal and it clearly reproduces the contrast change at the interface. Figure 3.6 (b) displays a simulation for the same model structure but with all mercury atoms replaced by cadmium. This image shows no contrast change, as expected. The details of the contrast change are somewhat sensitive to defocus and tilt, so it is still difficult to determine the exact location of the HgS layer relative to the fault, using our data. Nevertheless, the contrast change does argue forcefully for the localization of the HgS at the interface. This is particularly striking if the simulation and experimental images are combined to form the images in (c). The simulated and real images are combined by a hard fade (about 4 lattice spacings wide) using a gradient mask in Adobe® Photoshop® 3.0.

It should be noted that the "eared" structure, while undesirable from the viewpoint of sample homogeneity, is actually fortuitous for the structural analysis. Since the outer CdS shell cannot be closed, the HgS layer becomes unobscured in [110] projection, which emphasizes the contrast change. This is best seen in a model in that projection, Figure 3.7. If the fault is absent, the outer CdS shell will completely enclose the core, forming a tetrahedral onion. In such a crystallite there are several layers of CdS above and below the projected HgS planes, which masks the contrast change.

3.2.2 Remarks

The microscopy data presented clearly shows the epitaxial nature of the CdS/HgS/CdS QDQW's. However many details remain unresolved. In particular, it is unclear what causes the fault at the interface between the HgS layer and the CdS shell. It is also unknown where exactly the fault occurs. If it occurs within the HgS layer, this would imply that the HgS layers on different tetrahedral faces are not connected. Given the leakage of the electron-hole wavefunctions [76] even in the ideal case, this may not affect the electronic level structure much. On the other hand, it also implies that the various HgS layers have different crystallographic orientations which may interrupt the band structure of the HgS shell. It may be more appropriate to think of such a system as four strongly coupled sheets of HgS, rather than a HgS shell. Albeit, such discussions are moot unless the various different types of crystallites can be separated from each other.

3.3 CdSe/CdS Core-Shell nanocrystals

The high temperature organic route lends itself equally well to shell growth. Since CdSe nanocrystals generally have poor photoluminescence quantum yields there is great desire to improve the nanocrystal surface passivation. Previous efforts using zinc chalcogenides were quite successful in achieving improved quantum yields but fell short of perfect passivation. [74, 75] To some degree this may be attributed to the poor lattice match of the zinc chalcogenides to the CdSe lattice. Our lab used CdS as the passivating agent instead and achieved quantum yields approaching 100% in some samples. [14] This bespeaks the excellent passivation achieved by this cap and already suggest that epitaxy is involved. The structural proof is presented below.

The synthesis is described in [14]. To summarize, these nanocrystals are prepared by shell growth on CdSe nanocrystals prepared by the route described in section 2.2. The TOPO ligands are replaced with pyridine by refluxing in pyridine solvent. These are the cores. The cores are then heated in pyridine and CdS feedstock is injected at 100°C to allow shell growth.

Representative micrographs of core and core/shell nanocrystals are presented in Figure 3.8. The images are of cores, cores with thin shells (~1 layer of CdS) and full core-shells respectively. The fringe contrast reveals that the nanocrystals are in the wurtzite crystal structure. Additionally, the nanocrystals are somewhat faceted, consistent with the previous observations on CdSe nanocrystals.

The average aspect ratio of the initial cores, $A = \frac{diameter \parallel c-axis}{diameter \parallel a-axis}$ was 1.03± 0.015 [1] and there was an average of 1.6±0.2 stacking faults (rotation twin faults) per nanocrystal. The nanocrystals remained fully crystalline and somewhat faceted upon shell growth. There was no evidence for any defects at the core/shell interface. Indeed, the main indication of shell growth was the change in the nanocrystal diameter. In addition *A* increased to 1.10±0.04, and the average stacking fault density increased to 2.2±0.2 upon shell growth.

All the observed stacking faults extended across the entire nanocrystal. This indicates that any stacking faults initially present in the core were preserved during shell growth and propagated through the shell, such as the example indicated by arrow 1 in Figure 3.8. The increase in the stacking fault density is attributable to additional stacking faults occurring in the final layers of the shell structure, arrow 2 in Figure 3.8.

Sizing statistics are shown in Figure 3.9 for cores (sample MS37) and core-shells (Se37-S13). As can be seen, the average size increases upon shell growth. The size distribution also broadens upon shell growth, which is consistent with the broadening observed in the optical spectra. [14] Based on the change in average size, the mean shell thickness is estimated to be three layers or about 1 nm. Thin shell particles were not stable in the microscope and quickly degraded, making it impossible to collect enough data for statistics. For these particles the shell thickness was estimated from the amount of reagent consumed and the average surface area of a core calculated from the average radius. The beam sensitivity of the thin shell samples may be due to incomplete closure

---

[1] Note, the diameter perpendicular to c measured in the HRTEM is not parallel to *a*. To obtain the diameter parallel to *a*, multiply by $\frac{2}{\sqrt{3}}$ (1.1547).

of the CdS shell. We have previously observed that pyridine-capped CdSe nanocrystals are prone to oxidation in the TEM. This is presumed to be due to the desorption of the pyridine ligand from the nanocrystal surface in vacuum. [13] Core-shells are capped with amines as well and it may be assumed that these will desorb in the microscope vacuum. Nevertheless, full core-shell nanocrystals were found to be stable to oxidation in the TEM, which suggests that the CdS shell prevents photo-oxidation. Photo-oxidation requires the creation of charge carriers at the surface. Since the lowest energy states for excited carriers lie in the core, any carriers excited by the electron beam will likely relax to the core before participating in photo-oxidation. Those that do make it to the surface will oxidize the CdS shell, which may eventually degrade to the point where it no longer presents a sufficient barrier to prevent direct photo-oxidation of the core. Until this happens, core-shell nanocrystals should be very resilient to photo-oxidation. The lack of such resilience in thin-shelled nanocrystals suggests that they do not have a full shell. The stability of the core-shell nanocrystals has been independently confirmed from light-induced photo-oxidation experiments. [14]

Evidence for the shell structure also arises from the image contrast. As described in section 3.2.1.a, the contrast depends on the scattering power of the atoms making up the sample. Hence, for similar lattice parameters CdS is expected to show less contrast than CdSe. In the present case, there was a noticeable drop-off in image contrast across the last 2-3 layers of the core/shell crystals in Figure 3.8. To better visualize this change, intensity profiles along lattice planes in the images of Figure 3.8 were measured and are shown in Figure 3.10. Intensity profiles for the crystallites in Figure 2.15 are also included for comparison. High intensity (peaks) corresponds to white pixels in the image (channels in the crystal), whereas low intensity (troughs) indicates dark pixels (atoms in the lattice). Both the small cores and larger CdSe nanocrystals display a smooth drop-off in contrast near the edge of the nanocrystal. By comparison, the core/shell nanocrystals exhibit a step-wise drop in contrast. This is consistent with a core/shell structure. A change in nanocrystal thickness may also explain such contrast, but it is unlikely that this would occur in such a step-like fashion, and this has never been observed in any other II-VI nanocrystal sample. For comparison, the line scans corresponding to Figure 2.15 show a smooth drop-off over 1-2 lattice spacings.

The contrast change over the outer 2-3 layers tallies nicely with the 3-layer increase in nanocrystal radius upon shell growth as well as XPS data. [14] However, it should be emphasized that the use of intensity profiles is a rather crude way of determining the change in chemical composition. A proper HRTEM simulation would be more desirable. It is complicated by the difficulty in postulating a precise model structure. Unlike the case of the quantum onions, the lattice mismatch between CdSe and CdS is not negligible. There is a 3.9% mismatch with the CdS lattice having a smaller lattice constant. This implies that there is significant strain in these crystallites. Hence a model cannot be built simply by matching models of CdSe and CdS using bulk lattice parameters. Rather the strain has to be taken into account explicitly. Since the nature of the strain is unknown, this cannot be done in a rational way, but has to rely on a trial-and-error approach. However, the strain is very important to the image simulation, since it may result in localized tilt of the lattice, which will affect the image contrast. On the other hand, even if the contrast change is strain-induced, this argues for the presence of CdS in the outer shells, as there is no such effect observed in ordinary nanocrystals.

The HRTEM images do provide proof of epitaxy, as they demonstrate the crystallinity of the particles and discount the existence of incoherent domains or an amorphous phase. They do not provide proof of the core-shell structure, and so cannot disprove the possibility that the particles are alloys. Neither does it disprove the possibility that the CdS grows as a block attached to the CdSe core without enveloping it completely. However, all the evidence presented here, including the photo-oxidation behavior, and other experiments [14] are consistent with such a shell structure. In combination, this proves the epitaxial core-shell structure.

From a microscopist's point of view, the ultimate experiment to perform would be EELS-filtered imaging. This is a technique that generates the image from electrons that have undergone a specific energy loss while passing through the specimen. An image generated from a sulfur loss peak should provide direct, real-space evidence of the chemical distribution in these nanocrystals. Particularly appealing is that both lattice images and EELS-filtered images could be obtained from the same individual crystallites. Another intriguing aspect of this experiment is that it may reveal inhomogeneities in the shell thickness due to growth on the different faces.[1] The facilities for doing such an experiment are now available at NCEM and such an experiment is being considered for future studies.

3.4 Conclusions

Epitaxy can be performed on colloidal nanocrystals, leading to core-shell like structures. The morphology of the core is preserved in the final structure if growth defects can be minimized. The main defects encountered are growth faults in both zincblende and wurtzite structure. For three-dimensional growth, the morphological effect of such a fault is greater in the higher-symmetry zincblende structure than in the wurtzite lattice. This is in contrast to epitaxial growth on a single surface, where a plane defect parallel to the growth surface does not affect the final morphology in either structure.

In the absence of growth defects, growth proceeds without a change in particle morphology. The smooth growth of epitaxial shells indicates a layer-by-layer growth mode for colloidal nanocrystals similar to Frank Van der Merwe growth. Since CdSe

---

[1] The limitation being that EELS-filtered imaging is an incoherent imaging process with a lower resolution than lattice imaging.

nanocrystals themselves can be grown by multiple injections and these nanocrystals look identical to nanocrystals grown in a single injection, it suggests that this growth mode is active for regular nanocrystals.

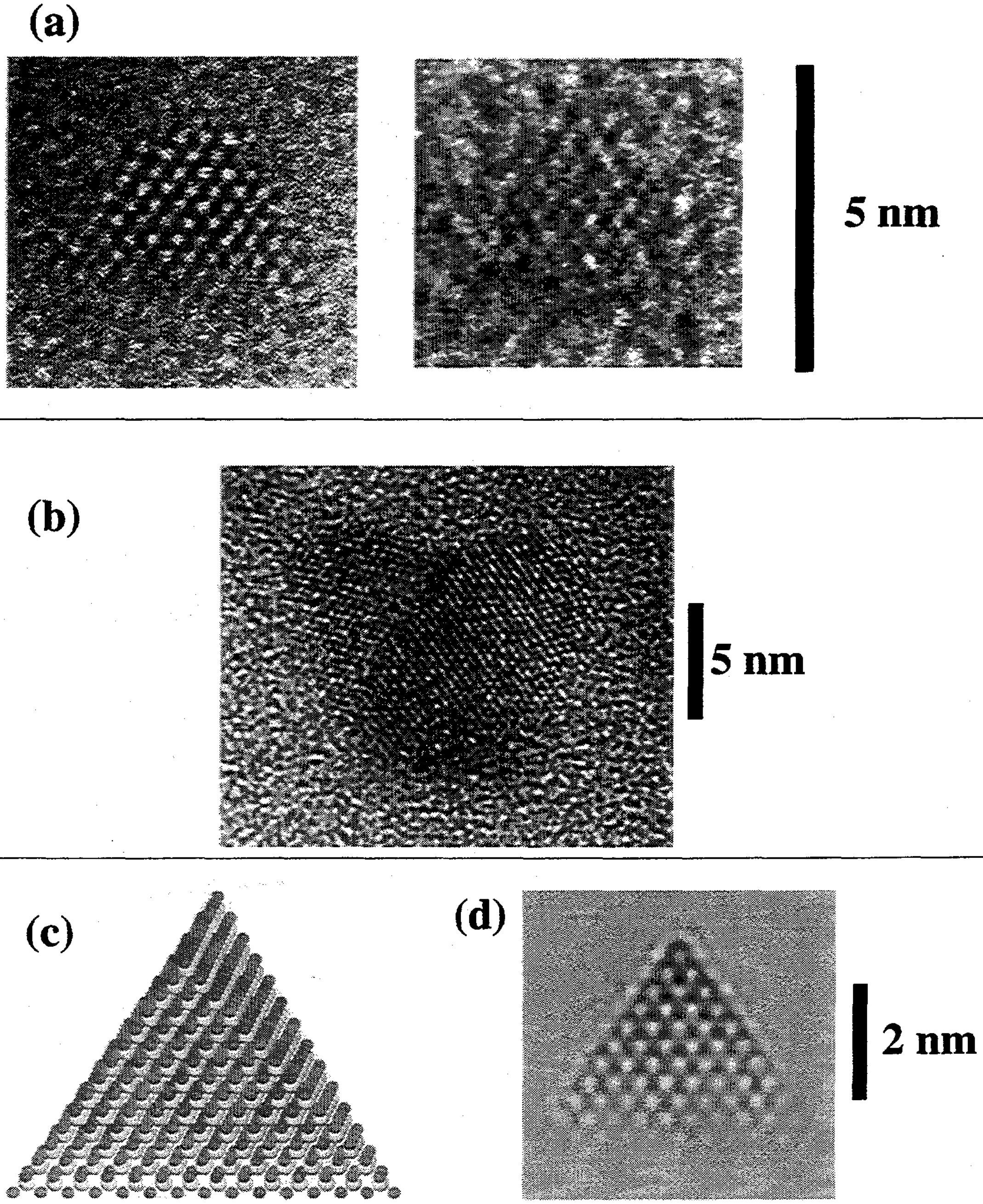

Figure 3.1: Tetrahedral CdS Cores

(a) CdS nanocrystals in [110] projection. Faceting along (111) planes is consistent with tetrahedral shape.

(b) Multiply-twinned CdS nanocrystal with ear-like outgrowths, [110] projection.

(c) Structural model for a Cd-(111) terminated CdS nanocrystal, 4 nm edge length.

(d) Simulated HRTEM micrograph for nanocrystal from (c) in [110] projection.

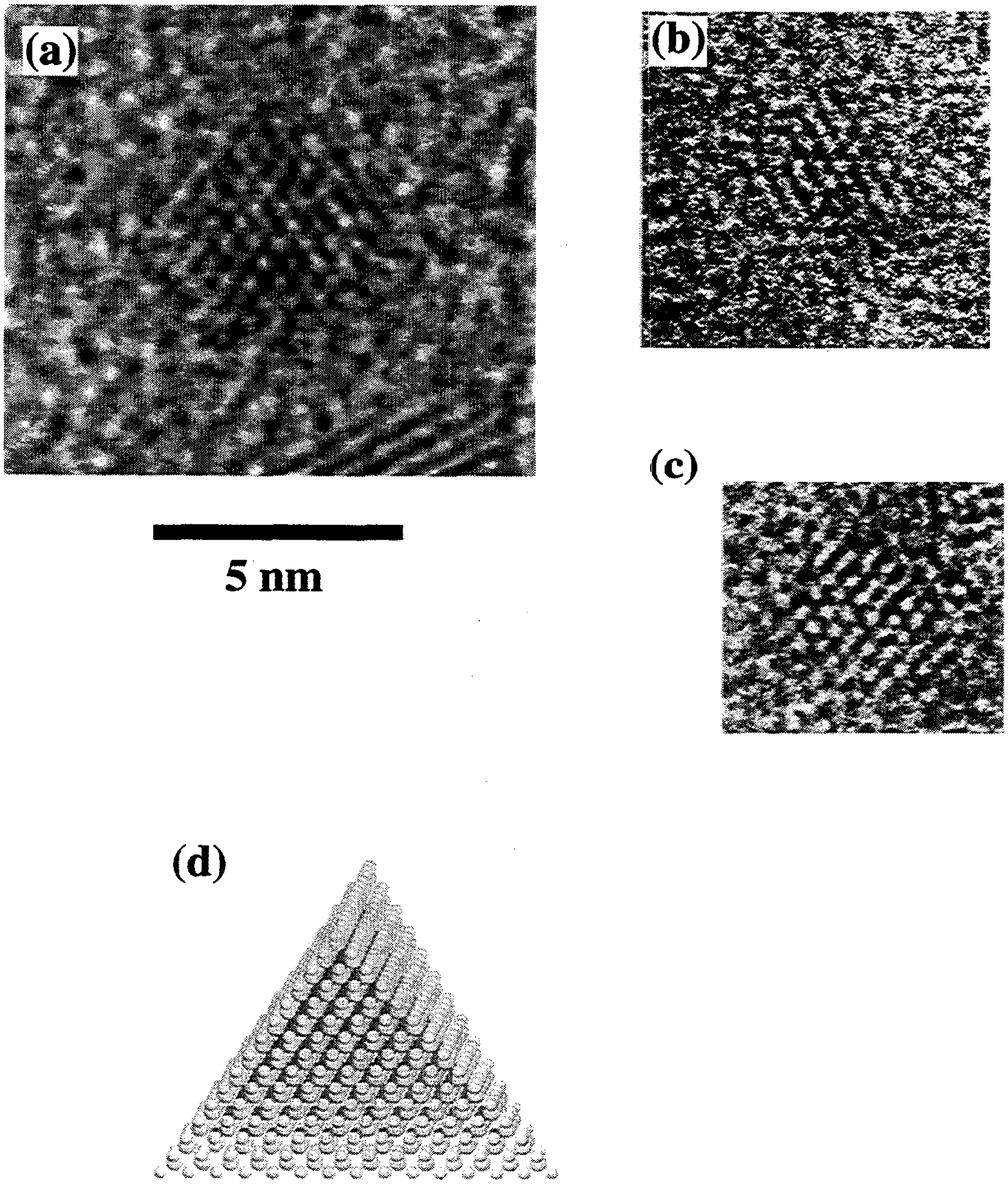

Figure 3.2: CdS/HgS Core-Shells

CdS nanocrystals after growth of one layer of HgS. [110] projection. The particles were rather unstable, making it difficult to obtain good images.

(a)-(c) The tetrahedral motif is essentially preserved.

(d) Same as Figure 3.1 (c), but with the outermost Cd layer replaced with Hg.

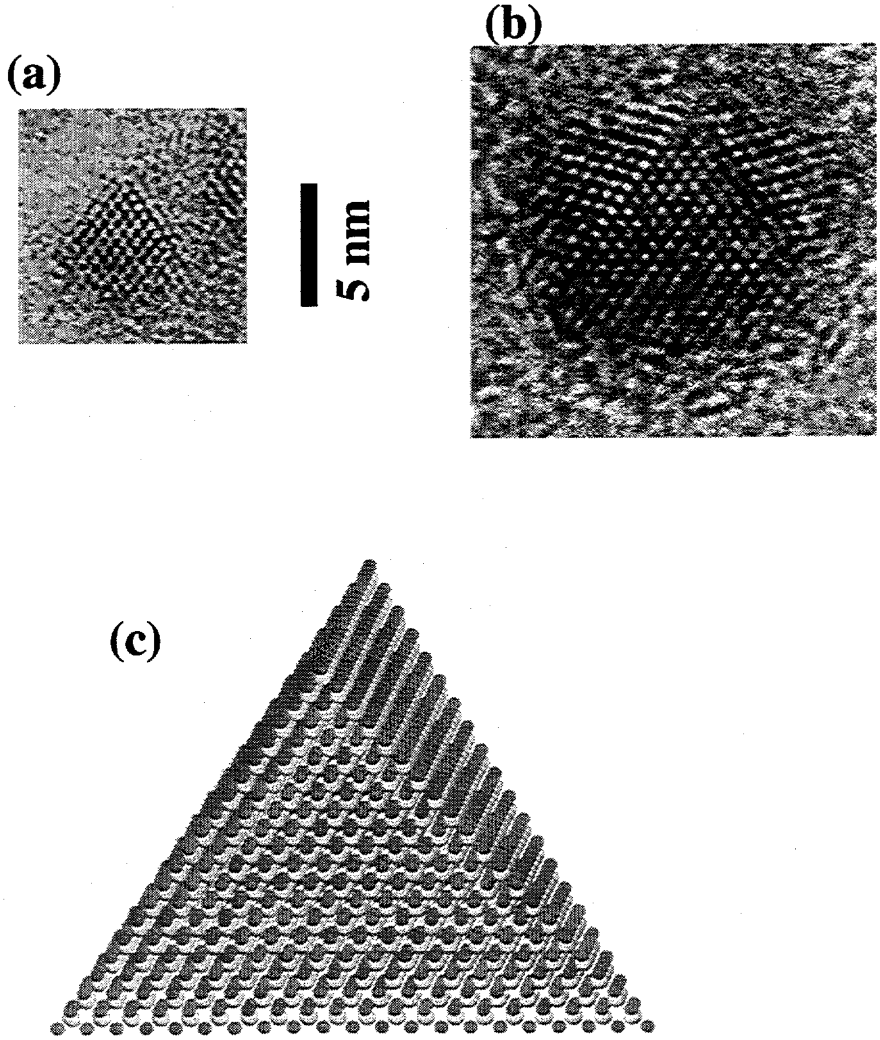

Figure 3.3: CdS/HgS/CdS Nanocrystals
Quantum Onions: CdS/HgS/CdS QDQW's.
(a) A normal, tetrahedral crystallite. [110] projection.
(b) The main, tetrahedral defect structure.
(c) Structural Model for a normal, tetrahedral onion structure.

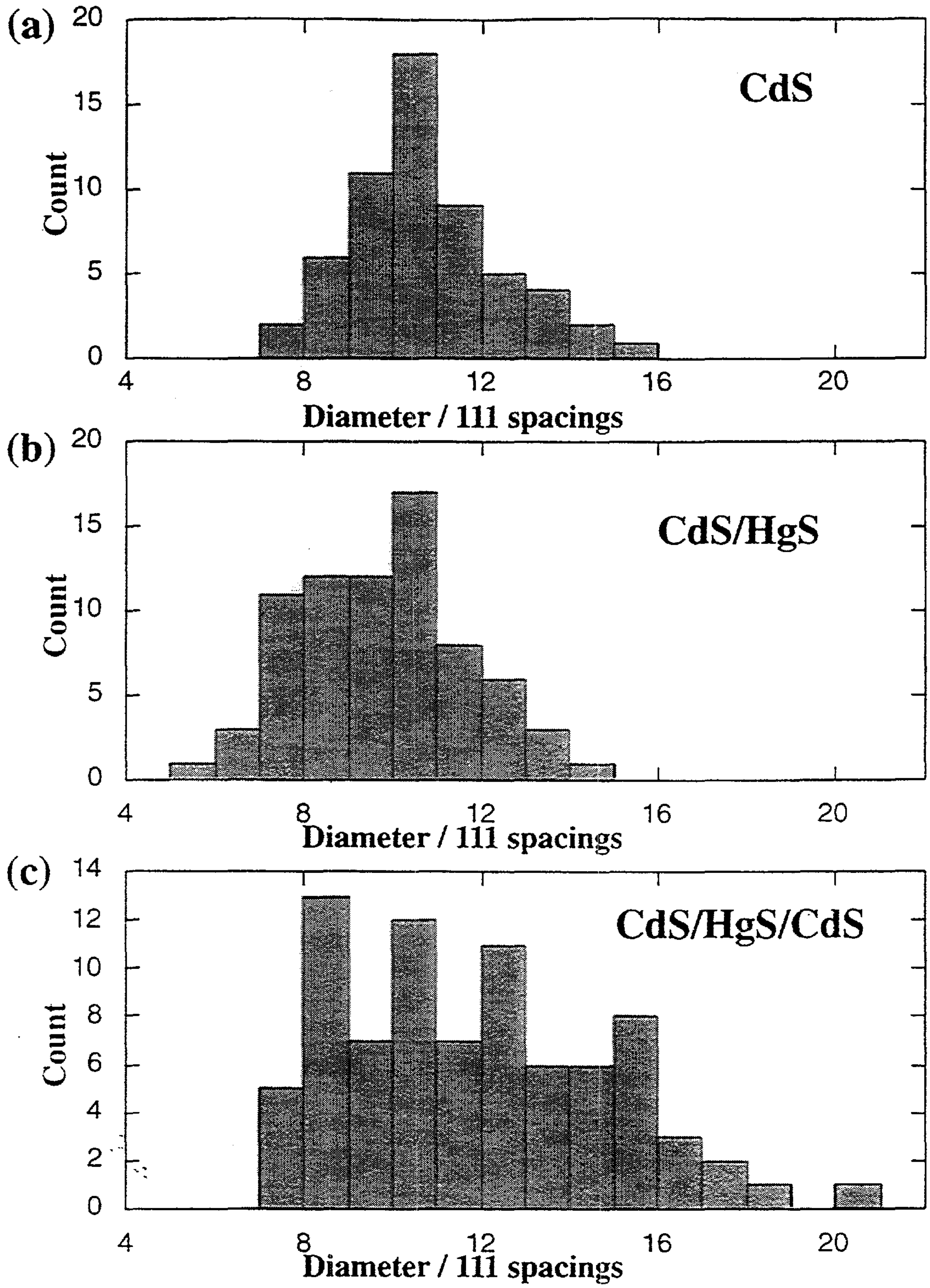

Figure 3.4: Size Evolution from CdS to QDQW

Size distributions from HRTEM sizing of (a) CdS nc's, (b) CdS/HgS core-shells (1 monolayer HgS) derived from (a), and (c) CdS/HgS/CdS QDQW's derived from (b). Measured in units of the CdS {111} spacing.

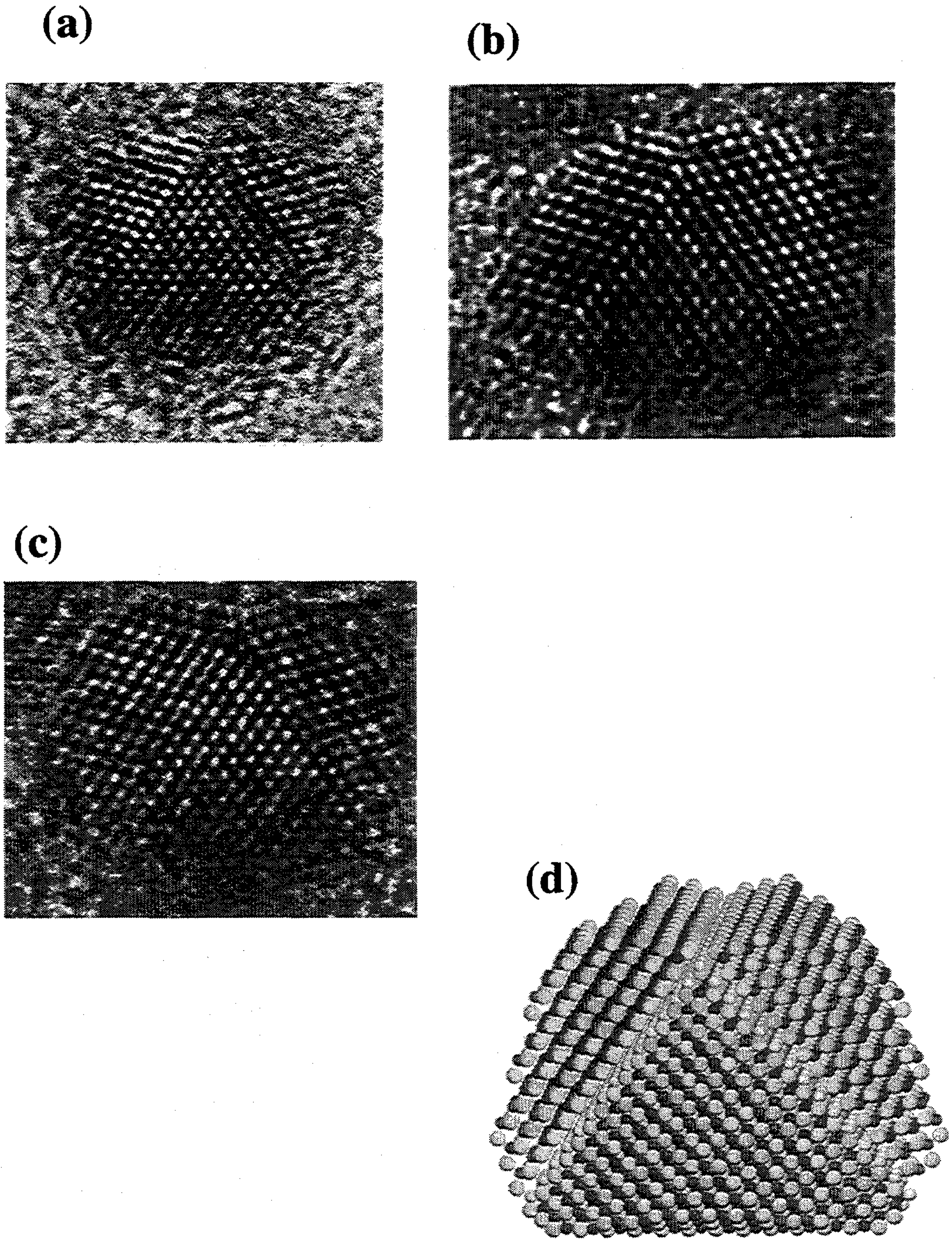

Figure 3.5: Onions with Ears
(a)-(c) Multiply-twinned QDQW's from several samples.
(d) Model structure for the "Quantum Onion" with Ears.

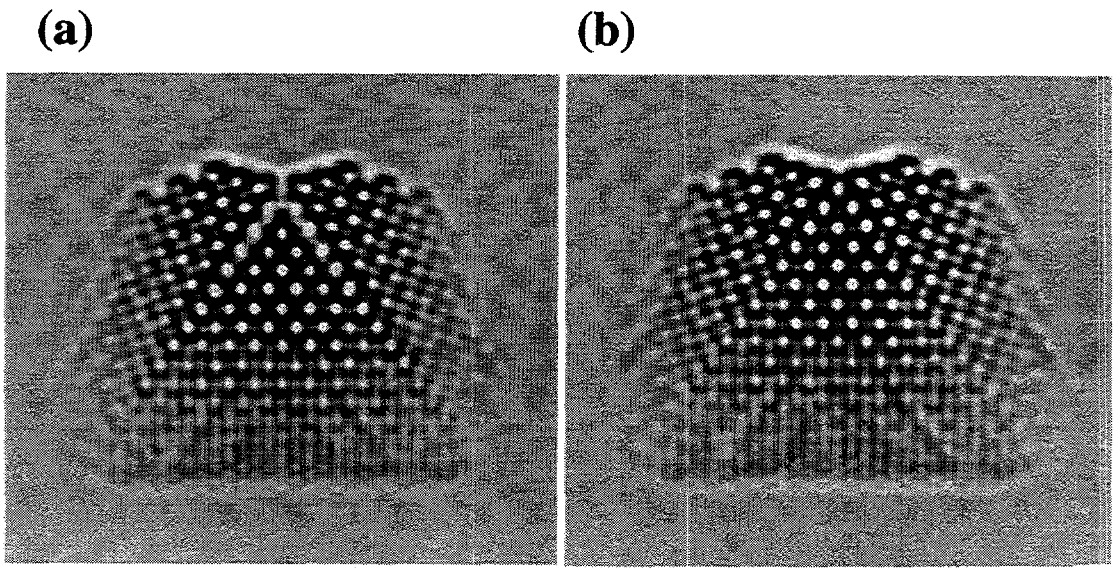

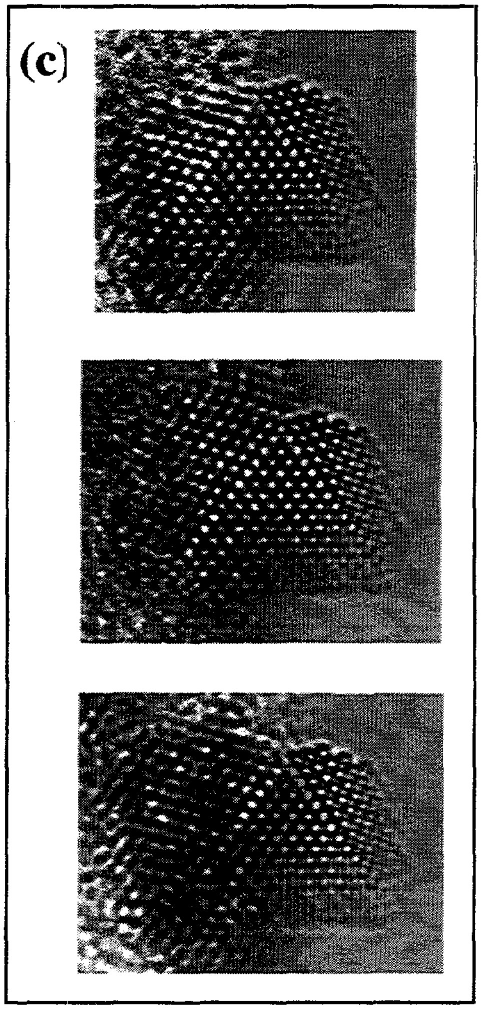

Figure 3.6: TEM Simulations of Multiply Twinned QDQW's

(a) HRTEM Simulation of the model in Figure 3.5 (d). The HgS layer introduces a change in contrast at the stacking fault.

(b) HRTEM Simulation for the same structure with Hg replaced by Cd. No contrast change is observed.

(c) The simulation overlaid with several experimental images.

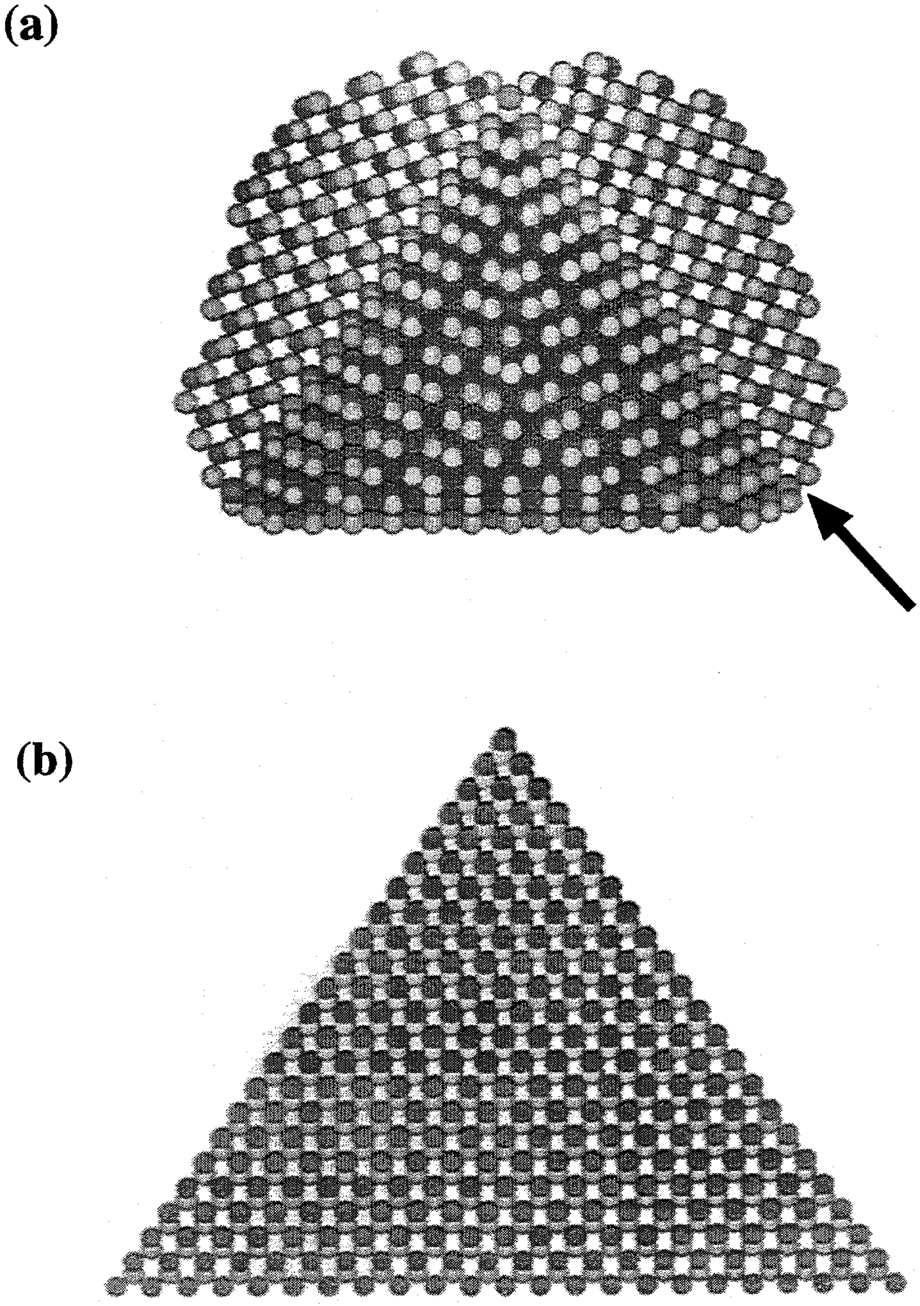

Figure 3.7: QDQW Model

(a) Model of an eared nanocrystal in [110] projection. The HgS layers(arrow) are unobscured, and the projected potentials at the stacking fault arise from equal thicknesses of HgS and CdS.

(b) By comparison, in a tetrahedral nanocrystal the HgS layers are obscured by CdS and hence not visible in a the ball-and-stick model. The projected potential will then be an average of the HgS and CdS potentials.

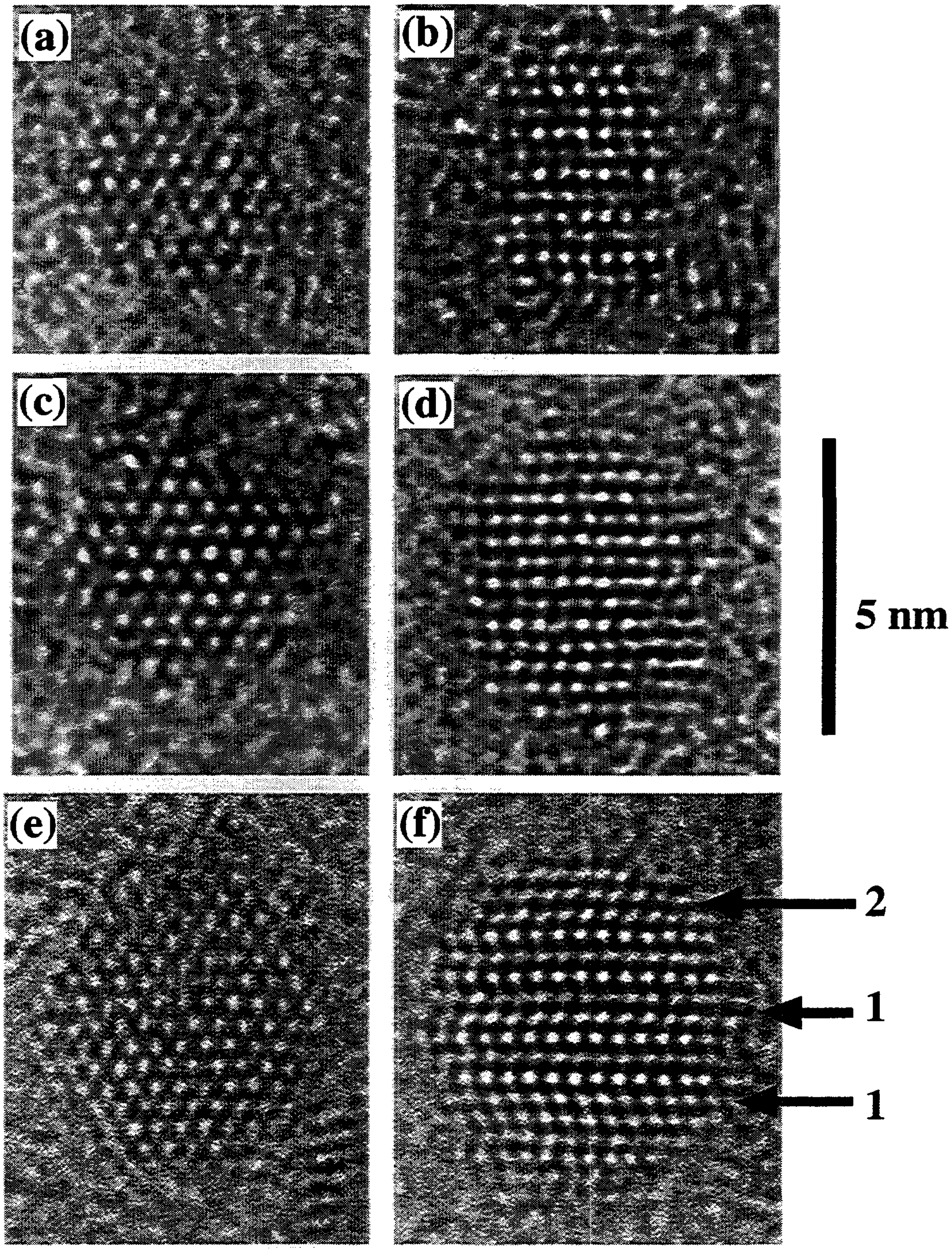

Figure 3.8: CdSe/CdS Core-shell Nanocrystals

CdSe cores in (a) [001] and (b) [010] projection.

CdSe cores with a thin shell of CdS in (c) [001] and (d) [010] projection.

CdSe cores with a thick shell of CdS in (e) [001] and (f) [010] projection. Arrows mark stacking faults in the crystallite: (1) Stacking fault traverses the core and extends through the shell. (2) Stacking fault grown in the shell. (Though possibly a partially disordered phase.)

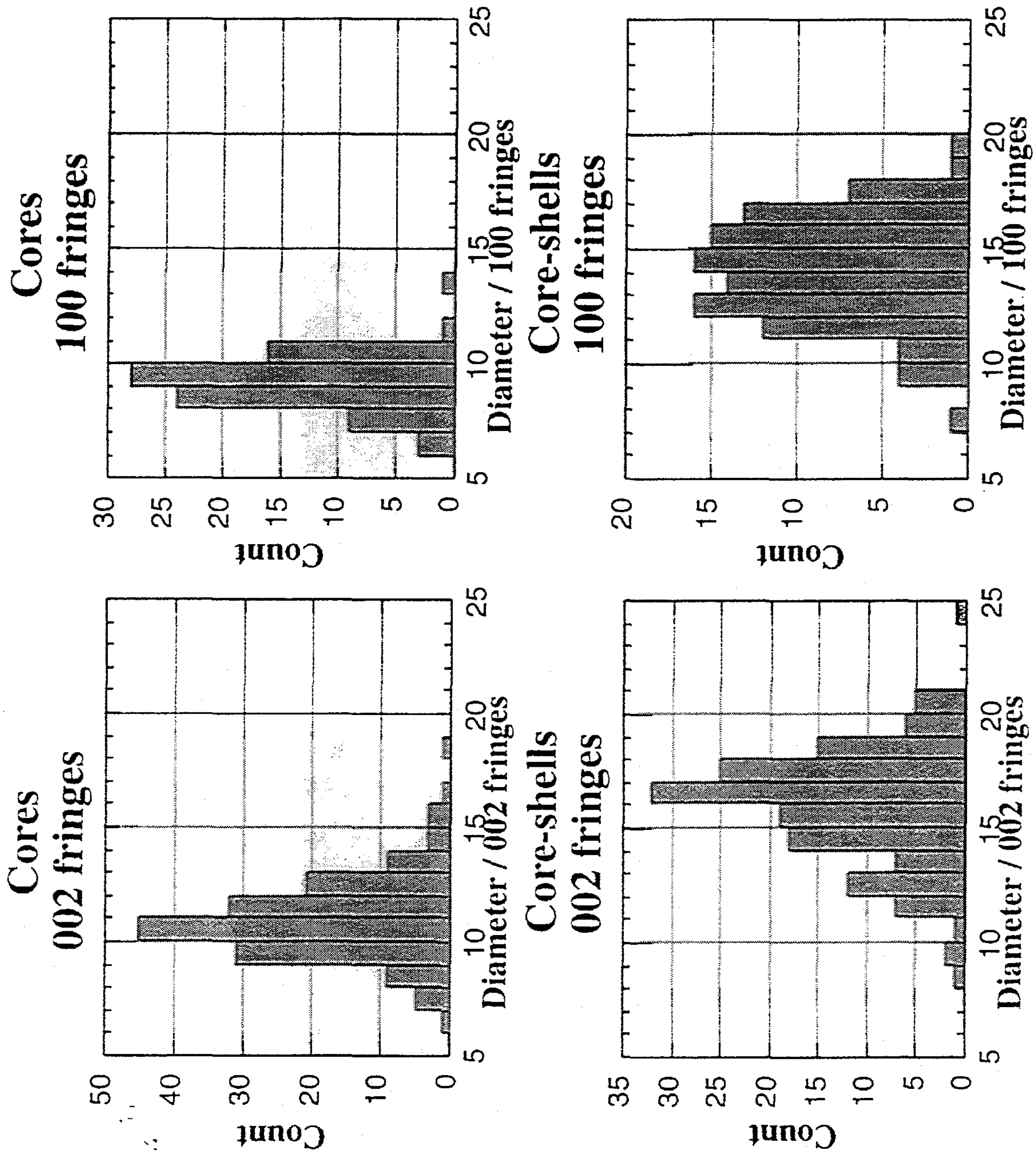

Figure 3.9: Size Evolution of Core-shell nanocrystals

Size Distributions in the major and minor axes, determined from HRTEM sizing. In units of lattice spacings.

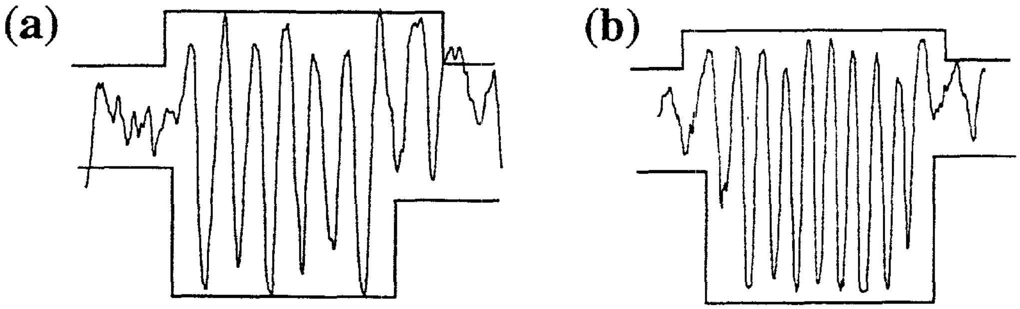

Core 001

Core 010

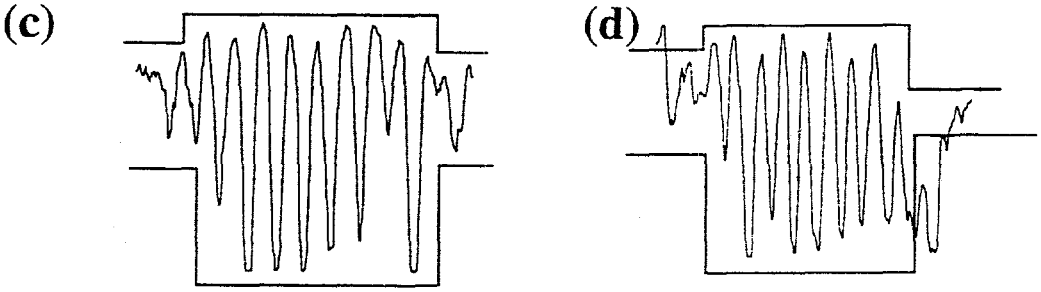

Thin Shell 001

Thin Shell 010

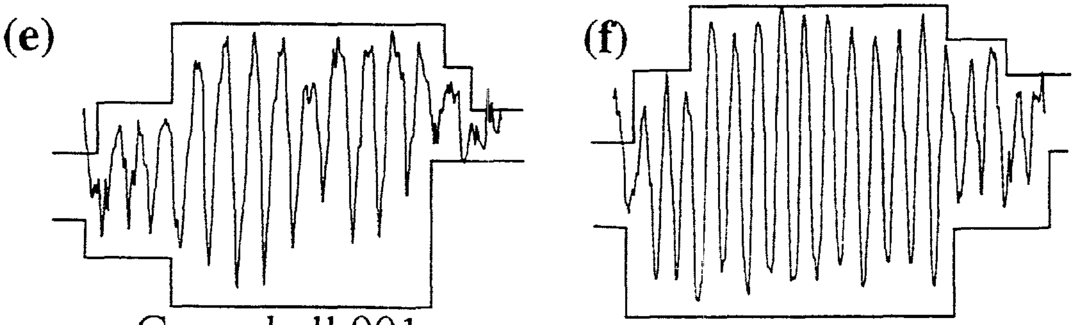

Core-shell 001

Core-shell 010

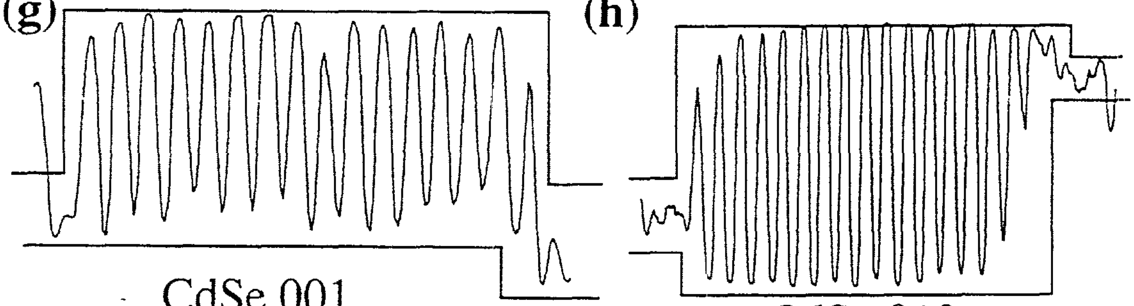

CdSe 001

CdSe 010

Figure 3.10: Intensity Profiles Across Core-shell Samples

(a)-(f)Line scans along <100> for the crystallites in Figure 3.8 and (g), (h) for the crystallites in Figure 2.15 for comparison.

Large values (peaks) correspond to white pixels (channels in the crystal structure). Low values (troughs) are atoms. The horizontal/vertical lines are guides to the eye to indicate areas of equal contrast.

Thebackground may be (and frequently is) at different gray levels on opposite sides of the crystal.

Chapter 4: Ordered nanocrystal layers

> *I am, as I said, inspired by the biological phenomena in which chemical forces are used in repetitious fashion to produce all kinds of weird effects (one of which is the author).*
>
> —*Richard P. Feynman, 1959*

Biology uses self-assembly of simpler molecules to create a variety of higher-order structures. Perhaps the best known example is the lipid bilayer forming cell walls, a fairly simple construct that nevertheless provides much functionality. Self-assembly provides an appealing route to the creation of higher order structures from nanocrystals as it is a very cheap and scalable process. What could be easier than throwing a bunch of molecules into a beaker and sitting back as they arrange themselves into an interesting superstructure? What could be more profitable than feeding a batch of molecular components into a vessel and sitting back as they form a useful device on their own? For nanotechnology to be commercially viable, self-assembly will have to be a crucial component of any manufacturing process. It is then interesting to investigate what assembly processes one might experience with nanocrystals.

A closer look at Figure 2.1 shows that in various areas, the nanocrystals have aggregated into locally close-packed layers. Indeed particles are usually found in islands on the TEM grid. Presumably this is an artifact of the specimen preparation process. A mechanism for this has been proposed. [82, 83] The nanocrystals adhere to the carbon substrate due to van der Waals forces between the carbon and the organic ligands. The crystallites similarly interact with each other and with the solvent. As the solvent evaporates, the liquid collects into drops. If the interaction between the particles and the solvent is stronger than the particle-substrate attraction, then nanocrystals can move along the substrate to stay within the droplet as it evaporates until the concentration exceeds solubility threshold. At this point the particles precipitate out of solution onto the substrate with the arrangement they had in the droplet.

If the evaporation process is sufficiently slow, the particles will be able to reach their equilibrium positions within the droplet by Brownian motion. As the droplet size decreases, the equilibrium configuration should be the one maximizing the nanocrystal packing density within the drop. For a narrow size distribution, this problem reduces to arranging the particles in a crystalline superlattice arrangement. For the right combination of solvent, capping group, and substrate, this will result in a crystalline monolayer, such as the ones seen in Figure 4.1 for size-selected InAs samples deposited from toluene onto carbon film. Such arrangements have been seen over μm-sized areas with these particles. However, as can be seen from the fringe contrast inside individual crystallites, the nanocrystals are still arranged with random orientations within the layer.

Orientation within the layer can be achieved however. Figure 4.2 (a) shows a monolayer array of CdSe nanocrystals on a Formvar substrate, prepared by Dr. Xiaogang Peng in our group. The nanocrystals were deposited by exposure of the substrate to a nanocrystal containing solution. Just like with the InAs sample, the nanocrystals self-assembled into a hexagonal close-packed array on the substrate as the solvent evaporated. This is somewhat more evident from part (b) of the figure, which is the Fourier transform (FT) of the image. This is equivalent to the diffraction pattern of the array and clearly indicates hexagonal closest packing in the plane. Even at the low magnification of the image, the faceting is evident.

Furthermore, nanocrystals are aligned with their polar axes perpendicular to the substrate and with their facets facing each other. This in fact takes place over quite long ranges. Figure 4.2 (c) shows a SAD pattern from an area approximately 1 μm in diameter. Rather than being an ordinary powder pattern of concentric rings the intensity along the rings varies in a six-fold symmetric fashion. This is particularly evident along the 100 ring. Furthermore, the 002 and 103 rings are almost entirely missing from the pattern, indicating that the [001] axes of the nanocrystals are perpendicular to the substrate. The same effect can be observed in a higher resolution FT of the image. This is demonstrated in Figure 4.3. Part (a) is an enlarged view of the image in Figure 4.2. Figure 4.3 (b) is the FT of Figure 4.3 (a). The indexed intensity maxima correspond to diffraction from the interior of the nanocrystals and are indexed accordingly. The 002 reflections are absent, indicating alignment of the <[001]> axis perpendicular to the substrate. The 100 reflections are concentrated in a six-fold symmetric pattern, indicating the common orientation within the plane. For reference the FT of a single oriented nanocrystal is shown in Figure 4.3 (c). Finally, Figure 4.3 (d) is an enlarged view of the central portion of the FT in part (b) which corresponds to the low angle diffraction signature of the array. In addition to the hexagonal close-packed nature of the array, this also illustrates the 30° rotation to the unit cell of the nanocrystals.

Finally it needs to be noted that such oriented packing is not observed in smaller nanocrystals. The particles shown in Figure 4.3 are quite large (~8 nm diameter) and elongated along the [001] axis. The aspect ratios of some of these particles approach 2. This means that efficient packing does not take place with the [001] axis in the plane of the substrate which presumably aids in the alignment process similarly to the case of CdSe nanocrystal superlattices. [71] The large size also facilitates orientation within the plane since in smaller particles the shape is smoothed out by the soft surface ligands. This leads to the random orientation in the InAs case, which is best described by soft-sphere packing. However, it may be possible to achieve alignment in smaller nanocrystals by adjusting the surface ligand. In particular, shorter ligands should preserve more of the nanocrystal shape in its interaction with its environment.

The alignment effect is particularly exciting because of the polar nature of these nanocrystals. [44] Having all the dipoles aligned may create interesting nonlinear optical effects.

All the arrangements discussed so far may appear intuitively obvious as they merely involve closest packing of objects in a plane. However, one can envision other arrangements by tailoring the various facets with different ligands. Such configurations may lead to non-close-packed arrangements such as those observed by Bowden. [84]

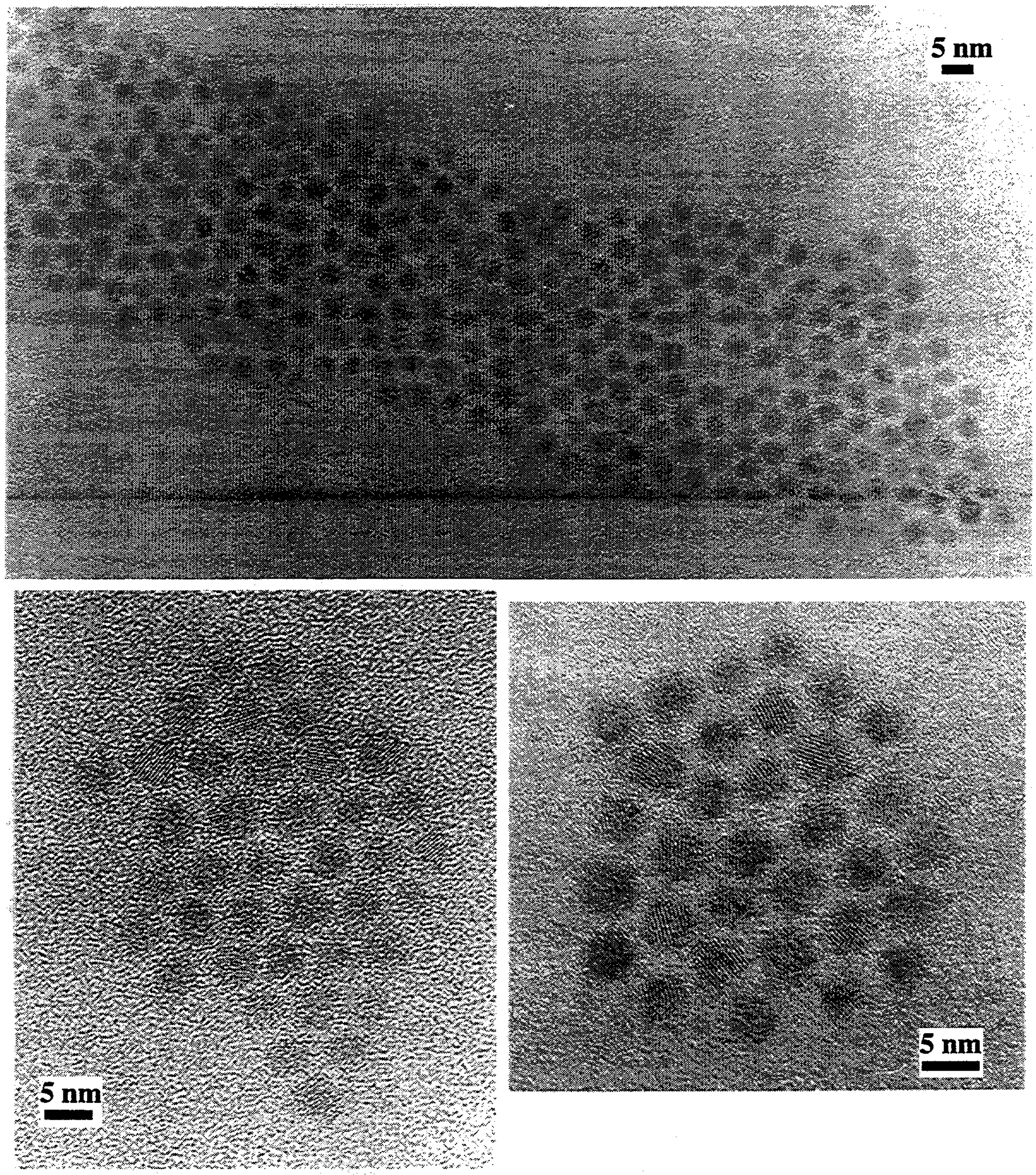

Figure 4.1: Ordered InAs Nanocrystals

Islands of InAs nanocrystals on amorphous carbon film. The nanocrystals locally order into closest-packed arrays.

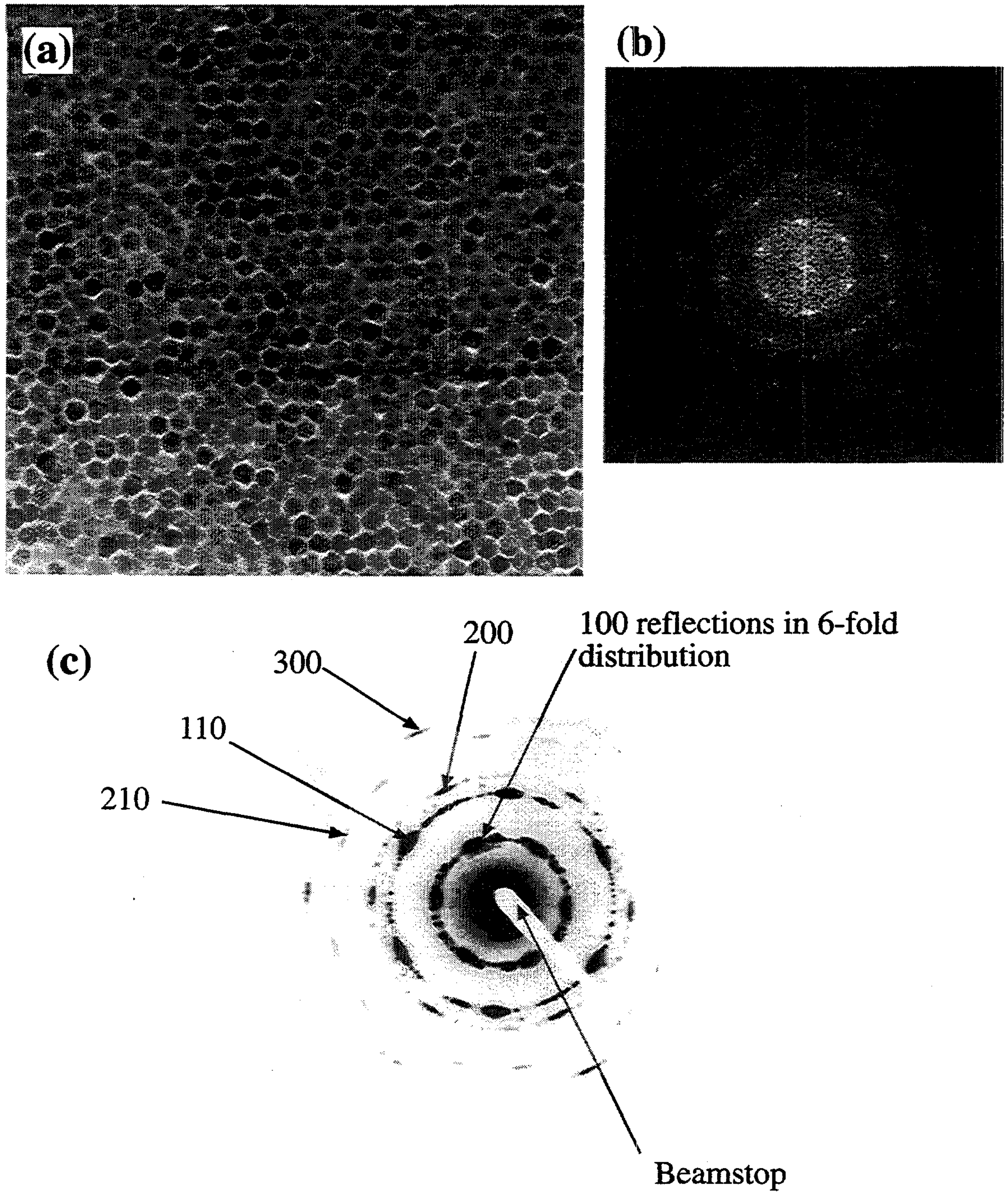

Figure 4.2: Oriented CdSe Nanocrystals

(a) Single monolayer array of CdSe nanocrystals on formvar film.

(b) Fourier Transform of the image in (a), showing hexagonal periodicity indicative of closest packing in a plane.

(c) Selected Area Electron Diffraction (negative) pattern from 1 μm diameter area of an array. Various reflections are indicated.

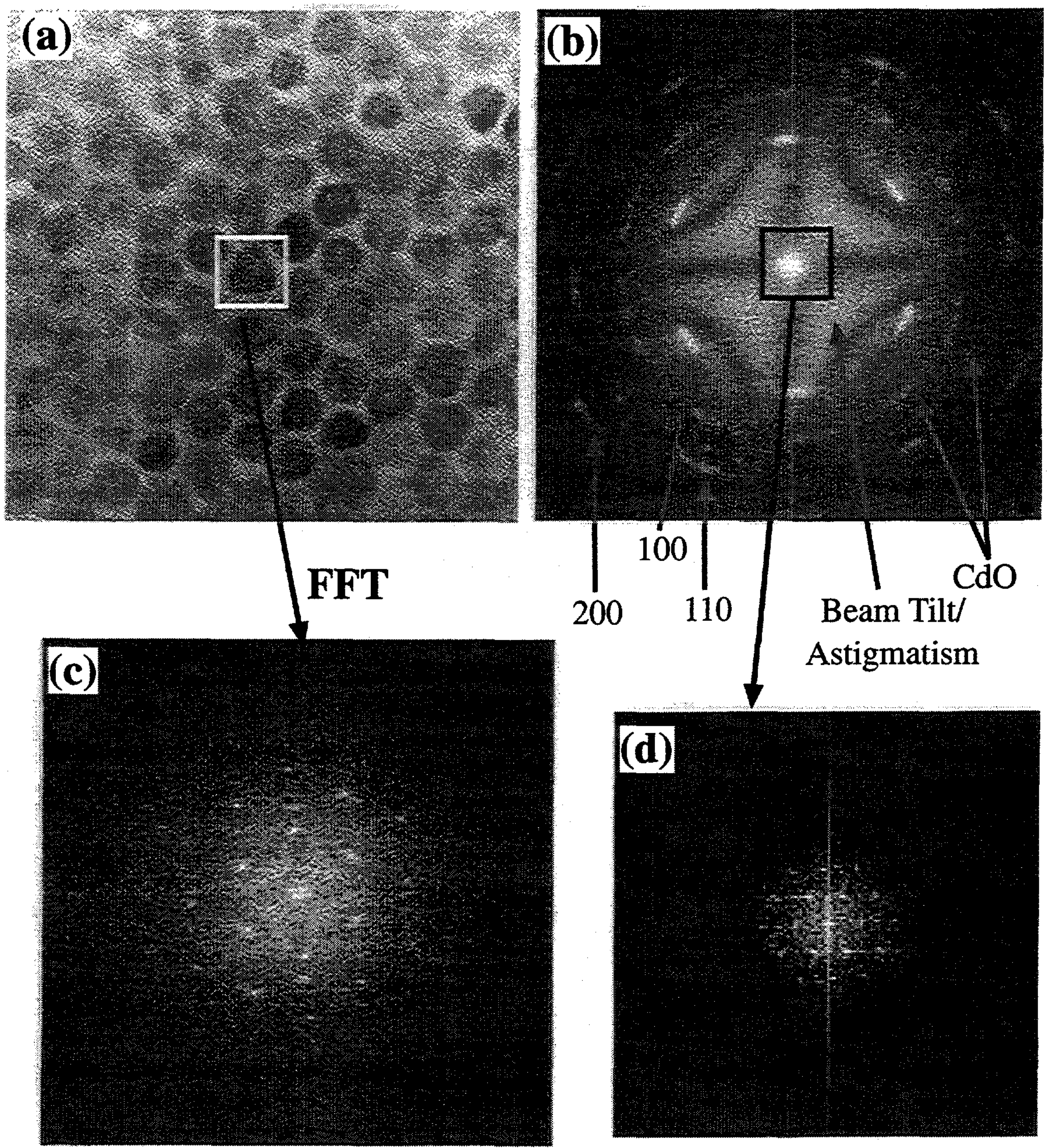

Figure 4.3: Oriented CdSe Nanocrystals, High Resolution

(a) Enlarged view of portion of Figure 4.2 (a).

(b) Fast Fourier Transform of part (a). The spots visible are due to the the lattice periodicity within the crystallites. Some extraneous rings have been identified as CdO (formed through beam-induced oxidation of the nanocrystals). The cross-hair like, diffuse intensity distribution in the center is due to beam tilt and/or astigmatism in the TEM.

(c) Fourier Transform of the central nanocrystal of (a). The orientation of the diffraction spots is the same as in (b).

(d) Enlarged view of the central portion of (b). This corresponds to low-angle diffraction, i.e. these are the superlattice spots, similar to Figure 4.2 (c). Note the 30° rotation to the FT's in (b) and (c).

Conclusions

> *The search for truth is in one way hard and in another easy, for it is evident that no one can master it fully or miss it completely. But each adds a little to our knowledge of nature, and from all the facts assembled there arises a certain grandeur.*
>
> *—Aristotle*

The morphologies of colloidal semiconductor nanocrystals were investigated using High Resolution Transmission Electron Microscopy. Unlike the conventional theoretical assumption of spherical particles, these nanocrystals were observed to adopt faceted shapes. These shapes were consistent with Wulff polyhedra with the stabilizing effects of surface ligands taken into account, suggesting that these equilibrium crystal shapes (ECS) for the nanocrystal/ligand systems.

For TOPO-capped, wurtzite CdSe nanocrystals grown at 350°C the observed morphology was a truncated hexagonal prism consisting primarily of {100} and {001} surfaces. The prism edges were rounded off by {101}{103} surfaces/steps. The nanocrystals were elongated along the [001] axis, with typical aspect ratios around 1.1-1.2. The highest point group symmetry achievable with this morphology is C_{3v}, which is consistent with spectroscopic data on these nanocrystals. The major crystal defect observed is the presence of growth faults in the [001] direction, which does not significantly affect the particle morphology.

The faceting also affects the packing of large (~8nm diameter along <100>) crystallites into ordered arrays. These crystallites align facet-to-facet resulting in oriented packing. This contrasts with smaller crystallites where packing occurs with random orientation, presumably because the surface ligands blunt the shape.

The morphology can be changed by annealing at high temperature, which is assumed to remove the surface ligands. At ~550°C the {001} surface of a CdSe nanocrystal is observed to refacet along {103} planes, similar to the reconstruction of the bulk surface.

Zincblende CdS nanocrystals grown in aqueous media and capped by polyphosphate anions demonstrate the strong effect that the surface ligands exert on nanocrystal morphology. These nanocrystals have tetrahedral shapes, terminated in {111} surfaces. The tetrahedral morphology suggests that the anionic ligands have preferentially stabilized the Cd {111} surfaces over the S {111} surfaces. Rotation twin faults similar to the growth faults in wurtzite CdSe constitute the major crystal defect and markedly affect the nanocrystal morphology, lowering the symmetry from T_d.

Various III-V zincblende nanocrystals (InP, InAs) capped by TOP or TOPO were shown to have shapes dominated by {111} and {100} surfaces. Individual morphologies varied within this constraint with both truncated octahedral shapes and some occurrence of tetrahedral shapes. Rotation twin faults again constitute the major defect, resulting in morphologies that retain some characteristics of the above-mentioned shapes, but overall are of low symmetry. The discussion of morphology is complicated by the sensitivity to oxidation and beam damage in the TEM.

Si nanocrystals grown by gas-phase pyrolysis and capped by an amorphous oxide layer were found to be quasi-spherical at large sizes, but all sizes showed faceting, predominantly along {111} planes. {100} and {110} facets contributed to a lesser extent. A large portion of the observed nanocrystals contain a twins in <111> orientation near the center of the nanocrystal. This may point to its presence in the initial nucleus, but further study is necessary to validate that claim.

CdS/HgS/CdS quantum onion nanocrystals were shown to have an epitaxial structure that maintains the tetrahedral morphology of the zincblende CdS nanocrystals from which they were grown. The HgS layer creates a tetrahedral shell around the CdS core. Rotation twin faults frequently occur at the interface between CdS and HgS layers, but it is not known at this stage whether this is caused by the growth of the HgS layer.

Wurtzite CdSe/CdS core-shell nanocrystals were shown to be epitaxial in nature as well, despite the large lattice mismatch. The morphology of the final core-shell crystallites mimics that of the original CdSe cores. Even stacking faults originally present in the core propagate through the shell. This suggests a layer-by layer growth mode on the original nanocrystal seeds, similar to Frank Van der Merwe growth on bulk surfaces. The similarity of the reaction conditions to ordinary nanocrystal synthesis also suggests that this growth mode is equally valid for plain nanocrystals.

Concluding Remarks

The morphologies of colloidal nanocrystals are clearly more complex than simple spheres. The study of these morphologies can provide insight into the electronic and chemical properties and to some degree even aid in understanding the synthetic process. This in turn allows one to improve the synthesis to make better samples.

Nanocrystals come in a variety of shapes, dictated by their unit cell structure and surface passivation. The nature of the surface ligands is one of the most crucial parameters determining the shape. It is also the parameter that is most amenable to chemical manipulation. Currently, thermodynamic and kinetic parameters (reaction temperature, reagent concentrations, speed of injection) control most of the aspects of nanocrystal synthesis. This is appealing since it allows one particular synthesis method to be adapted to many different chemical systems. The price is that no synthesis is optimal for every sample. One can imagine though that eventually ligands will be customized for particular syntheses with the express goal of optimizing a synthesis for a given size and morphology. Nature uses such templating in the process of biomineralization with very high selectivity and efficiency. Alternatively it may be possible to use surface selective ligands after the synthesis to separate nanocrystals according to size or shape.

As every organic chemist knows, the most minute differences can be exploited to create something new out of something ordinary. Being able to selectively interact with different surfaces allows one to put “handles” on nanocrystals. With these handles, nanocrystals can be oriented, linked, and generally manipulated in a controlled fashion. At this point, the concept of a “molecular lego” will be reality.

References

1. Williams, D.B. and Carter, C.B., *Transmission electron microscopy : a textbook for materials science.* 1996, New York: Plenum Press.
2. Hirsch, P.B., *Electron microscopy of thin crystals.* 1977, Malabar, Fla.: R.E. Krieger Pub. Co.
3. Edington, J.W., *Practical electron microscopy in materials science.* 1976, New York: Van Nostrand Reinhold Co.
4. Spence, J.C.H., *Experimental high-resolution electron microscopy.* 1988, New York: Oxford University Press.
5. Reimer, L., *Transmission electron microscopy : physics of image formation and microanalysis.* 1993, Berlin, New York: Springer-Verlag.
6. Goldstein, A.N., *The thermodynamic properties of semiconductor nanocrystals.* 1993, Doctoral Dissertation, Department of Chemistry, University of California, Berkeley, CA 94720.
7. Iijima, S. and Ichihashi, T., *Structural Instability of Ultrafine Particles of Metals.* Physical Review Letters, 1986. **56** (6): p. 616-619.
8. Iijima, S., *Thin graphite support films for high resolution electron microscopy.* Micron, 1976. **8** : p. 41-46.
9. Cowley, J.M. and Moodie, A.F., Acta Crystallographica, 1957. **10** : p. 609.
10. Bevington, P.R. and Robinson, D.K., *Data reduction and error analysis for the physical sciences.* 1992, New York: McGraw-Hill.

11. Efros, A.L. and Rodina, A.V., *Band-edge absorption and luminescence of nonspherical nanometer-size crystals.* Physical Review B (Condensed Matter), 1993. **47** (15): p. 10005-7.

12. Efros, A.L., Rosen, M., Kuno, M., Nirmal, M., Norris, D.J., and Bawendi, M., *Band-edge exciton in quantum dots of semiconductors with a degenerate valence band: dark and bright exciton states.* Physical Review B (Condensed Matter), 1996. **54** (7): p. 4843-56.

13. Bowen Katari, J.E., Colvin, V.L., and Alivisatos, A.P., *X-ray Photoelectron Spectroscopy of CdSe Nanocrystals with Applications to Studies of the Nanocrystal Surface.* Journal of Physical Chemistry, 1994. **98** (15): p. 4109-17.

14. Peng, X.G., Schlamp, M.C., Kadavanich, A.V., and Alivisatos, A.P., *Epitaxial growth of highly luminescent CdSe/CdS core/shell nanocrystals with photostability and electronic accessibility.* Journal Of the American Chemical Society, 1997. **119** (30): p. 7019-7029.

15. Murray, C.B., Norris, D.J., and Bawendi, M.G., *Synthesis and Characterization Of Nearly Monodisperse CdE (E = S, Se, Te) Semiconductor Nanocrystallites.* Journal Of the American Chemical Society, 1993. **115** (19): p. 8706-8715.

16. Shiang, J.J., Kadavanich, A.V., Grubbs, R.K., and Alivisatos, A.P., *Symmetry of Annealed Wurtzite CdSe Nanocrystals: Assignment to the C_{3v} Point Group.* Journal of Physical Chemistry, 1995. **99** (48): p. 17417-17422.

17. Hartmann, H., *On the growth of Hexagonal ZnSe single crystals.* Kristall und Technik, 1970. **5** (4): p. 527-34.

18. Kaito, C., Fujita, K., and Shiojiri, M., *Growth of tetrapod-like crystals in CdS smoke prepared by gas evaporation.* Journal of Crystal Growth, 1982. **57** (1): p. 199-202.

19. Seacrist, L. and Munir, Z.A., *Studies on the Sublimation of IIB-VIA Compounds*

IV. The Anisotropic Behavior of the Sublimation of Basal-Plane Oriented Crystals of Cadmium Selenide. High Temperature Science, 1971 : p. 340-348.

20. LaFemina, J.P., *Total-energy calculations of semiconductor surface reconstructions.* Surface Science Reports, 1992. **16** (4-5): p. 133-260. And references therein.

21. Allais, M. and Gandais, M., *Habit and structure of Cd(S,Se) quantum dots in silicate glasses: high-resolution transmission electron microscopy.* Philosophical Magazine Letters, 1992. **65** (5): p. 243-8.

22. Ekimov, A.I., Hache, F., Schanne-Klein, M.C., Ricard, D., Flytzanis, C., Kudryavtsev, I.A., Yazeva, T.V., Rodina, A.V., and Efros, A.L., *Absorption and intensity-dependent photoluminescence measurements on CdSe quantum dots: assignment of the first electronic transitions.* Journal of the Optical Society of America B (Optical Physics), 1993. **10** (1): p. 100-7.

23. Hill, N.A. and Whaley, K.B., *Electronic structure of semiconductor nanoclusters: a time dependent theoretical approach.* Journal of Chemical Physics, 1993. **99** (5): p. 3707-15.

24. Mattoussi, H., Cumming, A.W., Murray, C.B., Bawendi, M.G., and Ober, R., *Characterization of CdSe nanocrystallite dispersions by small angle X-ray scattering.* Journal of Chemical Physics, 1996. **105** (22): p. 9890-6.

25. Murray, C.B., *Ph.D. Dissertation*. 1995, Ph.D. Dissertation, Department of

Chemistry, Massachusetts Institute of Technology, Cambridge.

26. Champagnon, B., Adrianasolo, B., Ramos, A., Gandais, M., Allais, M., and Benoit, J.-P., *Size of Cd(S,Se) quantum dots in glasses: Correlation between measurements by high-resolution transmission electron microsocopy, small-angle x-ray scattering, and low-frequency inelastic Raman scattering.* Journal of Applied Physics, 1993. **78** (6): p. 2775-2779.

27. Kostorz, G., *Inorganic Substances*, in *Small Angle X-ray Scattering*, O. Glatter and O. Kratky, Editors. 1982, Academic Press: New York. p. 119-166.

28. Glatter, O., *Data Treatment*, in *Small Angle X-ray Scattering*, O. Glatter and O. Kratky, Editors. 1982, Academic Press: New York. p. 119-166.

29. Glatter, O., *Interpretation*, in *Small Angle X-ray Scattering*, O. Glatter and O. Kratky, Editors. 1982, Academic Press: New York. p. 167-196.

30. Oshcherin, B.N., *On surface energies of* $A^{N}B^{8-N}$ *semiconducting compounds.* Physica Status Solidi A, 1976. **34** (2): p. K181-6.

31. Nosker, R.W., Mark, P., and Levine, J.D., *Polar Surfaces of Wurtzite and Zincblende Lattices.* Surface Science, 1970. **19** : p. 291-317.

32. Wang, Y.R. and Duke, C.B., *Cleavage faces of wurtzite CdS and CdSe: surface relaxation and electronic structure.* Physical Review B (Condensed Matter), 1988. **37** (11): p. 6417-24.

33. Campbell, D.D. and Farnsworth, H.E., *Studies of Structure and Oxygen Adsorption of {0001} CdS Surfaces by LEED.* Surface Science, 1968. **10** : p. 197-214.

34. Zangwill, A., *Physics at Surfaces*. 1990, Cambridge, U.K.: Cambridge University

Press.

35. Alivisatos, A.P., Johnsson, K.P., Peng, X.G., Wilson, T.E., Loweth, C.J., Bruchez, M.P., and Schultz, P.G., *Organization Of Nanocrystal Molecules Using DNA.* Nature, 1996. **382** (6592): p. 609-611.

36. Luttinger, J.M., *Quantum Theory of Cyclotron Resonance in Semiconductors: General Theory.* Physical Review, 1956. **102** (4): p. 1030-1041.

37. Luttinger, J.M. and Kohn, W., *Motion of Electrons and holes in Perturbed Periodic Fields.* Physical Review, 1955. **97** (4): p. 869-883.

38. Baldereschi, A. and Lipari, N.O., *Spherical model of shallow acceptor states in semiconductors.* Physical Review B (Solid State), 1973. **8** (6): p. 2697-709.

39. Efros, A.L., *Luminescence polarization of CdSe microcrystals.* Physical Review B (Condensed Matter), 1992. **46** (12): p. 7448-58.

40. von Grünberg, H.H., *Energy levels of CdSe quantum dots: Wurtzite versus zinc-blende structure.* Physical Review B (Condensed Matter), 1997. **55** (4): p. 2293-302.

41. Hill, N.A. and Whaley, K.B., *Two-particle calculation of excitonic effects in semiconductor nanocrystals.* Chemical Physics, 1996. **210** (1-2): p. 117-33.

42. Bawendi, M.G., Carroll, P.J., Wilson, L., and Brus, L.E., *Luminescence properties of CdSe quantum crystallites: resonance between interior and surface localized states.* Journal of Chemical Physics, 1992. **96** (2): p. 946-54.

43. Colvin, V.L., Cunningham, K.L., and Alivisatos, A.P., *Electric field modulation studies of optical absorption in CdSe nanocrystals: dipolar character of the excited state.* Journal of Chemical Physics, 1994. **101** (8): p. 7122-38.

44. Schmidt, M.E., Blanton, S.A., Hines, M.A., and Guyot-Sionnest, P., *Polar CdSe nanocrystals: implications for electronic structure*. Journal of Chemical Physics, 1997. **106** (12): p. 5254-9.

45. Henglein, A., Top. Curr. Chem., 1988. **143** : p. 115.

46. Eychmüller, A., Mews, A., and Weller, H., *A quantum dot quantum well: CdS/HgS/CdS*. Chemical Physics Letters, 1993. **208** (1-2): p. 59-62.

47. Mews, A., Eychmüller, A., Giersig, M., Schooss, D., and Weller, H., *Preparation, Characterization, and Photophysics Of the Quantum Dot Quantum Well System CdS/HgS/CdS*. Journal Of Physical Chemistry, 1994. **98** (3): p. 934-941.

48. Herron, N., Calabrese, J.C., Farneth, W.E., and Wang, Y., *Crystal structure and optical properties of* $Cd_{32}S_{14}(SC_6H_5)_{36}{\bullet}DMF_4$, *a cluster with a 15 angstrom CdS core*. Science, 1993. **259** (5100): p. 1426-8.

49. Dance, I.G., Choy, A., and Scudder, M.L., *Syntheses, Properties, and Molecular and Crystal Structures of* $(Me_4N)_4[E_4M_{10}(SPh)_{16}]$ *(E = S, Se; M = Zn, Cd): Molecular Supertetrahedral Fragments of the Cubic Metal Chalcogenide Lattice*. Journal of the American Chemical Society, 1984. **106** (21): p. 6285-6295.

50. Vossmeyer, T., Reck, G., Katsikas, L., Haupt, E.T.K., Schulz, B., and Weller, H., *A "double-diamond superlattice" built up of* $Cd_{17}S_4(SCH_2CH_2OH)_{26}$ *clusters*. Science, 1995. **267** (5203): p. 1476-9.

51. Wulff, G., *Zur Frage der Geschwindigkeit des Wachsthums und der Auflösung der Krystallflächen*. Zeitschrift für Kristallografie, 1901. **34** : p. 449.

52. Whetten, R.L. and Gelbart, W.M., *Nanocrystal Microemulsions - Surfactant-*

Stabilized Size and Shape. Journal Of Physical Chemistry, 1994 : p. 3544-3549.

53. Ahmadi, T.S., Wang, Z.L., Green, T.C., Henglein, A., and El-Sayed, M.A., *Shape-Controlled Synthesis Of Colloidal Platinum Nanoparticles.* Science, 1996. **272** (5270): p. 1924-1926.

54. Guzelian, A.A., Katari, J.E.B., Kadavanich, A.V., Banin, U., Hamad, K., Juban, E., Alivisatos, A.P., Wolters, R.H., Arnold, C.C., and Heath, J.R., *Synthesis Of Size-Selected, Surface-Passivated InP Nanocrystals.* Journal Of Physical Chemistry, 1996. **100** (17): p. 7212-7219.

55. Guzelian, A.A., Banin, U., Kadavanich, A.V., Peng, X., and Alivisatos, A.P., *Colloidal chemical synthesis and characterization of InAs nanocrystal quantum dots.* Applied Physics Letters, 1996. **69** (10): p. 1432-4.

56. Yeh, C.Y., Lu, Z.W., Froyen, S., and Zunger, A., *Zinc-blend-wurtzite polytypism in semiconductors.* Physical Review B (Condensed Matter), 1992. **46** (16): p. 10086-97.

57. Littau, K.A., Szajowski, P.J., Muller, A.J., Kortan, A.R., and Brus, L.E., *A Luminescent Silicon Nanocrystal Colloid Via a High-Temperature Aerosol Reaction.* Journal Of Physical Chemistry, 1993. **97** (6): p. 1224-1230.

58. Eaglesham, D.J., White, A.E., Feldman, L.C., Moriya, N., and Jacobson, D.C., *Equilibrium shape of Si.* Physical Review Letters, 1993. **70** (11): p. 1643-6.

59. Packard, W.E. and Dow, J.D., *Scanning tunneling microscope of the "16*2" reconstructed Si(110) surface.* Journal of Applied Physics, 1997. **81** (2): p. 994-6.

60. Safta, N., Lacharme, J.P., and Sebenne, C.A. *Clean Si(110): a surface with intrinsic or extrinsic defects?* in *8th International Conference on Solid Surfaces.* 1992. The

Hague, Netherlands.

61. Yamamoto, Y., *Atomic arrangements of 16*2 and (17,15,1) 2*1 structures on a Si(110) surface.* Physical Review B (Condensed Matter), 1994. **50** (12): p. 8534-8.

62. Iijima, S., *Fine particles of silicon. I. Crystal growth of spherical particles of Si.* Japanese Journal of Applied Physics, Part 1 (Regular Papers & Short Notes), 1987. **26** (3): p. 357-64.

63. Hayashi, S., Tanimoto, S., Fujii, M., and Yamamoto, K., *Surface oxide layers of Si and Ge nanocrystals.* Superlattices and Microstructures, 1990. **8** (1): p. 13-18.

64. Okada, R. and Iijima, S., *Oxidation property of silicon small particles.* Applied Physics Letters, 1991. **58** (15): p. 1662-1663.

65. Alford, J.M., Laaksonen, R.T., and Smalley, R.E., *Ammonia chemisorption studies on silicon cluster ions.* Journal of Chemical Physics, 1991. **94** (4): p. 2618-30.

66. Cheshnovsky, O., Yang, S.H., Pettiette, C.L., Craycraft, M.J., Liu, Y., and Smalley, R.E., *Ultraviolet photoelectron spectroscopy of semiconductor clusters: silicon and germanium.* Chemical Physics Letters, 1987. **138** (2-3): p. 119-24.

67. Anderson, L.R., Maruyama, S., and Smalley, R.E., *Ethylene chemisorption on levitated silicon cluster ions: evidence for the importance of annealing.* Chemical Physics Letters, 1991. **176** (3-4): p. 348-54.

68. Jarrold, M.F. and Constant, V.A., *Silicon cluster ions: evidence for a structural transition.* Physical Review Letters, 1991. **67** (21): p. 2994-7.

69. Kaxiras, E. and Jackson, K., *Shape of small silicon clusters.* Physical Review Letters, 1993. **71** (5): p. 721-30.

70. Colvin, V.L., Goldstein, A.N., and Alivisatos, A.P., *Semiconductor nanocrystals covalently bound to metal surfaces with self-assembled monolayers.* Journal of the American Chemical Society, 1992. **114** (13): p. 5221-30.

71. Murray, C.B., Kagan, C.R., and Bawendi, M.G., *Self-organization of CdSe nanocrystallites into three-dimensional quantum dot superlattices.* Science, 1995. **270** (5240): p. 1335-8.

72. Goldstein, A.N., *The Melting Of Silicon Nanocrystals - Submicron Thin-Film Structures Derived From Nanocrystal Precursors.* Applied Physics a-Materials Science & Processing, 1996. **62** (1): p. 33-37.

73. Colvin, V.L., Schlamp, M.C., and Alivisatos, A.P., *Light-Emitting Diodes Made From Cadmium Selenide Nanocrystals and a Semiconducting Polymer.* Nature, 1994. **370** (6488): p. 354-357.

74. Danek, M., Jensen, K.F., Murray, C.B., and Bawendi, M.G., *Synthesis of Luminescent Thin-Film CdSe/ZnSe Quantum Dot Composites Using CdSe Quantum Dots Passivated with an Overlayer of ZnSe.* Chemistry of Materials, 1996. **8** (1): p. 173-180.

75. Hoener, C.F., Allan, K.A., Bard, A.J., Campion, A., Fox, M.A., Mallouk, T.E., Webber, S.E., and White, J.M., *Demonstration Of a Shell Core Structure In Layered CdSe-ZnSe Small Particles By X-Ray Photoelectron and Auger Spectroscopies.* Journal Of Physical Chemistry, 1992. **96** (9): p. 3812-3817.

76. Schooss, D., Mews, A., Eychmüller, A., and Weller, H., *Quantum-dot quantum well CdS/HgS/CdS: theory and experiment.* Physical Review B (Condensed Matter), 1994. **49** (24): p. 17072-8.

77. Mews, A., Kadavanich, A.V., Banin, U., and Alivisatos, A.P., *Structural and spectroscopic investigations of CdS/HgS/CdS quantum-dot quantum wells.* Physical Review B, Rapid Communications, 1996. **53** (20): p. R13242-R13245.

78. Szuszkiewicz, W., Dybko, K., Dynowska, E., Gorecka, J., Witkowska, B., and Hennion, B. *Lattice dynamics of cubic mercury sulphide.* in *25th International School on Physics of Semiconducting Compounds.* 1996. Jaszowiec, Poland.

79. Porowski, S., Jun, J., Krukowski, S., Bockowski, M., Tedenac, J.C., and Record, M.C. *High pressure differential thermal analysis (DTA) and crystal growth of alpha -HgS.* in *Joint International Association for Research and Advancement of High Pressure Science and Technology and American Physical Society Topical Group on Shock Compression of Condensed Matter Conference.* 1993. Colorado Springs, CO, USA.

80. Tedenac, J.C., Record, M.C., Ayral-Marin, R.M., Brun, G., Jun, J., Grzegory, I., Krukowski, S., and Bockowski, M. *Phase transformations and p-T diagram of some HgX compounds (X=S, Se, Te).* in *5th International Conference on High Pressure in Semiconductor Physics.* 1992. Kyoto, Japan.

81. Broser, I., Broser, R., and Rosenzweig, M., in *Numerical Data and Functional Relationships in Science and Technology*, D. Madelung, Editor. Landolt-Börnstein, New Series, Group III. 1982, Springer Verlag: Berlin.

82. Heath, J.R., *The Chemistry Of Size and Order On the Nanometer Scale.* Science, 1995. **270** (5240): p. 1315-1316.

83. Ohara, P.C., Heath, J.R., and Gelbart, W.M., *Self-assembly of submicrometer rings of particles from solutions of nanoparticles.* Angewandte Chemie-International Edition

In English, 1997. **36** (10): p. 1078+.

84. Bowden, N., Terfort, A., Carbeck, J., and Whitesides, G.M., *Self-assembly of mesoscale objects into ordered two-dimensional arrays.* Science, 1997. **276** (5310): p. 233-5.